KINETIC, MORPHOLOGICAL, AND COMPOSITIONAL CHARACTERIZATION OF THE UPTAKE OF AQUEOUS Ba^{2+}, Mn^{2+}, AND Cd^{2+} IONS BY CALCITE AND ARAGONITE OVER A WIDE RANGE OF CONCENTRATION

A Thesis Submitted to
the Graduate School of Engineering and Science of
İzmir Institute of Technology
in Partial Fulfillment of the Requirements for the Degree of

MASTER OF SCIENCE

in Chemistry

by
Özge TUNUSOĞLU

July 2007
İZMİR

We approve the thesis of **Özge TUNUSOĞLU**

Date of Signature

……
Assoc. Prof. Dr. Talal SHAHWAN
Supervisor
Department of Chemistry
İzmir Institute of Technology

16 July 2007

……
Assoc. Prof. Dr. Ahmet E. EROĞLU
Department of Chemistry
İzmir Institute of Technology

16 July 2007

……
Assoc. Prof. Dr. Hürriyet POLAT
Department of Chemistry
İzmir Institute of Technology

16 July 2007

……
Assoc. Prof. Dr. Serdar ÖZÇELİK
Department of Chemistry
İzmir Institute of Technology

16 July 2007

……
Assoc. Prof. Dr. Selahattin YILMAZ
Department of Chemical Engineering
İzmir Institute of Technology

16 July 2007

……
Prof. Dr. Levent ARTOK
Head of Department
İzmir Institute of Technology

……
Prof. Dr. M. Barış ÖZERDEM
Head of the Graduate School

ACKNOWLEDGMENTS

I would like to express my grateful thanks to my supervisor Assoc. Prof. Dr. Talal R. A. SHAHWAN, for his instructive comments, motivations, and valued support throughout my thesis study and patience to my questions.

I would also like to thank Assoc. Prof. Dr. Ahmet E. EROĞLU and Assoc. Prof. Dr. Durmuş ÖZDEMİR for their helps and guidance throughout my study.

Special thanks to group members of Materials Research Center, Evrim YAKUT, Mine BAHÇECİ, Duygu OĞUZ, and Gökhan ERDOĞAN for their helps in XRD and SEM/EDS analysis. Also, I would like to thank to Oya ALTUNGÖZ, Sinan YILMAZ, Aslı ERDEM, Arzu ERDEM, Müşerref YERSEL, and Betül ÖZTÜRK at Department of Chemistry, for their helps in ICP-AES, AAS, and FTIR analysis.

Also, I would like to thank to Demet ERDOĞAN, Çağrı ÜZÜM, and Nazlı EFECAN, for their kindness in laboratory studies.

I am pleased to thank TUBITAK for its financial support for this study (TBAG-2478 (104T089)).

Finally, I would like to express my endless thanks to my family and to Research Assistant Erkin GEZGİN, for their endless support, motivation, and patience.

ABSTRACT

KINETIC, MORPHOLOGICAL, AND COMPOSITIONAL CHARACTERIZATION OF THE UPTAKE OF AQUEOUS Ba^{2+}, Mn^{2+}, AND Cd^{2+} IONS BY CALCITE AND ARAGONITE OVER A WIDE RANGE OF CONCENTRATION

The large availability and widespread distribution of calcium carbonate, $CaCO_3$, in Earth's crust makes it among the most important minerals to investigate in terms of environmentally and geochemically important aqueous-metal partitioning interactions.

In this study, the interactions of Ba^{2+}, Mn^{2+}, and Cd^{2+} with calcite and aragonite were investigated over a wide range of experimental conditions. The experiments were conducted to examine the effects of time, concentration, pH, temperature on the uptake process assess at low concentrations and the composition and morphology of the precipitated carbonates. The kinetic data corresponding to adsorption were adequately described by the pseudo-second order rate equation. At equilibrium, the extent of adsorption on both minerals followed the order $Cd^{2+} > Mn^{2+} > Ba^{2+}$. Precipitation of metal carbonates proceeded at a slower rate and led to large removal of the ions under consideration. The mass fractions of the precipitated metal carbonates were determined using quantitative XRD. For this purpose, empirical equations were developed for binary carbonate mixtures. FTIR was used to follow the possible modifications in vibrational modes of calcite and aragonite, and the newly emerging vibrations of various carbonate phases.

According to SEM results, $BaCO_3$ crystals appeared to be 1-2 micrometers in size with an olivary-like shape and $MnCO_3$ crystals assumed a cubic shape with 200-400 nm size. The particles of precipitated $CdCO_3$ did not demonstrate a well defined shape and its texture appeared to be composed of aggregated sub-micron crystals that form micron sized particles with irregular appearance.

ÖZET

GENİŞ DERİŞİM ARALIĞINDAKİ Ba^{2+}, Mn^{2+} VE Cd^{2+} İYONLARININ KALSİT VE ARAGONİT TARAFINDAN TUTULMALARININ KİNETİK, MORFOLOJİK VE İÇERİK OLARAK BELİRLENMESİ

$CaCO_3$ mineralinin yer kabuğunda büyük miktarlarda bulunması ve çeşitli katyonlara karşı yüksek tutma kapasitesine sahip olması jeokimyasal ve çevresel açılardan özel bir öneme sahiptir.

Bu çalışmada, çevresel etkileri açısından risk taşıyan, periyodik tablodaki çeşitli metal grup/periyotlara mensup Ba^{2+}, Mn^{2+} ve Cd^{2+} iyonlarının kalsit ve aragonit mineralleri ile etkileşimi araştırılmıştır. Yapılan araştırmalar kapsamında, düşük derişimlerdeki tutulmanın belirlenmesinde zaman, derişim etkisi, pH, sıcaklık ve yüksek derişimlerde çökelen karbonatların morfolojik, içerik ve yapısal özellikleri incelenmiştir. Adsorpsiyon aşamasında tutulmanın hızlı olduğu ve ikinci-mertebeden hız denklemine uyduğu görülmüştür. Dengeye ulaşıldığında, hem kalsit hem de aragonitçe tutulan iyon miktarı bakımından sıralamanın $Cd^{2+} > Mn^{2+} > Ba^{2+}$ şeklinde olduğu tespit edilmiştir. Metal karbonatların çökelmesi yavaş hızla ilerlemiş ve söz konusu iyonların büyük oranlarda uzaklaştırılmasına önderlik etmiştir. Kantitatif X-Işınları Kırınımı (XRD) kullanılarak çökelen metal karbonatların kütle fraksiyonları belirlenmiş; bu amaçla, ikili karbonat karışımları için deneysel denklemler geliştirilmiştir. Yapılan Kızıl Ötesi Spektroskopi (FTIR) analizlerine göre, Mn^{2+} ve Cd^{2+} iyonlarının kalsitçe veya aragonitçe adsorpsiyonu sonucunda bu minerallerin titreşim bantlarında çok az değişiklikler olurken, Ba^{2+} adsorpsiyonu çeşitli değişikliklere neden olmaktadır.

Taramalı Elektron Mikroskobu (SEM) sonuçlarına göre, $BaCO_3$ çökeltisinin kristalleri 1-2 mikron boyutunda ve zeytin tanelerine (*olivary-like*) benzemektedir. $MnCO_3$ kristalleri ise küp şeklinde ve bir kaç yüz nanometre boyutunda oluşmuştur. Çöken $CdCO_3$'ın parçaları diğer karbonatlar kadar belirgin bir şekil sergilememekle birlikte, bu parçalar genellikle mikron-altı ve toplu halde bulunan taneciklerden oluşmaktadır.

TABLE OF CONTENTS

LIST OF FIGURES viii
LIST OF TABLES xii

CHAPTER 1. INTRODUCTION 1
1.1. Heavy Metal Pollution 1
1.2. Calcium Carbonate ($CaCO_3$) 3
1.2.1. Calcite 3
1.2.2. Aragonite 4
1.2.3. Vaterite 5
1.3. Uptake Mechanisms of Metals by Carbonates 6
1.3.1. Ion –Exchange Mechanism 6
1.3.2. Surface Complexation 6
1.3.3. Coprecipitation (Solid Solution) 7
1.3.4. Precipitation 9
1.3.5. Solid State Diffusion 10
1.4. Literature Survey 11

CHAPTER 2. SCOPE OF THE STUDY 14
2.1. Aim of This Work 14
2.2. Applied Methods 14
2.2.1. Atomic Absorption Spectrometry (AAS) 14
2.2.2. Inductively Coupled Plasma-Atomic Emission Spectrometry (ICP-AES) 17
2.2.3. X-Ray Diffraction (XRD) 18
2.2.4. Scanning Electron Microscope (SEM) 20
2.2.5. Energy Dispersive X-Ray Spectroscopy (EDS) 21
2.2.6. Fourier Transform Infrared Spectroscopy (FTIR) 22

CHAPTER 3. EXPERIMENTAL 24
3.1. Preparation of Samples 24
3.1.1. Aragonite Synthesis 24
3.2. Determination of Zero Point Charge (ZPC) of Calcite and Aragonite 25
3.3. Particle Size Analysis 25

3.4. BET Analysis 26
3.5. Uptake Experiments 26
3.5.1. Kinetic Experiments 26
3.5.2. Dependence of Metal Uptake on Temperature Change 28
3.5.3. Dependence of Metal Uptake on pH Change 29
3.6. Analysis of Aqueous Solutions 30
3.6.1. AAS 30
3.6.2. ICP-AES 30
3.7. Characterization of the Solid 31
3.7.1. XRD 31
3.7.2. SEM/EDS 31
3.7.3. FTIR 32
3.8. Chemical Speciation Analysis 32

CHAPTER 4. RESULTS AND DISCUSSION 34
4.1. Characterization of Calcite and Aragonite 34
4.2. Kinetic and Equilibrium Description of Metal Adsorption on Calcite and Aragonite 38
4.2.1. Kinetics 38
4.2.2. Percentage Adsorption 42
4.3. Kinetics of Precipitate Formation of Metal Carbonates upon Interaction with Calcite and Aragonite 45
4.3.1. Rate of Precipitate Formation 45
4.3.2. XRD Quantitative Calculations 50
4.3.3. EDS Mapping 57
4.3.4. Effect of pH Change on Precipitate Formation 59
4.3.5. Effect of Temperature Change on Precipitate Formation 61
4.4. The Morphological Aspects and FTIR Spectra of Precipitated Metal Carbonates 62
4.4.1. SEM Images 62
4.4.2. Fourier Transform Infrared (FTIR) 64

CHAPTER 5. CONCLUSION 69
REFERENCES 71

LIST OF FIGURES

Figure **Page**

Figure 1.1. Structure of Calcite……4

Figure 1.2. Structure of Aragonite……5

Figure 2.1. Instrumentation of AAS……16

Figure 2.2. Instrumentation of ICP-AES……....17

Figure 2.3. Instrumentation of XRD……19

Figure 2.4. Illustration of Bragg's Law……...19

Figure 2.5. Instrumentation of SEM……21

Figure 2.6. Instrumentation of FTIR …….....22

Figure 3.1. Chemical speciation curves of (a) Ba^{2+}, (b) Mn^{2+}, and (c) Cd^{2+} at initial concentration of 1000 mg/L in aqueous solution. Ionic Strength (I): 0.001 and Temperature (T): 25^{o}C……..33

Figure 4.1. XRD diagrams of (a) calcite and (b) aragonite used in this work……..34

Figure 4.2. Characteristic SEM images of (a) calcite and (b) aragonite…… …….35

Figure 4.3. EDS spectra of (a) calcite and (b) aragonite……35

Figure 4.4. Particle size distribution (for particles less than 38 μm) for: (a) calcite and (b) aragonite……..…36

Figure 4.5. Variation of zeta potential with respect to pH for (a) calcite and (b) aragonite……...37

Figure 4.6. The variation of uptake of the ions (a) Ba^{2+}, (b) Mn^{2+}, and (c) Cd^{2+} by calcite mineral with respect to mixing time……39

Figure 4.7. The variation of uptake of the ions (a) Ba^{2+}, (b) Mn^{2+}, and (c) Cd^{2+} by aragonite mineral with respect to mixing time…… ……40

Figure 4.8. The linear fits obtained by use of second order rate equation: (a) adsorption of the ions on calcite, (b) adsorption of the ions on aragonite……41

Figure 4.9. The change in *104* XRD signal of $BaCO_3$ (witherite) precipitate formed by the interaction of Ba^{2+} ions with calcite; (a) 1000 mg/L Ba^{2+}, (b) 5000 mg/L Ba^{2+}, (c) 10000 mg/L Ba^{2+}……..……..46

Figure 4.10. The change in *104* XRD signal of $BaCO_3$ (witherite) precipitate formed by the interaction of Ba^{2+} ions with aragonite; (a) 1000 mg/L

Ba^{2+}, (b) 5000 mg/L Ba^{2+}, (c) 10000 mg/L Ba^{2+} ……..……46
Figure 4.11. The change in *104* XRD signal of $MnCO_3$ (rhodochrosite) precipitate formed by the interaction of Mn^{2+} ions with calcite; (a) 1000 mg/L, Mn^{2+} (b) 5000 mg/L Mn^{2+}, (c) 10000 mg/L Mn^{2+} ……..…….47
Figure 4.12. The change in *104* XRD signal of $MnCO_3$ (rhodochrosite) precipitate formed by the interaction of Mn^{2+} ions with aragonite; (a) 1000 mg/L Mn^{2+}, (b) 5000 mg/L Mn^{2+}, (c) 10000 mg/L Mn^{2+} ……....47
Figure 4.13. The change in *104* XRD signal of $CdCO_3$ (otavite) precipitate formed by the interaction of Cd^{2+} ions with calcite; (a) 1000 mg/L Cd^{2+}, (b) 5000 mg/L Cd^{2+}, (c) 10000 mg/L Cd^{2+} …….……...48
Figure 4.14. The change in *104* XRD signal of $CdCO_3$ (otavite) precipitate formed by the interaction of Cd^{2+} ions with aragonite; (a) 1000 mg/L Cd^{2+}, (b) 5000 mg/L Cd^{2+}, (c) 10000 mg/L Cd^{2+} ……. ……..48
Figure 4.15. Variation of the mass fractions of $MeCO_3$ in their mixtures with calcite as a function of the intensity ratio of the $MeCO_3$/calcite; $MeCO_3$= (a) $BaCO_3$, (b) $MnCO_3$, (c) $CdCO_3$……...….51
Figure 4.16. Variation of the mass fractions of $MeCO_3$ in their mixtures with aragonite as a function of the intensity ratio of the $MeCO_3$/aragonite; $MeCO_3$= (a) $BaCO_3$, (b) $MnCO_3$, (c) $CdCO_3$…….52
Figure 4.17. The change of mass fractions of precipitated $BaCO_3$ as a function of time and initial concentration; (a) on calcite surface, (b) on aragonite surface…….54
Figure 4.18. The change of mass fractions of precipitated $MnCO_3$ as a function of time and initial concentration; (a) on calcite surface, (b) on aragonite surface…….55
Figure 4.19. The change of mass fractions of precipitated $CdCO_3$ as a function of time and initial concentration; (a) on calcite surface, (b) on aragonite surface…….56
Figure 4.20. X-ray maps showing the distributions of (a) Ca on $BaCO_3$-calcite surface, (b) Ba on $BaCO_3$-calcite surface, (c) Ca on $BaCO_3$-aragonite surface, (d) Ba on $BaCO_3$-aragonite surface……58
Figure 4.21. X-ray maps showing the distributions of (a) Ca on $MnCO_3$-calcite surface, (b) Mn on $MnCO_3$-calcite surface, (c) Ca on $MnCO_3$-aragonite surface, (d) Mn on $MnCO_3$-aragonite surface……58

Figure 4.22. X-ray maps showing the distributions of (a) Ca on $CdCO_3$-calcite surface, (b) Cd on $CdCO_3$-calcite surface, (c) Ca on $CdCO_3$-aragonite surface, (d) Cd on $CdCO_3$-aragonite surface……...59
Figure 4.23. XRD diagrams of the precipitates formed on calcite surface after the pH of medium was adjusted to 10.0 (a) $BaCO_3$, (b) $MnCO_3$, and (c) $CdCO_3$. The initial ion concentrations are (i) 1000 mg/L, (ii) 5000 mg/L, and (iii) 10000 mg/L……60
Figure 4.24. XRD diagrams of the precipitates formed on aragonite surface after the pH of medium was adjusted to 10.0 (a) $BaCO_3$, (b) $MnCO_3$, and (c) $CdCO_3$. The initial ion concentrations are (i) 1000 mg/L, (ii) 5000 mg/L, and (iii) 10000 mg/L. ……..……..60
Figure 4.25. XRD diagrams of the precipitates formed on calcite surface after the temperature of medium was adjusted to 50^oC (a) $BaCO_3$, (b) $MnCO_3$, and (c) $CdCO_3$. The initial ion concentrations are (i) 1000 mg/L, (ii) 5000 mg/L, and (iii) 10000 mg/L……61
Figure 4.26. XRD diagrams of the precipitates formed on aragonite surface after the temperature of medium was adjusted to 50^oC (a) $BaCO_3$, (b) $MnCO_3$, and (c) $CdCO_3$. The initial ion concentrations are (i) 1000 mg/L, (ii) 5000 mg/L, and (iii) 10000 mg/L……62
Figure 4.27. SEM images of $BaCO_3$ precipitated on (a, b) calcite surface, (c, d) aragonite surface……....63
Figure 4.28. SEM images of $MnCO_3$ precipitated on (a, b) calcite surface, (c, d) aragonite surface……63
Figure 4.29. SEM images of $CdCO_3$ precipitated on (a, b) calcite surface, (c, d) aragonite surface……64
Figure 4.30. FTIR spectra of (a): (i) calcite, (ii) Ba^{2+}-calcite (500 mg/L Ba^{2+}), (iii) $BaCO_3$-calcite (10000 mg/L Ba^{2+}), (b): (i) aragonite, (ii) Ba^{2+}-aragonite (500 mg/L Ba^{2+}), (iii) $BaCO_3$-aragonite (10000 mg/L Ba^{2+})……...66
Figure 4.31. FTIR spectra of (a): (i) calcite, (ii) Mn^{2+}-calcite (500 mg/L Mn^{2+}), (iii) $MnCO_3$-calcite (10000 mg/L Mn^{2+}), (b): (i) aragonite, (ii) Mn^{2+}-aragonite (500 mg/L Mn^{2+}), (iii) $MnCO_3$-aragonite (10000 mg/L Mn^{2+})……..67

Figure 4.32. FTIR spectra of (a): (i) calcite, (ii) Cd^{2+}-calcite (500 mg/L Cd^{2+}), (iii) $CdCO_3$-calcite (10000 mg/L Cd^{2+}), (b): (i) aragonite, (ii) Cd^{2+}-aragonite (500 mg/L Cd^{2+}), (iii) $CdCO_3$-aragonite (10000 mg/L Cd^{2+})……...68

LIST OF TABLES

Table **Page**

Table 1.1. Ionic Radius and Hydration Energy Values of Cations.…….....3

Table 3.1. Initial and final pH values of solutions of Ba^{2+} in contact with calcite or aragonite at different initial concentrations and contact times. The temperature of the medium was 25°C.……...27

Table 3.2. Initial and final pH values of solutions of Mn^{2+} in contact with calcite or aragonite at different initial concentrations and contact times. The temperature of the medium was 25°C……....27

Table 3.3. Initial and final pH values of solutions of Cd^{2+} in contact with calcite or aragonite at different initial concentrations and contact times. The temperature of the medium was 25°C……28

Table 3.4. The pH change of Ba^{2+}, Mn^{2+}, and Cd^{2+} cations during interactions with calcite at different initial cation concentrations and 50°C…….....29

Table 3.5. The pH change of Ba^{2+}, Mn^{2+}, and Cd^{2+} cations during interactions with aragonite at different initial cation concentrations and 50°C……..29

Table 3.6. The pH values of the samples before filtration in the experiments carried out at pH of 10.0 at various initial concentrations……..30

Table 4.1. Elemental content of calcite and aragonite obtained by EDS analysis……...36

Table 4.2. Mean, median, mode, and standard deviation for particle size analysis of calcite and aragonite minerals.…….…..…36

Table 4.3. Results of surface area and pore size values of calcite and aragonite ...……37

Table 4.4. k_2 and q_e values obtained by use of second order rate equation....…….41

Table 4.5. The equilibrium results corresponding to the uptake of Ba^{2+} ions by calcite and aragonite at various initial concentrations …….....42

Table 4.6. The equilibrium results corresponding to the uptake of Mn^{2+} ions by calcite and aragonite at various initial concentrations …….…..…43

Table 4.7. The equilibrium results corresponding to the uptake of Cd^{2+} ions by calcite and aragonite at various initial concentrations…….……...43

Table 4.8. The partition coefficients calculated by the thermodynamic model of Wang's and Xu's (2001)……45

Table 4.9. ICDD card numbers of mineral carbonates relative to their crystal

structure.....45
Table 4.10. The equations of binary metal carbonates developed for quantitative XRD analysis.....53

CHAPTER 1

INTRODUCTION

1.1. Heavy Metal Pollution

Any metallic chemical that has a relatively high density and is generally toxic or poisonous at low concentrations is named as a heavy metal. These metals are inherent components of Earth's crust and they cannot be demoted or annihilated. Heavy metals enter to human bodies via food, drinking water, and air in a small extent. Although being poisonous at higher concentrations, some heavy metals are essential to maintain the metabolism of the human body. Drinking-water contamination (e.g. lead pipes), high ambient air concentrations near emission sources, or intake via the food chain could be the reason of heavy metal poisoning.

Heavy metals are dangerous as they incline bioaccumulation which means an increase in the concentration of a chemical in a biological organism over time, compared to its value in the environment. Heavy metals can come into the water reservoir by industrial and consumer waste or from acidic rain that causes breaking of soils and releasing them into lakes, rivers, streams, and groundwater. The cations Ba^{2+}, Mn^{2+}, and Cd^{2+} applied in this study are known to be among the cations that possess various risks from the environmental perspective.

Barium whose chemistry is analogous to that of the other alkaline earth metals is detected in most surface waters with a median concentration of 43µg/L. Its concentration range in surface waters varies between 2 and 340µg/L; hence, elevated concentrations point out the presence of industrial pollution (Pagenkopf 1978). Barium has a variety of radioactive isotopes. One of these, ^{140}Ba ($t_{1/2}$=12.8 d) is formed in a great yield (6.21%) as a result of fission reactions (Lieser 1995), and as a result this isotope is important in radioactive waste management. Two forms of barium, barium sulfate ($BaSO_4$) and barium carbonate ($BaCO_3$) are naturally found in underground ores. Barium compounds are used in paint, brick, tile, glass, eraser, insect and rat poisons, oil industries, and as an additive in fuels. This element is taken into human body via drinking waters contaminated with barium, eating waste entangled plants, or breathing

dust particles entangled with barium. If taken in high concentrations, barium compounds may cause paralysis and death. When barium is taken in low amounts, it leads to shortness of breath, increase in blood pressure, change in heart rhythm and nerve reflexes, irritation of stomach, minor changes in blood, weakening of muscles, suffering of kidney, heart, and spleen (WEB_1 2007).

Manganese is a common mineral having four positive oxidation states, +2, +3, +4, and +7 and its most momentous compound is pyrolusite (MnO_2). Divalent state of manganese is stable in acid or nonoxygenated media, and trivalent state should be stabilized by complexation. In addition, insoluble oxide is formed in natural waters by tetravalent state and this oxide is colloidally dispersed or precipitates (Pagenkopf 1978). Manganese is found in nature at elevated amounts. Low amount of this element is necessary for regular physiological functions of human beings and animals. In addition to being one of the natural constituents of some rocks and stones, manganese exists in air, water, soil, and foods at low amounts. On the other hand, manganese is released into air from coke furnaces and powerplants. People working on metallic manganese production are exposed to this element via breathing and it is concluded by health problems. Continuous exposures may cause permanent brain damages. While anorexia, weakness, and dormancy are determined in earlier symptoms, it can be possible to come across with speech and character defects, and also balance problems. Manganese may cause Parkinson's disease, allergy in lungs, damages in kidney and liver at very high doses and long-term exposures.

Cadmium is one of the toxic metals with an oxidation state of +2. It can enter waterways via native leaching of zinc blende, industrial releases, inappropriate mining operations, or deterioration of galvanized pipe (Pagenkopf 1978). Cadmium is used in electronic products, batteries, pigments, plastic stabilizers, metal sheets, and industrial materials involving alloys. Extreme exposures of cadmium cause lungs to blister; however, long-term low level effects evoke chronic kidney and lung diseases. In addition to these effects, it can cause hypertension, other heart diseases and affects the skeleton system. It is known that, cadmium may show carcinogenic effect on human beings. Birds and mammals are relatively resistant to excessive influences of cadmium; nevertheless, it is possible that chronic exposures to cadmium cause histologic changes in kidney, liver, heart tissue, blood vessels, and bone marrows. Moreover, chronic exposures lead to increase in death ratios, decrease in growing, and inhibition of reproduction.

The ionic radius and hydration energy values of the studied metal ions in addition to that of Ca^{2+} cations are given in Table 1.1.

Table 1.1. Ionic Radius and Hydration Energy Values of Cations
(Source: Langmuir 1997)

CATION	IONIC RADIUS (Å)	HYDRATION ENERGY (J/mol)
Ca^{2+}	1.00	-1577
Ba^{2+}	1.35	-1305
Mn^{2+}	0.83	-1841
Cd^{2+}	0.95	-1807

1.2. Calcium Carbonate ($CaCO_3$)

Carbonates are very common minerals which form about 4% by weight of Earth's crust, and thus are among the most important minerals that play a central role in the regulation of biogeochemical cycles of heavy metals in the environment. In addition to this, carbonates control the aquatic environments through sorption, dissolution, and precipitation reactions which occur between mineral lattice and bulk solution interface (Shahwan et al. 2002). In addition to being found in structures of rocks, calcium carbonate is a fundamental component of seashells and the shells of snails. Calcium carbonate can be naturally found in three polymorphs; calcite, aragonite, and vaterite.

Calcium carbonate is also used in medicine as a calcium supplement or as antacid. Furthermore, $CaCO_3$ has applications in rubber, paint, paper industries and cosmetics.

1.2.1. Calcite

Calcite, which obtained its name from the word "chalix" meaning lime in Greek, is thermodynamically the most stable polymorph of calcium carbonate at room temperature and atmospheric pressure (WEB_2 2007, Langmuir 1997). This polymorph is the most important constituent of the carbonate rocks and forms 99% of these kinds of rocks. Also, calcite can be found as limestone and marble. Under influences of high

heat and pressure of metamorphic circumstances limestone is converted into marble. The best property of calcite is its use in the acid taste since calcite always bubbles when weak acids lay on specimens. The reason of this bubbling is the carbon dioxide gas formation as in Equation 1.1.

$$CaCO_3(s) + 2\ H^+ \longrightarrow\ Ca^{2+} + H_2O + CO_2(g) \qquad (1.1)$$

Due to this test, the geologists can understand if the sandstone sample contains any cementing mineral since cement in sandstones effervesces. Calcite is generally white or colorless and possesses a rhombohedral crystal structure with the trigonal carbonate ions being coplanar as seen in Figure 1.1. The planes including carbonate ions are perpendicular to the c-axis and they are rotated by 60^o from one carbonate layer to the other carbonate layer.

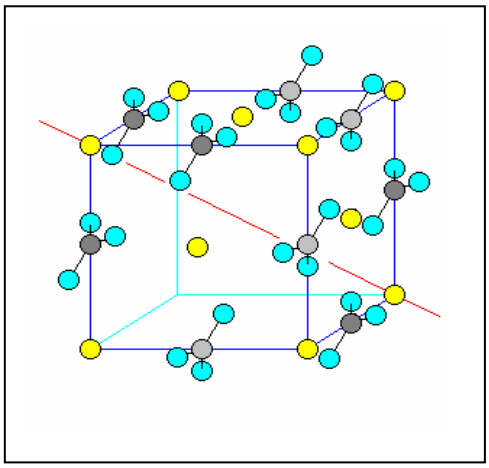

Figure 1.1. Structure of Calcite
(Source: WEB_3 2005)

1.2.2. Aragonite

Aragonite is a universal carbonate mineral and thermodynamically unstable polymorph of calcium carbonate at normal surface temperatures and pressures. It can be stable at higher pressures, but not at higher temperatures since the dry mineral possess a tendency to convert to calcite spontaneously at higher temperatures. Aragonite is

generally white or colorless and possesses orthorhombic crystal structure as seen in Figure 1.2.

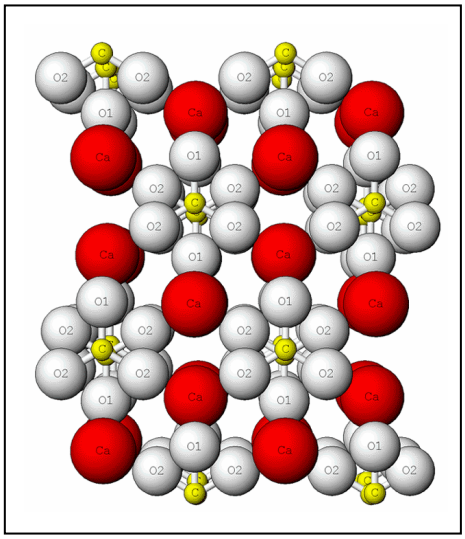

Figure 1.2. Structure of Aragonite
(Source: WEB_4 2006)

The structure of aragonite is composed of triangular carbonate ion groups, (CO_3^{2-}), where carbon is at the center of the triangle and the three oxygens are at each corner. As it is known, the carbonate ions are situated in a single plane and each ion points to the same direction. However, in aragonite, the carbonate ions are not situated in a single plane and they do not point the same direction. By destroying the characteristic trigonal symmetry of calcite structure, they lie in two planes pointing to opposite directions (WEB_5 2007).

1.2.3. Vaterite

Vaterite is a rare mineral that only appears in highly supersaturated solutions with respect to aragonite and calcite (Langmuir 1997). It takes its name from the German mineralogist Heinrich Vater. Contrary to other calcium carbonate polymorphs, vaterite is considered to be a metastable phase and possesses higher solubility than other polymorphs. Consequently, when vaterite is subjected to water, it converts to calcite at

low temperatures or aragonite at high temperatures (about 60^{o}C). It inherently exists in mineral springs, organic tissues, gallstones, and urinary calculi.

1.3. Uptake Mechanisms of Metals by Carbonates

1.3.1. Ion –Exchange Mechanism

Any replacement of an ion in a solid phase in contact with a solution by another ion is called as "ion-exchange" despite the fact that it possesses different meanings as a word. In a more restrictive sense, the term is utilized for the characterization of replacement of one adsorbed, easily changeable ion by another. This wariness, utilized in soil science, indicates a surface occurrence including charged species in outer-sphere complexes. Operationally, the amount of moles of adsorbed ion charge that can be desorbed from unit mass of soil, under specified conditions of temperature, pressure, soil solution composition, and soil-solution mass ratio is named as the ion exchange capacity of a soil (or of soil-minerals in waters or sediments). Thus, the replacement of (natural) effortlessly exchangeable ions by a standard cation or anion is usually included in the measurement of an ion exchange capacity. For cations in contact with carbonate minerals, ion-exchange is perceived as one of the possible uptake mechanisms at low cation concentrations. The reaction between $CaCO_3$ and Sr^{2+} is given as an example of ion-exchange mechanism, as in Equation 1.2 (Stumm and Morgan 1996). Experimental evidence based on structural techniques showed that at low concentrations Sr^{2+} ions were six-fold coordinated implying no change in the structural environment of calcite. This can take place only if a simple exchange of Ca^{2+} for Sr^{2+} occurs (Stumm and Morgan 1996). In addition to cation concentration, the size of the particular cation is also expected to affect the extent of ion exchange in carbonate mineral.

$$CaCO_3(s) + Sr^{2+} \Longleftrightarrow SrCO_3(s) + Ca^{2+} \qquad (1.2)$$

1.3.2. Surface Complexation

At the interface, atoms, molecules, and ions exert forces on each other. Adsorption, the accumulation of matter at the solid-water interface, is the essence of

most surface-chemical processes. It also involves surface complexation reactions in which coordinative bonds are formed between metals and ligands at the surface (Stumm and Morgan 1996).

In the $MeCO_3(s)$-H_2O-CO_2 system the following reactions illustrate the surface speciation. The values of logarithms of equilibrium constants are given in Equation 1.3-1.8 where the metal ion is calcium (Capellen et al. 1993).

$$>CO_3H^0 \Longleftrightarrow >CO_3^- + H^+ \qquad \log K = -4.9 \qquad (1.3)$$

$$>CO_3H^0 + Me^{2+} \Longleftrightarrow >CO_3Me^+ + H^+ \qquad \log K = -2.8 \qquad (1.4)$$

$$>MeOH_2^+ \Longleftrightarrow >MeOH^0 + H^+ \qquad \log K = -12.2 \qquad (1.5)$$

$$>MeOH^0 \Longleftrightarrow >MeO^- + H^+ \qquad \log K = -17.0 \qquad (1.6)$$

$$>MeOH^0 + CO_2 \Longleftrightarrow >MeHCO_3^0 \qquad \log K = 6.0 \qquad (1.7)$$

$$>MeOH^0 + CO_2 \Longleftrightarrow >MeCO_3^- + H^+ \qquad \log K = -2.6 \qquad (1.8)$$

In surface complexation model, the basic idea is the formation of chemical bonds between water molecules and dissolved species at mineral surfaces. The initial hydration surface sites for (hydr)oxide minerals are hydroxylated surface cation centers: $>MeOH^0$ which can either deprotonate (MeO^-) or protonate ($>MeOH_2^+$). In the carbonate-aqueous systems, the following two types of surface sites are produced with hydration of a metal carbonate mineral surface: $>MeOH^0$ and $>CO_3H^0$. Thus, by the hydration of calcite surface $>CaOH^0$ and $>CO_3H^0$ are formed, the existence of which was proven spectroscopically (Capellen et al. 1993). Surface complexes are suggested to be formed by the dissolved hydroxo metal complex $Me(OH)^+$, at high pH values in addition to Me^{2+}, normally found at lower pH values. At carbonate surface metal centers, such a complexation occurs via oxygen bridging (Capellen et al. 1993).

$$>MeOH^0 + Me^{2+} \Longleftrightarrow MeOMe^+ + H^+ \qquad (1.9)$$

1.3.3. Coprecipitation (Solid Solution)

In natural systems, carbonate minerals precipitate in the presence of different solutes. Even though trace amounts of components exist in the solution, these components may get incorporated into the solid carbonate minerals (Stumm 1992).

Coprecipitation provides a thermodynamics construct between surface complexation and bulk solid precipitation. It is predicted that, surface complexation predominates at low sorbate/sorbent ratios. As the surface is loaded with sorbed ion, a solid solution is formed as a precipitate until the surface sites become saturated (Zhu 2002, Stumm 1992).

Solid solution formation can be seen in the sorption of Cd^{2+} ion on $CaCO_3$. In an initial first step, Cd^{2+} (0.95 Å) ions are adsorbed by hydrated layer of the calcite surface (ionic size of Ca^{2+} is 1.00 Å). Then, surface precipitation occurs in a slow step. After a slow long term recrystallization, it is determined that a new crystalline material in the presence of Cd^{2+} grow as a solid solution rather than as pure calcite. The reaction between calcium carbonate and Cd^{2+} ion is given as below where some of $CdCO_3(s)$ dissolves in $CaCO_3(s)$ (Stumm 1992, Stumm and Morgan 1996).

$$CaCO_3(s) + Cd^{2+} \Longleftrightarrow CdCO_3(s) + Ca^{2+} \qquad (1.10)$$

A well known natural example of solid solution is magnesian calcite. It is a predominant carbonate phase in seawater and in the analyses it is seen that, 30% mol of natural calcites formed at low temperatures contain $MgCO_3$. The reaction between magnesium and calcium carbonate (either calcite or aragonite) proceeds as below;

$$Ca_{(1-x)}Mg_xCO_3(s) \Longleftrightarrow (1-x)Ca^{2+} + xMg^{2+} + CO_3^{2-} \quad ; K_{eq(x)} \qquad (1.11)$$

$$Ca^{2+} + CO_3^{2-} \Longleftrightarrow CaCO_3(s) \quad ; 1/K_{sp(CaCO3)} \qquad (1.12)$$

$$Ca_{(1-x)}Mg_xCO_3(s) + xCa^{2+} \Longleftrightarrow CaCO_3(s) + xMg^{2+} \quad ; K_{eq(x)}\ 1/K_{sp(CaCO3)} \qquad (1.13)$$

$$([Mg^{2+}] / [Ca^{2+}])^x = K_{eq(x)}\ 1/K_{sp(CaCO3)} \qquad (1.14)$$

The Mg-calcite is less stable than $CaCO_3(s)$ if a Mg-calcite is in contact with a solution whose $([Mg^{2+}] / [Ca^{2+}])^x$ ratio is not greater than $K_{eq(x)}\ 1/K_{sp(CaCO3)}$. Hence, in marine sediments high Mg-calcite should be transformed into calcite or aragonite. As the Mg-calcite is dissolved, Mg^{2+} proportion becomes richer in the solution and pure $CaCO_3(s)$ is precipitated. Beside calcite, low Mg-calcites (x=3-4 mol %) are plausibly stable; however, higher Mg-calcites might carry on for substantial time periods in spite of being thermodynamically unstable. As a consequence, surface processes fulfill a degree of metastability rapidly whereas phase equilibrium is not accomplished in spite of long time periods (Stumm 1992)

1.3.4. Precipitation

A precipitate is a very fine crystalline which is usually formed from vigorously oversaturated solutions. In order to understand if a solution or natural water is over- or undersaturated, the free energy of dissolution of the solid phase is examined if their values are positive, negative, or zero.

$$CaCO_3(s) \Longleftrightarrow Ca^{2+} + CO_3^{2-} \qquad K_{sp} = 4.5 \times 10^{-9} \text{ (for calcite)}$$
$$K_{sp} = 6.0 \times 10^{-9} \text{ (for aragonite)}$$

The free energy of dissolution is given in Equation 1.15.

$$\Delta G = RT \ln Q/K_{sp} \qquad (1.15)$$

$$= RT \ln \left\{ \frac{[Ca^{2+}]_{act} [CO_3^{2-}]_{act}}{[Ca^{2+}]_{eq} [CO_3^{2-}]_{eq}} \right\} = RT \ln (IAP)/K_{sp}$$

The condition of saturation of solution with respect to a solid depends on the comparison between ion activity product, IAP, and solubility product, K_{sp}. For a system, the terms oversaturation, saturation, and undersaturation could be defined as;

$IAP > K_{sp}$ (oversaturated)
$IAP = K_{sp}$ (equilibrium, saturated)
$IAP < K_{sp}$ (undersaturated)

In terms of concentration, the saturation conditions for all reactions including a solid phase are determined by the comparison of quotient, Q, and K_{sp} values. A solid phase dissolves when Q/K_{sp} is less than 1; in contrast, it precipitates when Q/K_{sp} is greater than 1 (Stumm and Morgan 1996). In carbonate systems, the cation adsorbs to bulk CO_3^{2-} ion in order to achieve precipitation on surface.

For the cations studied in this work, the equations of bulk precipitations leading to the formation of $BaCO_3$, $MnCO_3$, and $CdCO_3$ together with the corresponding K_{sp} values are given as Equation 1.16, 1.17, and 1.18, respectively.

$$Ba^{2+} + CO_3^{2-} \Leftrightarrow BaCO_3(s) \qquad K_{sp} = 5.0 \times 10^{-9} \qquad (1.16)$$

$$Mn^{2+} + CO_3^{2-} \Leftrightarrow MnCO_3(s) \qquad K_{sp} = 5.0 \times 10^{-10} \qquad (1.17)$$

$$Cd^{2+} + CO_3^{2-} \Leftrightarrow CdCO_3(s) \qquad K_{sp} = 1.8 \times 10^{-14} \qquad (1.18)$$

These reactions correspond to systems containing dissolved carbonate ions together with the given cation in solution. In the presence of a carbonate solid in the solution, precipitation can take place at the solid surface even at metal concentration below the values corresponding to supersaturation. This is caused by the higher metal concentration in the vicinity of the carbonate particle due to the counter charge attractions. According to the surface precipitation model (Zhu 2002), precipitation at the surface is thought of as a pre-step to bulk precipitation, as the thing given by the Equation 1.19 and 1.20, respectively.

$$= CaCO_3^{o} + M^{2+} + HCO_3^{-} \Longleftrightarrow CaCO_3(s) + = MCO_3^{o} + H^{+}$$

(surface precipitation of the metal, M^{2+}) (1.19)

$$= MCO_3^{o} + M^{2+} + HCO_3^{-} \Longleftrightarrow MCO_3(s) + = MCO_3^{o} + H^{+}$$

(bulk precipitation) (1.20)

These equations illustrates also the presumed effect of bicarbonate ions which are extensively present in carbonate system at pH values close of natural levels.

1.3.5. Solid State Diffusion

Countless chemical reactions and micro-structural modifications occur in solids through solid state diffusion, i.e. migration and transfer of atoms in solid phases. The diffusions occur due to the defects in solids such as, cavities and interstitial ions, grain boundaries, dislocations, inner and outer surfaces. Various types of diffusion in oxide and other inorganic compounds are caused by temperature, partial pressures of the constituents of compounds, microstructure, and grain size (WEB_6 2007). In soil, since lots of free ions exist, they can change from one state to another by the effect of temperature and pressure when they are in solid form (MCa_yCO_3). However, it requires

long time periods to occur and is thus not expected to contribute to metal uptake by the carbonate minerals in the course of short adsorption processes.

1.4. Literature Survey

The sorption behaviors of various heavy metals and radioactive isotopes by calcium carbonate were subject to plenty of researches. Natural $CaCO_3$ samples generally forming from calcite and to a lesser extent calcite-aragonite mixtures were used in these studies; nevertheless, the number of studies in which pure aragonite was used, is very limited. In addition to our knowledge, there is no data available on the precipitate overgrowth kinetics of the studied metal carbonates.

In previous studies, it is reported that $CaCO_3$ is especially important for industrial and municipal waste control involving heavy metals (Sanchez and Ayuso 2002, Speck et al. 1998, Bilinski et al. 1991, Zachara and Cowan 1991, Johnson and Furrer 2002, Kirby and Rimstidt 1994). In other studies, the sorption characteristics of $CaCO_3$ were evaluated for elements that are important in radioactive waste control (Curti 1999, Piriou et al. 1997, Torstenfelt and Pankow 1982, Meece and Benninger 1993, Robbins et al. 1992, Magaritzl et al. 1990, Bancroft et al. 1977). In addition, a large number of studies exist in literature pointing out the importance of precipitation formation or co-precipitation phenomenon in the uptake of metals by calcite (Martin-Garin et al. 2002, Stipps 1999, Ning et al. 1996, Weijden et al. 1994, Zachara et al. 1988, Fuller and Davis 1987, Davis et al. 1987, Zachara et al. 1989, Pingitore et al. 1988, Terekado and Masuda 1988, Kitano 1986, Lorens 1981).

Mechanistically, there are three major uptake processes of cations by carbonate minerals; adsorption, co-precipitation (or solid solution formation), and precipitation (appearance of cation carbonate as a separate phase). According to literature sources, the plausibility of precipitation or solid solution formation is dependent on the size and the charge of cation (Curti 1999). As the size and charge of retained ion approaches that of Ca^{2+}, the possibility of co-precipitation increases. It is reported that co-precipitation is also dependent on the solubility products of retained cation-carbonate ions and this phenomenon is based on Fajan's "precipitation law". According to this law, it is expected that as the solubility of the substance formed by retained cation and anion

found in precipitate decreases, the amount of this cation increases in the substance (Curti 1999).

The retention of alkali metal cations by calcite is reported to occur in the cavities (interstitial positions) of mineral structure rather than co-precipitation. However, the data obtained for uptake of these cations show that this mineral does not behave entirely as calcite and that alkali metal ions are retained in vacant places which are formed after leaving of Ca^{2+} ion (Kitano 1986).

In the studies with earth alkaline ions such as Sr^{2+} and Ba^{2+}, the existence of co-precipitation is detected at specific conditions. Nonetheless, it is seen that partition coefficients of these kinds of cations are lower than that of transition elements (Curti 1999, Tesoriero and Pankow 1996, Gutjahr et al. 1996, Miyake et al. 1988). Several studies on calcite and aragonite show that the partition coefficients of Sr^{2+}, Ba^{2+} and Ra^{2+} ions are very close to each other (Curti 1999, Pingitore and Eastman 1984) and it is proposed that the similarities of behaviors between Ba^{2+} and Ra^{2+} ions are sourced by adjacent size (1.35 and 1.48 Å) and electronegativities (0.9 for both ions) of these ions. Comperatively, it is observed that other divalent cations such as Zn^{2+}, Cd^{2+}, Mn^{2+} and Co^{2+} construct more stable precipitates with carbonate ions and that they have high partition coefficient values (Curti 1999).

From a different perspective, it is reported that the presence of $CaCO_3$ in soil minerals enhances the uptake capacities of these minerals. The studies performed previously on the sorption behavior of Ba^{2+} ion on $CaCO_3$-montmorilonite mixture support this approach (Shahwan et al. 2002). In other studies carried out to study the sorption behavior of Zn^{2+} and Pb^{2+} ions on calcite-kaolinite and calcite-clinoptilolite mixtures, the sorption efficiency of calcite in these mixture was documented (Shahwan et al. 2005a, Shahwan et al. 2005b).

Various approaches are followed to examine the distribution of metal ions in natural environments. While some of these approaches are dependent on thermodynamic equilibrium basis, the others are kinetically-based (Martin-Garin et al. 2002). Especially, when precipitation mechanism is under consideration, understanding the kinetic processes is essential for modelling of distribution of metal ions in nature. Some metal ions (e.g. Mn^{2+}, Fe^{2+}) exceed the solubility levels of their concentration values in water. This phenomenon is referred to the slow crystal growth kinetics of metal carbonates (Jensen et al. 2002). The limited amount of kinetic data in literature provides an important motivation to these kinds of studies (Martin-Garin et al. 2002).

It is known that, crystal growth kinetics are dependent on supersaturated conditions, pH, and temperature during precipitation (either as pure compound or solid solution formation) (Sternbeck 1997). It is proposed that, precipitation reactions pass through an intermediate adsorption stage (Curti 1999, Stipps 1999, Kinsman and Holland 1969, Chiarello et al. 1997, Shahwan et al. 2005a). In this intermediate stage, an ion bound to solid surface generally forms an outer-sphere complex, a process which is rapid but involve weak interactions. At last stage, this ion diffuses into the solid in order to form a stable inner-sphere complex by a slower mechanism. Previous studies on Mn^{2+} and Cd^{2+} indicated slow formation of $MnCO_3$ and $CdCO_3$ which can continue up to several days (Fuller and Davis 1987, Wersin et al. 1989).

As it is understood from literature searches, studies investigating the formation kinetics and morphologic properties of metal carbonates are very limited. Most of these studies are related to calcite mineral, and a few of them deals with uptake by aragonite (e.g. Prieto et al. 2003, Godelitsas et al. 2003).

CHAPTER 2

SCOPE OF THE STUDY

2.1. Aim of This Work

The preliminary aim of this study is to investigate the kinetic aspect of the uptake of Ba^{2+}, Mn^{2+}, and Cd^{2+} ions by calcite and aragonite minerals over a wide range of concentrations at the stages of adsorption and precipitate overgrowth. In addition to that, the study includes morphologic and structural characterization of metal ion carbonates formed on calcite and aragonite. Atomic Absorption Spectrometry (AAS) and Inductively-Coupled Plasma Atomic Emission Spectrometry (ICP-AES) were used for the determination of aqueous concentrations of Ba^{2+}, Mn^{2+}, and Cd^{2+} ions. Quantitative X-ray Diffraction (XRD) was employed for elucidating the mass fraction of metal carbonates formed by precipitation as calcite and aragonite surfaces. For this purpose, equations were developed, based on relevant peak intensities of the metal carbonate and calcite or aragonite that can be used for direct determination of the carbonate binary mixtures. The distribution of the elements on the carbonate surface was recorded using the mapping analysis of Energy Dispersive X-ray Spectroscopy (EDS). Scanning Electron Microscope (SEM) was used to record the particle morphologies of different carbonate phases. The changes in vibrational modes of carbonate as a result of metal uptake were analyzed using Fourier Transform Infrared Spectroscopy (FTIR).

2.2. Applied Methods

2.2.1. Atomic Absorption Spectrometry (AAS)

Atomic Absorption Spectrometry (AAS) is applied for the identification of trace metals in a various environmental and biological matrices. The success of this technique is dependent not only to its sensitivity and selectivity but also its rate, simplicity, and

wide field of activity. Determination of more than six dozen elements can be achieved by Atomic Absorption technique. In general, the detection limit interval changes from few tenths to part per billion (in electrothermal atomization techniques) or from few tenths to part per million (in ordinary flame atomization) (Jenniss et al.1997).

Each element absorbs specific wavelength of light and they correspond to the energies needed to excite electrons from an energy level to other higher energy level. Atomic absorption spectrometry is used in various areas of chemistry.

Clinical analysis: AAS is used in analysing metals in biological fluids, eg. blood and urine.

Environmental analysis: The concentration levels of various elements found in air, drinking water, seawater, rivers, petrol and in drinks as beer, wine, and fruit drinks, can be determined by AAS.

Pharmaceuticals: Minor quantity of a catalyst (generally a metal) is used in some pharmaceutical manufacturing processes. In spite of being a catalyst, they are occasionally present in the final product and their amount can be determined by AAS.

Industry: AAS is widely used to examine many raw materials on account of determining the major elements present and the level of toxic impurities-e.g. where calcium is a major constituent, the lead level should be low because of its being toxic.

Mining: The amount of metals such as gold in rocks can also be determined by AAS to see whether the rocks are worth mining to extract the gold or not.

In AAS, atoms of different elements absorb characteristic wavelengths of light; therefore, the light of a particular element is used to understand if a sample contains the element of interest. The sample is atomized and emitted electromagnetic radiation is passed through vaporized sample. Since some of the radiation is absorbed by the analyzed atoms in the sample, the amount of absorbed radiation increases as the number of atoms increases in the vapor.

In principle, AAS instrument needs three components; a light source, a sample cell for the production of gaseous atoms, and a means of measuring the specific light absorbed. The main components of AAS instrument are given in Figure 2.1.

The common source of light is “hollow cathode lamp” containing a tungsten anode and a cylindrical hollow cathode made of the element to be determined which are sealed in a glass tube filled with an inert gas such as neon or argon at a pressure of

between 1 Nm^{-2} and 5 Nm^{-2}. The ionization of some gas atoms is provided by applying a potential approximately 300-400 V between the anode and the cathode.

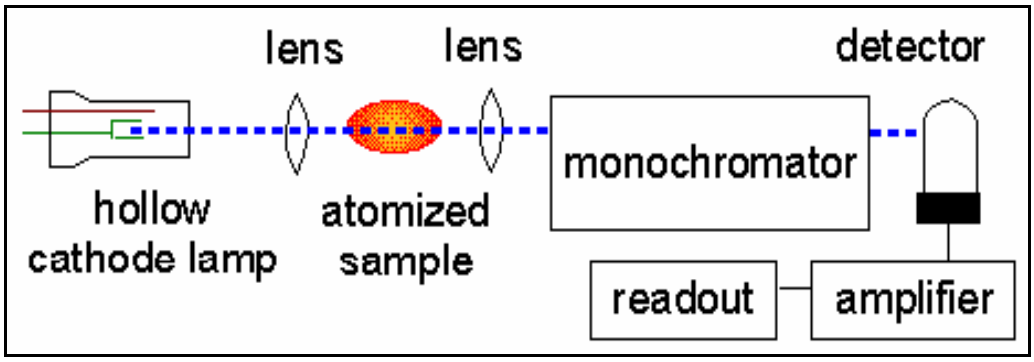

Figure 2.1. Instrumentation of AAS
(Source: WEB_7 2007)

In order to select the specific wavelength of light that is absorbed by the sample, a monochromator is used. The light selected by the monochromator is sent to detector which is typically a photomultiplier tube to produce an electrical signal proportional to the light intensity. On the other hand, commonly two systems are used to produce atoms from the sample: aspiration and electrothermal atomization. Aspiration includes sucking a solution of sample into a flame while the latter is where a drop is placed into a graphite tube and then heated electrically. In flame aspiration, most commonly selected gases as oxidant and fuel are compressed air and acetylene. The highest temperature obtained is about 2200^{o}C. Nitrous oxide (N_2O) which decomposes to give a 2:1 mixture of nitrogen and oxygen can be replaced the air for higher temperature values. The highest temperature it can gain is approximately 3000^{o}C when burning acetylene (Ewing 1985). In electrothermal atomization, the tube is heated by transferring a current through it in a series of steps which are programmed beforehand. In order to vaporize and atomize the samples, 5-10 seconds at 2000-2500^{o}C is sufficient. Almost 100% of the sample is atomized in electrothermal atomization; thus, the technique is much more sensitive than flame AAS.

2.2.2. Inductively Coupled Plasma-Atomic Emission Spectrometry (ICP-AES)

Inductively Coupled Plasma-Atomic Emission Spectrometry (ICP-AES) is an emission spectrophotometric technique in which the excited electrons belonging to elements of the analyzed sample emit energy at a given wavelength when they return to ground state. In this process, each element emits energy at specific wavelengths. Thus, in the ICP-AES technique, choosing a single wavelength for an element is widespread despite the fact that it emits energy at multiple wavelengths. There is a direct proportion between the intensity of the emitted energy at chosen wavelength and the concentration of analyzed sample; therefore, the elemental composition of this sample can be quantified by assessing the emitted wavelengths and their intensities (WEB_12 2007). The main components of ICP-AES instrument are given in Figure 2.2.

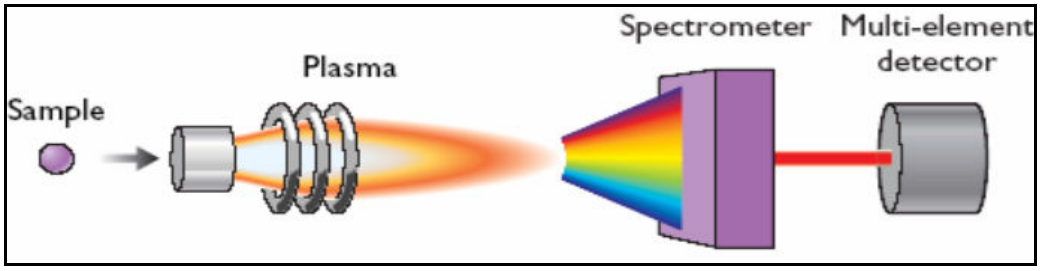

Figure 2.2. Instrumentation of ICP-AES
(Source: WEB_8 2007)

In ICP-AES analysis, the sample analyzed should be in solution; that's why, water can be analyzed simply by dilution. On the other hand, all ICP-AES systems are composed of several components which are grouped in three main parts: the sample introduction system, the torch assembly, and the spectrometer. The aqueous sample is pumped into the nebulizer and it produces an aerosol mist. Moisturized argon gas is injected into the chamber throughout the sample. The mist is collected in the spray chamber, where the larger mist particles are sent to waste and the appropriate particles are drifted into the torch. As a result, latter particles are injected vertically up to the length of the torch into the plasma with argon gas.

In order to produce vigorous atomic emission from chemical elements, the temperature should reach a value considerably above than those of simple flames. The

maximum value for the highest amount of atomic emission is reached in range between 7000 K and 10000 K. A way of obtaining these temperatures is to produce an inert-gas plasma. A gaseous state of matter involving free electrons and highly charged ions is called as "plasma" that is a very efficient environment for atomization and volatilization. A great many elements can be ionized efficiently (>90%). Nevertheless, no molecules and ground state elements are found in the plasma.

In the plasma, great amount of energy is transferred to the atoms and ions to elevate the excitation of higher energy levels. These excited atoms or ions emit electromagnetic radiation of specific wavelengths (λ) in the UV/VIS range of the spectrum when they come back to the ground state or lower excitation state. The light emitted from the plasma is focalized through a lens and sent to entrance slit into the spectrometer. The spectrometer can be either sequential (monochromator) or simultaneous (polychromator). The detector (photomultiplier tube) is set at the far end of the spectrometer (WEB_8 2007).

Because of its range and sensitivity, ICP-AES is analogous to flame atomic absorption spectrometry. Even though, some atomic absorption spectrophotometers able to measure up to five elements simultaneously, ICP-AES is more accommodating to simultaneous multielement determinations. Moreover, in decreasing the chemical interferences associated with atomic absorption spectrometry, the higher temperature of the plasma is a significant aspect (Jenniss et al.1997).

2.2.3. X-Ray Diffraction (XRD)

X-ray Diffraction (XRD), which enables information about structures, phases, preferred crystal orientations (texture) and other structural parameters such as average grain size, crystallinity, strain and crystal defects, is a vigorous and non-destructive technique for the characterization of crystalline materials. The production of X-ray diffraction peaks are caused by constructive interference of monochromatic beam that is scattered from each group of lattice planes at particular angles. The atomic decoration in the lattice planes provides the determination of peak intensities. As a result, the X-ray diffraction pattern is the fingerprint of periodic atomic regulations of materials. The main components of XRD instrument are given in Figure 2.3.

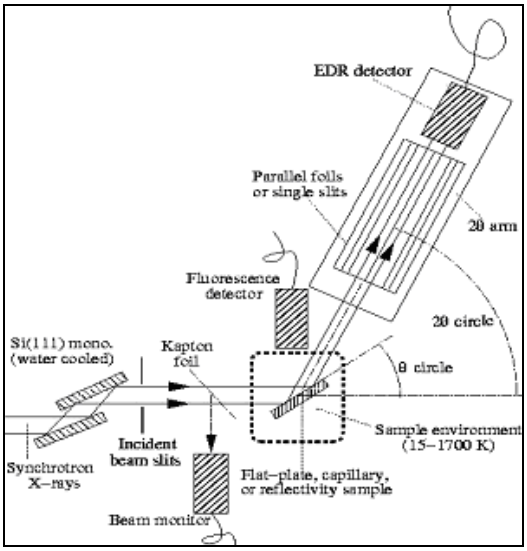

Figure 2.3. Instrumentation of XRD

(Source: WEB_9 2007)

In XRD, the X-ray beam is reflected from a plane crystal and by the change of theta angle the wavelength is selected (Figure 2.4). The reflected waves from successive crystal planes should pass twice across the space between planes; so, Bragg's equation is applied in this technique where n is the order of reflection, λ is the wavelength of X-ray radiation, d is the distance between adjacent planes in the crystal, and θ is the angle between incident beam and lattice plane (Ewing 1985). In general, as the symmetry of the material increases, the number of peaks in its diffraction pattern decreases and the intensity of each peak increases.

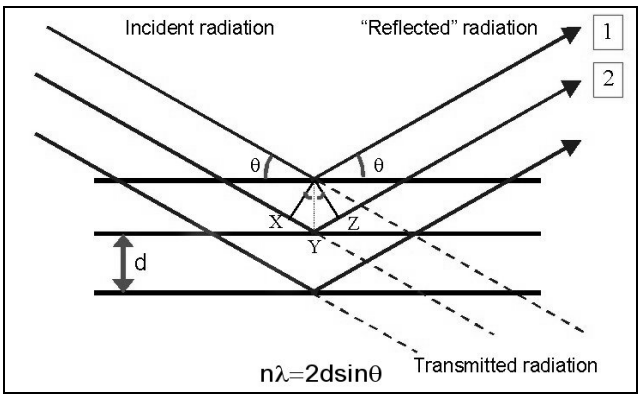

Figure 2.4. Illustration of Bragg's Law

(Source: WEB_10 2007)

High energy electrons irradiate the X-ray spectrum of a given material with continuous superimposed discrete lines. The transitions from the L to the K shell are specified as K_α X-rays. The transitions originating from different sublevels of the L shell are called as $K_{\alpha 1}$ and $K_{\alpha 2}$. In addition, X-rays owing to the transitions from M to the K shell is designated as K_β (Ewing 1985).

Quantitative XRD technique is usually applied to determine the amount of different phases in multi-phase samples. In quantitative analysis, an effort is to state the structural characteristics and phase proportions with quantifiable numerical precision by use of the experimental data itself. Present XRD techniques for this analysis depend on four methods which are analyzing based on peak areas, usage of the same mass absorption coefficient method, mineral diagnosing based on an internal standard, and quantitative mineral appraisement by use of external standard, respectively. It is known that there is a proportion between the intensities of the XRD pattern of an individual mineral and concentrations of the different minerals present. Thus, some idea about the relative quantities of each phase can be obtained by measuring the intensities of patterns (Ouhadi and Yong 2003).

2.2.4. Scanning Electron Microscope (SEM)

SEM is a surface determination technique which is applied to get a physical picture of the topology of the surface on a microscopic scale. Especially, the smoothness of the surfaces is revealed by an optical microscope. SEM is an essential technique since it gives information about the surfaces which involve details of grain or crystal boundaries, lattice deficiencies, foreign inclusions, and other microphysical data (Strobel and Heineman 1989). The main components of SEM instrument are given in Figure 2.5.

In this device, the surface of the sample is scanned in a rectangular raster by a finely focused beam of electrons. By the interaction with the specimen, electron beam yields various products such as reflected or backscattered primary electrons, slowly moving (secondary) ejected electrons, Auger electrons, and X-rays. In this technique, either reflected or secondary electrons are produced along the surface of the sample in a good fraction. Should the secondary electrons supply the intensity data, the detector located at a low angle to the primary beam collects them.

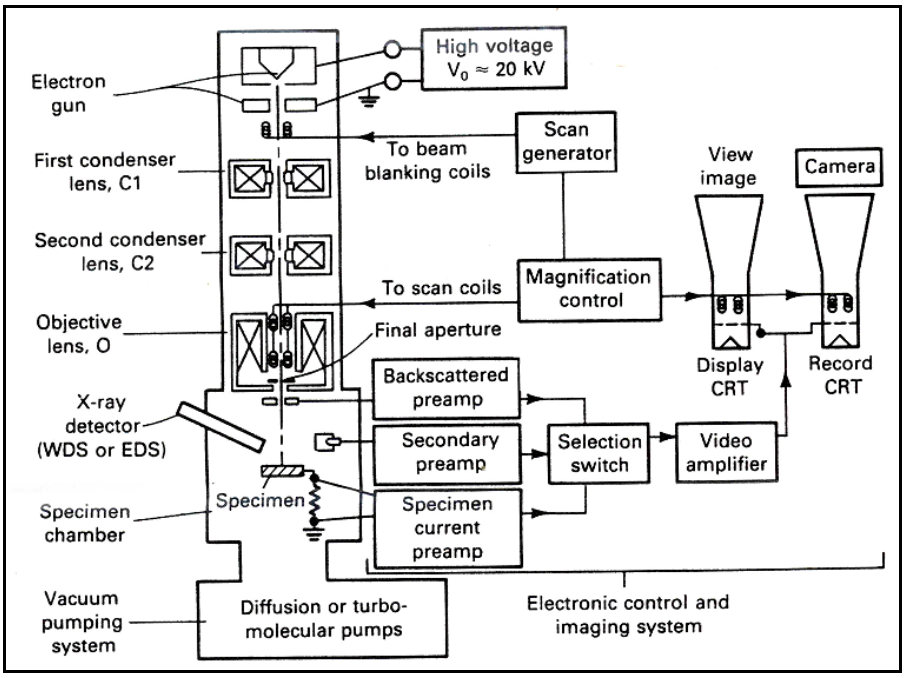

Figure 2.5. Instrumentation of SEM

(Source: WEB_11 2006)

In the instrument, the potential applied on the electrodes of the gun causes stream of emitted electrons which then pass through magnetic lenses. The electron optics of the device is formed by the collection of lenses and apertures. A high vacuum is required in an electron microscope because electron beams are vigorously absorbed or scattered by molecules in air. The secondary electrons arising from a spot on the sample generally interact with scintillator and are detected by photomultiplier tube. Finally, the image is displayed on the CRT monitor (Strobel and Heineman 1989).

2.2.5. Energy Dispersive X-Ray Spectroscopy (EDS)

EDS is a technique to determine elements and their surface concentrations in a sample. Generally, Si(Li) module is utilized as an energy-dispersive X-ray detector and characteristic X-ray wavelength of an element is detected. There is a proportion between local concentration of the analyte and the indirect X-ray image of the surface developed intensity (Strobel and Heineman 1989).

In EDS technique, the dispersion of energy depends on the availability of a detector which replies linearly the energy content of separate photons. Those detectors,

which are capable of measuring photon energies, are called as scintillation counters, gas counters worked at a median range of voltages, and lithium-drifted silicon or germanium detectors. Separate counting of signal pulses of successive energy brackets is permitted by a series of electronic energy discriminators which are used to analyze the signal from the solid-state detector. The pulses correspond to photons come randomly (Ewing 1985). The elemental concentration for the top 1000 nm is represented with SEM to which an energy-dispersive X-ray spectrometer is connected (Strobel and Heineman 1989).

2.2.6. Fourier Transform Infrared Spectroscopy (FTIR)

Infrared Spectroscopy is the study of the interaction between infrared light and matter. When infrared (IR) radiation interacts with matter, it can be absorbed by causing the vibration of chemical bonds in the material. The functional groups which are known as the chemical structural fragments within molecules tend to absorb IR radiation in the same wavenumber range; however, the structure of the rest of the molecule may not be in this range. There is a connection between the molecule's structure and the wavenumbers at which a molecule IR radiation. This relation allows the structure of unknown molecules to be identified form the molecule's IR spectrum; that's why, IR spectroscopy is a useful chemical analysis tool (Smith 1996).

An FTIR instrument is composed of an IR source, an interferometer, a sample container, a detector, and a computer as shown in Figure 2.6.

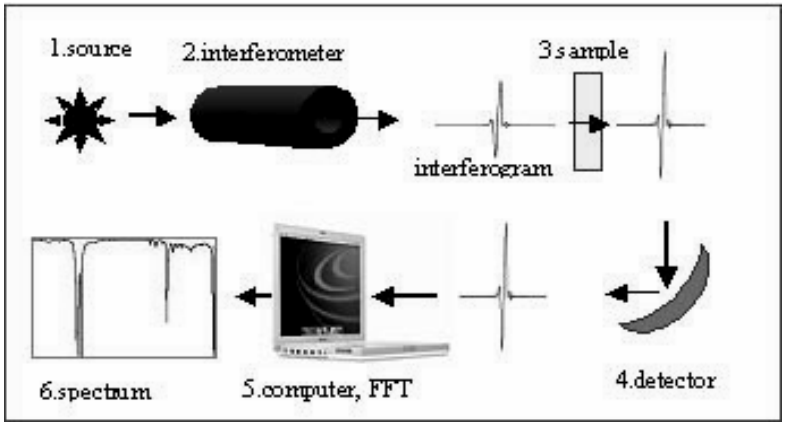

Figure 2.6. Instrumentation of FTIR
(Source: WEB_12 2007)

One of the important features of FTIR is the speed of this technique. In stead of spending several minutes, most measurements by FTIR are made in a matter of seconds since all of the frequencies are measured simultaneously. In addition, it is a very sensitive technique due to the detectors employed and the optical throughput is much higher which results in much lower noise levels. Moreover, these instruments are self-calibrating. As a result of these advantages, making measurements by FTIR is extremely accurate and reproducible.

CHAPTER 3

EXPERIMENTAL

3.1. Preparation of Samples

Throughout this study the batch method was applied. Calcite used in this study was obtained from Carlo Erba, while aragonite was synthesized in the laboratory. XRD characterization showed that calcite mineral contained a minor amount of aragonite while aragonite synthesized in the laboratory was pure. According to SEM images calcite particles showed indefinite morphology with variable size (5-15 μm), while aragonite possessed rod-like morphology with a crystal size of 5-10 μm.

3.1.1. Aragonite Synthesis

In order to synthesize aragonite, 1 liter solution of 0.10 M $CaCl_2$ (ALDRICH 22,231-3) and 0.20 M $MgCl_2.6H_2O$ (SIGMA-ALDRICH 7791-18-6) was prepared in the same volumetric flask. After that, this solution was transferred to 1.0 L Erlenmeyer flask and placed in Multimatics 9S water bath whose temperature was adjusted to 60^oC, beforehand. The solution was stirred in water bath until it came to thermal equilibrium (approximately 2 hours).

On the other hand, 100 ml of 1.0 M of Na_2CO_3 (ALDRICH 22,353-0) solution was prepared and placed into the water bath. After reaching to thermal equilibrium, this solution was added to $CaCl_2$-$MgCl_2$ solution by using a peristaltic pump at a rate of 1.67 mL/min. The white precipitate which had a pH value of 8.6 was stirred in water bath for 30 minutes. Then, the precipitate was separated by vacuum filtration and washed several times with distilled water. Finally, the filtrated solid particles were allowed to dry in an oven adjusted at 110^oC, beforehand.

The white precipitate was characterized using XRD analyses which showed it to be entirely composed of aragonite. The powders were stored under dry conditions for later use in the uptake experiments.

3.2. Determination of Zero Point Charge (ZPC) of Calcite and Aragonite

In order to identify the surface potential of either calcite or aragonite mineral at different pH values, zero point charge (ZPC) determination experiments were performed by using ZETA-METER 3.0+ instrument. First of all, six samples were prepared for each mineral with pH ranging from 7.0 to 12.0. For this purpose, 0.10 g samples of calcite or aragonite powders were prepared and 100 ml of distilled water was added in each. Then, the pH values were adjusted to intended value by using 1.0 M or 0.10 M of HCl and NaOH. Immediately after the pH adjustment, the sample was poured into the GT-2 Type electrophoresis cell of Zeta-Meter.

In the instrument system, Molybdenum Cylinder Anode and Platinum Rod Cathode electrodes are used. Then, the cell was positioned on the floor of the microscope. The clearness of ocular micrometer containing tracking lines was regulated by focusing the illuminators and microscope. After that, a voltage is applied to electrodes in order to observe the tracking of particles through tracking lines. This voltage is selected according to the maximum allowable specific conductance of sample. The K factor was adjusted to 64 because of using Molybdenum anode. According to the velocities of particles passing through tracking lines, either full scale or quarter scale measurements could be performed. For the measurement, a particle was selected and when it passed through a grid line, “track” button was pressed on the keypad according to the passing direction, and it was hold down until the particle crossed the next grid line. An average of 20 measurements was taken for each sample. Following these measurements, pH versus zeta potential plot was constructed and ZPC value was identified at the point where it intersected the pH axis.

3.3. Particle Size Analysis

Particle size of calcite and aragonite minerals were determined by using Micrometrics SediGraph 1500 type instrument located at the Department of Chemical Engineering at İzmir Institute of Technology. At first, dry sieving was performed to obtain particles with size les than 38 μm. Next, the particles less than this size were prepared in a 50 ml Calgon solution involving %0.65 by volume solid sample. Then, the

samples were placed in the ultrasonic bath for 15 minutes. After this time period, the particle size range was selected between 0.5 μm and 100 μm. The density values of calcite and aragonite minerals were chosen as 2.710 g/cm^3 and 2.935 g/cm^3, respectively. Cell temperature was selected as 37.4^{o}C and analysis period was 10 minutes.

3.4. BET Analysis

In order to determine the surface area and pore size of calcite and aragonite minerals, BET and Langmuir analysis were performed by using Micromeritics Gemini V instrument. For the analysis, degas conditions were adjusted to 120^{o}C and 3 hours. Saturation pressure was 1014.810 mbar. The mass of calcite and aragonite samples were 0.1568 g and 0.0941 g, respectively.

3.5. Uptake Experiments

3.5.1. Kinetic Experiments

These experiments were carried out in a wide concentration range. In each experiment, 25.0 ml aliquots of $BaCl_2.2H_2O$ (SIGMA-ALDRICH 10326-27-9), $MnCl_2$ (ALDRICH 7773-01-5), or $CdCl_2.5/2H_2O$ (SIGMA 7790-78-5) solutions were mixed with 0.25 g samples of calcite or aragonite powders using a thermostat multi-position magnetic stirrer (Selecta, Multimatic 9S). The initial concentrations were 10.0, 50.0, 100.0, 500.0, 1000.0, 5000.0, and 10000.0 mg/L and the experiments were carried out at ambient temperature and pressure for time periods ranging from 30 minutes up to 3 weeks. The flasks containing the samples which open to atmosphere were stirred up to 7 hours. Then, each flask was covered and left for time periods ranging from 24 hours to 3 weeks. At the end of the mixing period, the solid phase was separated from solution by filtration and dried at room temperature. All the experiments were performed in duplicates. The pH values of the solutions were measured before and after the experiments. The measured values are given in Table 3.1, 3.2, and 3.3. As it is expected, the pH value decreases as the concentration of the cation increases.

Table 3.1. Initial and final pH values of solutions of Ba^{2+} in contact with calcite or aragonite at different initial concentrations and contact times. The temperature of the medium was 25°C.

MINERAL	TIME	100 mg/L		500 mg/L		1000 mg/L		5000 mg/L		10000 mg/L	
		pH_i	pH_f	pH_i	pH_f	pH_i	pH_f	pH_i	pH_f	pH_i	pH_f
CALCITE	**10 min**	8.4		8.1		8.2		7.9		7.7	
	30 min	8.5		8.2		8.4		8.0		7.9	
	1 h	8.3	7.9	8.2	7.7	8.2	7.1	7.8	7.0	7.7	7.1
	4 h	8.5	7.7	8.3	7.5	8.0	7.5	7.7	7.1	7.6	7.0
	7 h	8.6	7.9	8.3	7.7	8.2	7.4	8.1	6.9	7.8	6.8
	24 h	8.3	8.0	8.1	7.9	8.0	7.2	7.8	6.9	7.6	6.8
	48 h	8.4	7.8	8.1	7.5	7.2	7.6	7.3	7.0	7.2	6.9
ARAGONITE	**10 min**	8.8		8.5		8.2		7.9		7.7	
	30 mi	8.2		8.3		8.3		7.9		7.7	
	1 h	8.8	8.0	8.7	7.6	8.3	7.6	7.9	7.1	7.7	6.8
	4 h	8.6	7.6	8.3	7.5	8.3	7.9	7.2	7.1	7.5	6.9
	7 h	8.7	7.9	8.7	7.7	8.4	7.8	8.0	7.4	7.9	6.9
	24 h	8.9	7.9	8.5	7.6	8.3	7.6	7.9	7.2	7.6	6.8
	48 h	8.9	7.8	8.6	7.6	8.3	7.5	7.9	7.2	7.7	6.8

Table 3.2. Initial and final pH values of solutions of Mn^{2+} in contact with calcite or aragonite at different initial concentrations and contact times. The temperature of the medium was 25°C.

MINERAL	TIME	100 mg/L		500 mg/L		1000 mg/L		5000 mg/L		10000 mg/L	
		pH_i	pH_f	pH_i	pH_f	pH_i	pH_f	pH_i	pH_f	pH_i	pH_f
CALCITE	**10 min**	9.7		9.2		9.2		8.9		8.9	
	30 min	9.7		9.2		9.2		8.9		8.9	
	1 h	9.7	9.0	9.2	8.6	9.2	8.6	8.9	8.5	8.9	8.2
	4 h	9.7	8.3	9.2	8.5	9.2	8.5	8.9	7.8	8.9	7.4
	7 h	9.7	8.2	9.2	6.5	9.2	7.9	8.9	7.2	8.9	6.8
	24 h	9.7	8.0	9.2	7.7	9.2	8.0	8.9	7.6	8.9	7.2
	48 h	9.7	8.0	9.2	8.1	9.2	8.0	8.9	7.5	8.9	7.4
ARAGONITE	**10 min**	9.7		9.6		9.4		8.6		8.4	
	30 min	9.7		9.6		9.4		8.6		8.4	
	1 h	9.7	9.6	9.6	9.2	9.4	8.7	8.6	8.1	8.4	8.4
	4 h	9.7	8.8	9.6	8.3	9.4	8.0	8.6	7.4	8.4	7.5
	7 h	9.7	8.5	9.6	8.1	9.4	7.9	8.6	7.4	8.4	7.3
	24 h	9.7	8.3	9.6	8.1	9.4	7.8	8.6	7.3	8.4	7.2
	48 h	9.7	8.4	9.6	8.1	9.4	7.8	8.6	7.3	8.4	7.1

Table 3.3. Initial and final pH values of solutions of Cd^{2+} in contact with calcite or aragonite at different initial concentrations and contact times. The temperature of the medium was 25°C.

MINERAL	TIME	100 mg/L		500 mg/L		1000 mg/L		5000 mg/L		10000 mg/L	
		pH_i	pH_f	pH_i	pH_f	pH_i	pH_f	pH_i	pH_f	pH_i	pH_f
CALCITE	**10 min**	8.4		7.3		6.8		6.7		6.7	
	30 min	8.5		7.6		6.9		6.7		6.8	
	1 h	8.7	8.4	7.2	7.8	6.6	7.9	6.6	6.4	6.3	6.4
	4 h	8.4	8.2	7.2	7.8	6.7	7.8	6.3	6.4	6.4	6.3
	7 h	8.3	7.9	7.3	7.8	6.7	7.8	6.6	6.5	6.3	6.4
	24 h	8.3	8.2	7.6	8.0	6.7	7.7	6.4	6.5	6.3	6.5
	48 h	8.4	7.8	7.2	7.6	6.7	8.0	6.5	6.6	3.2	6.5
ARAGONITE	**10 min**	7.4		7.3		6.6		6.3		6.2	
	30 min	8.3		7.3		7.4		6.5		6.5	
	1 h	7.0	8.0	6.9	7.5	6.7	8.0	6.4	7.3	6.3	6.6
	4 h	7.3	7.7	6.7	7.4	8.1	7.8	6.1	7.2	6.0	6.7
	7 h	7.4	8.0	6.7	7.8	8.3	7.9	6.6	7.3	6.3	6.6
	24 h	7.6	8.2	7.0	7.9	8.0	7.8	6.5	7.6	6.0	6.6
	48 h	7.6	8.2	7.0	7.8	7.2	7.7	6.3	7.4	6.0	7.1

3.5.2. Dependence of Metal Uptake on Temperature Change

In order to study the effect of temperature on the extent of uptake, 25.0 ml aliquots ion solutions were mixed with 0.25 g samples of calcite or aragonite powders using a thermostat multi-position magnetic stirrer (Selecta, Multimatic 9S) adjusted to 50°C, beforehand. The initial concentrations were 10.0, 50.0, 100.0, 500.0, 1000.0, 5000.0, and 10000.0 mg/L and the experiments were carried out at ambient pressure. At the end of the 24 hours mixing period, the solid phase was separated from solution by filtration and dried at room temperature. The measured initial and final pH values are given in Table 3.4 and 3.5.

Table 3.4. The pH change of Ba^{2+}, Mn^{2+}, and Cd^{2+} cations during interactions with calcite at different initial cation concentrations and 50°C.

CATION	10 mg/L		50 mg/L		100 mg/L		500 mg/L		1000 mg/L		5000 mg/L		10000 mg/L	
	pH_i	pH_s	pH_i	pH_s	pH_i	pH_s	pH_i	pH_s	pH_i	pH_s	pH_i	pH_s	pH_i	pH_s
Ba^{2+}	9.6	8.3	9.6	8.3	9.6	8.3	9.5	8.3	9.4	7.8	9.3	8.9	9.1	9.7
Mn^{2+}	9.1	8.1	8.7	7.8	8.6	7.7	8.3	7.6	8.1	7.4	7.8	6.9	7.7	6.8
Cd^{2+}	9.1	8.1	8.7	8.1	7.8	7.8	7.3	8.0	6.7	8.0	6.2	6.3	6.1	5.9

Table 3.5. The pH change of Ba^{2+}, Mn^{2+}, and Cd^{2+} cations during interactions with aragonite at different initial cation concentrations and 50°C.

CATION	10 mg/L		50 mg/L		100 mg/L		500 mg/L		1000 mg/L		5000 mg/L		10000 mg/L	
	pH_i	pH_s	pH_i	pH_s	pH_i	pH_s	pH_i	pH_s	pH_i	pH_s	pH_i	pH_s	pH_i	pH_s
Ba^{2+}	9.8	8.4	9.8	8.6	9.8	8.2	9.7	7.8	10.2	8.3	10.1	7.7	10.1	7.5
Mn^{2+}	9.4	8.3	9.0	8.0	8.8	7.7	8.5	7.4	8.2	7.4	7.9	7.1	7.1	6.4
Cd^{2+}	9.4	8.5	7.9	8.3	7.3	8.2	7.4	7.9	7.6	7.8	6.2	8.0	6.0	7.3

3.5.3. Dependence of Metal Uptake on pH Change

In another set of experiments, the initial pH value was adjusted to 10.0 by using 0.50 M NaOH and 0.50 M HCl. In each experiment, 25.0 ml aliquots ion solutions were mixed with 0.25 g samples of calcite or aragonite powders. The aim of these experiments was to check the effect of pH on the extent of precipitation of metal ions. The initial concentrations were 1000.0, 5000.0, and 10000.0 mg/L and the experiments were carried out at ambient temperature and pressure. At the end of the 24 hours mixing period, the solid phase was separated from solution by filtration and dried at room temperature. Before filtration, the pH values were measured and given in Table 3.6.

Table 3.6. The pH values of the samples before filtration in the experiments carried out at pH of 10.0 at various initial concentrations.

MINERAL	CATION	1000 mg/L		5000 mg/L		10000 mg/L	
		pH_i	pH_s	pH_i	pH_s	pH_i	pH_s
CALCITE	Ba^{2+}	10.0	8.3	10.0	8.1	10.0	9.9
	Mn^{2+}	10.0	8.2	10.0	9.5	10.0	9.4
	Cd^{2+}	10.0	8.8	10.1	9.4	10.1	9.4
ARAGONITE	Ba^{2+}	10.0	8.4	10.1	8.0	10.1	8.1
	Mn^{2+}	10.1	8.9	10.1	9.0	10.1	9.7
	Cd^{2+}	10.1	9.8	10.0	9.4	10.0	9.2

3.6. Analysis of Aqueous Solutions

3.6.1. AAS

Thermo Elemental SOLAAR M6 Series Atomic Absorption Spectrometer with air-acetylene flame was used to determine aqueous barium, manganese, and cadmium concentrations. The hollow cathode lamp used in the instrument for the determination of Ba, Mn, Cd concentrations operated at the wavelengths of 553.6, 279.5, and 228.8 nm, respectively.

3.6.2. ICP-AES

A Varian Liberty Series II Axial view ICP-AES was used in the determination of aqueous barium, manganese, cadmium, and lead concentrations. ICP-AES instrument was operated with incident power of 12 kW, plasma gas flow rate of 15 L/min, and auxiliary gas flow rate of 1.5 L/min. Continuous nebulization was achieved by means of a concentric glass nebulizer with cyclonic chamber. The sampling flow rate was 1.0 mL/min. Measurements were based on peak height with polynomial plotted background

correction method. In instrument, two wavelengths were chosen for each element which were 233.527 nm and 493.409 nm for Ba^{2+}, 293.930 nm and 259.373 nm for Mn^{2+}, 214.438 m and 226.502 nm for Cd^{2+}, and 317.933 nm and 422.673 nm for Ca^{2+}, respectively.

3.7. Characterization of the Solid

3.7.1. XRD

XRD analysis was performed using a Philips X'Pert Pro instrument which is situated at Center of Material Research at Izmir Institute of Technology. The samples were first ground, mounted on zero background sample holder then introduced for analysis. The source consisted of Cu K_α radiation (λ=1.54 Å). Each sample was scanned within the 2 theta range of 10-50. In XRD quantification analysis, $BaCO_3$ (ALDRICH cas:513-77-9), (SIGMA-ALDRICH cas:598-63-0), $MnCO_3$ (ALDRICH cas:598-62-9), and $CdCO_3$ (ALDRICH cas:28,914-0) solids were each mixed with calcite or aragonite in a way that the mixture would contain 10.0%, 20.0%, 30.0%, 40.0%, 50.0%, 60.0%, 70.0%, 80.0% and 90.0% by mass of the metal carbonate and have total mass of 1.0 gram. XRD analysis of each mixture was performed based on the basic reflections of metal carbonates, calcite, and aragonite. The peak areas were found using MS Origin 5.0, and the ratios of $I_{MeCO3}/I_{calcite}$ or $I_{MeCO3}/I_{aragonite}$ were calculated. From these peak ratios, a calibration plot was formed by drawing the peak ratios versus metal carbonate percentage. These plots were finally fitted using MS Excel to obtain the representative equations.

3.7.2. SEM/EDS

SEM/EDS characterization was carried out using a Philips XL-30S FEG type instrument. Prior to analysis, the solid samples were sprinkled onto adhesive aluminum tapes supported on metallic disks. Images of the sample surfaces were then recorded at different magnifications. Elemental EDS analysis was performed at randomly selected areas on the solid surfaces each being approximately 100μm×100μm in dimension. EDS

mapping was carried out at magnification of x1000 and applied the voltage was 18 kV under vacuum conditions of $3.5x10^{-5}$ mbar.

3.7.3. FTIR

FTIR spectra of the samples were collected in the middle IR region, 400-4000 cm^{-1}, using a Nicolet Magna 550 type instrument. After mixing with KBr, the samples were introduced as pellets and KBr powder was used as a background. A total of 32 scans were recorded with a resolution of 4 cm^{-1} for each spectrum. Omnic 1.3 software was used to process the results.

3.8. Chemical Speciation Analysis

The chemical speciation analysis of aqueous Ba^{2+}, Mn^{2+}, Cd^{2+}, and Pb^{2+} ions were performed using visual MINTEQ software. By use of this software, it is possible to obtain theoretical knowledge about chemical speciation of the ions at various concentrations, pH, temperature, and ionic strength values. For the purpose of illustrations, the chemical speciation curves of Ba^{2+}, Mn^{2+}, and Cd^{2+} in aqueous solution at initial concentration of 1000.0 mg/L and other specified conditions are given in Figure 3.1.

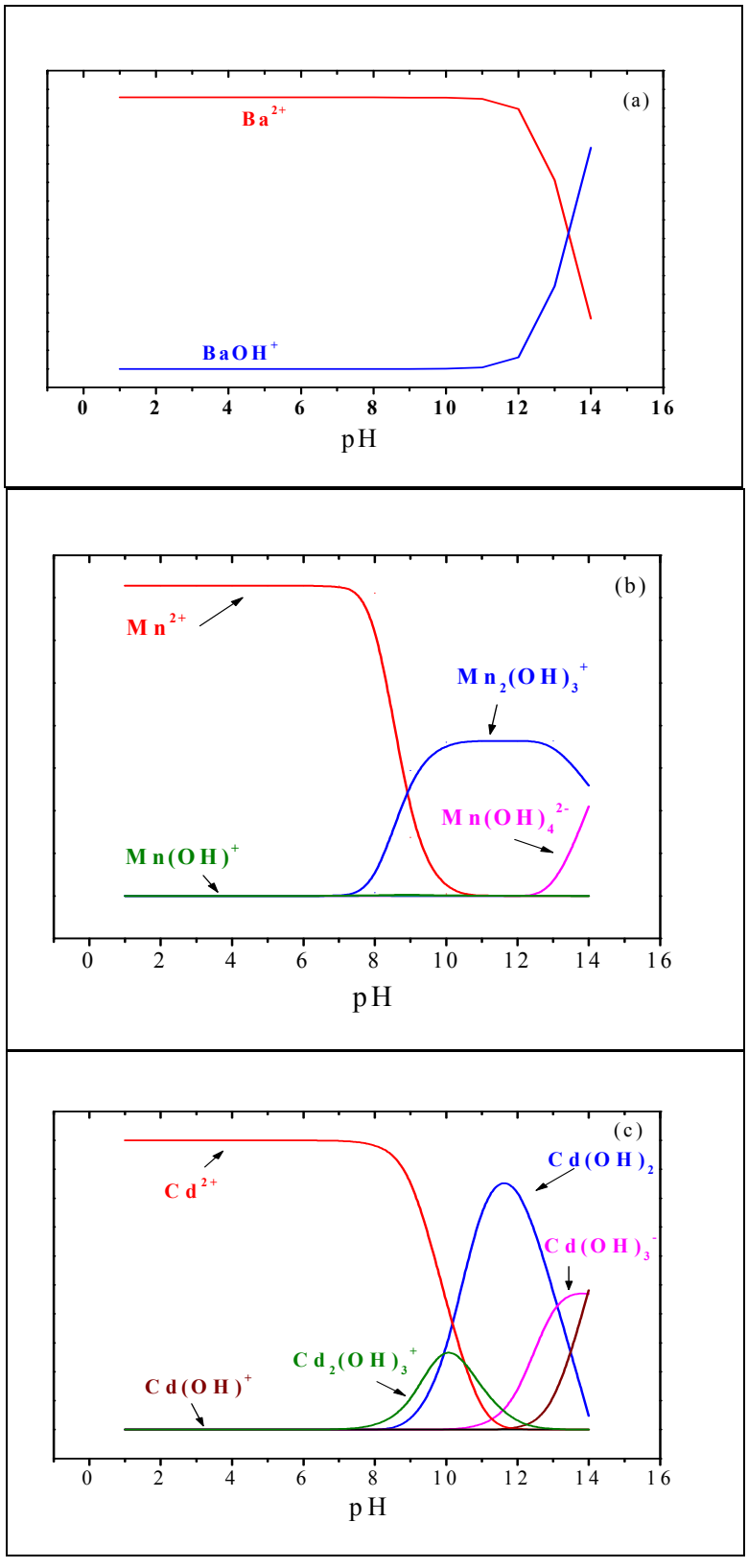

Figure 3.1. Chemical speciation curves of (a) Ba^{2+}, (b) Mn^{2+}, and (c) Cd^{2+} at initial concentration of 1000 mg/L in aqueous solution. Ionic Strength (I): 0.001 and Temperature (T): 25°C.

CHAPTER 4

RESULTS AND DISCUSSION

4.1. Characterization of Calcite and Aragonite

The XRD diagrams showed that the purity of calcite and aragonite minerals used in the experiments to be very high. Typical XRD diagrams of calcite and aragonite are given in Figure 4.1. The basic reflections of each mineral are labeled.

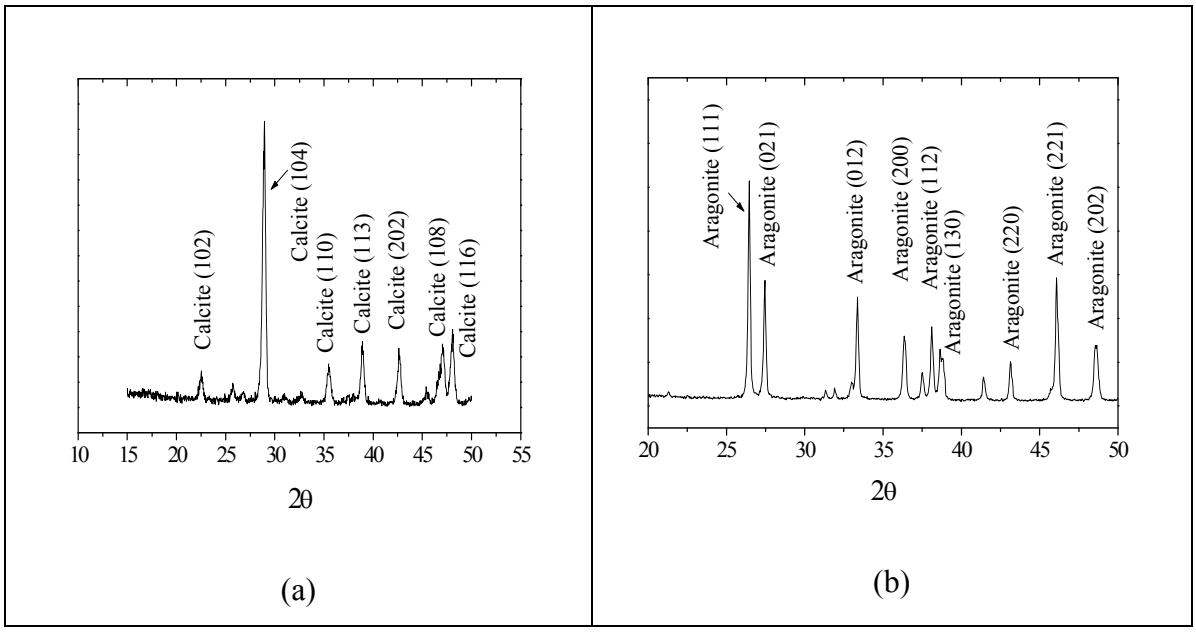

Figure 4.1. XRD diagrams of (a) calcite and (b) aragonite used in this work.

According to SEM characterization, calcite particles possess indefinite morphological structure with particle size ranging from 5 μm to 15 μ. On the other hand, aragonite mineral have a rod-like crystal structure with particle size ranging from 5 μm to 10 μm. Typical SEM images of calcite and aragonite are given in Figure 4.2.

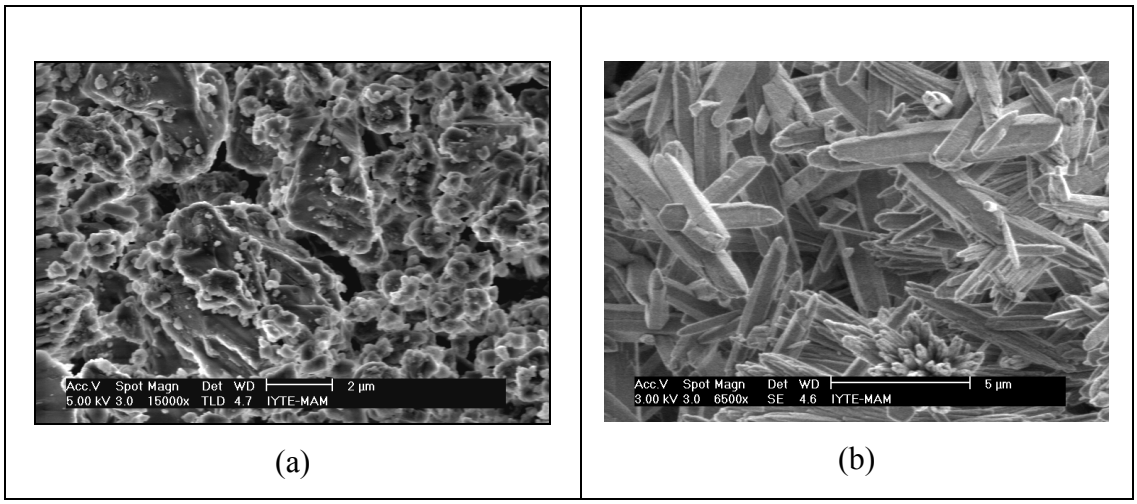

Figure 4.2. Characteristic SEM images of (a) calcite and (b) aragonite.

As mentioned in section 3.1.1 $MgCl_2$ was used in the synthesis of aragonite mineral. In order to check the elemental contents of aragonite and calcite mılti-spot, EDS analysis are performed. Typical EDS spectra are given in Figure 4.3. The elemental contents are also provided in and Table 4.1. Mg^{2+} ions are used in aragonite synthesis to avoid crystallization of $CaCO_3$ into calcite. The results indicate that Mg^{2+} content in aragonite is very small suggesting that this ion affects $CaCO_3$ crystallization in the solution with minimal amount entering the solid structure of the mineral.

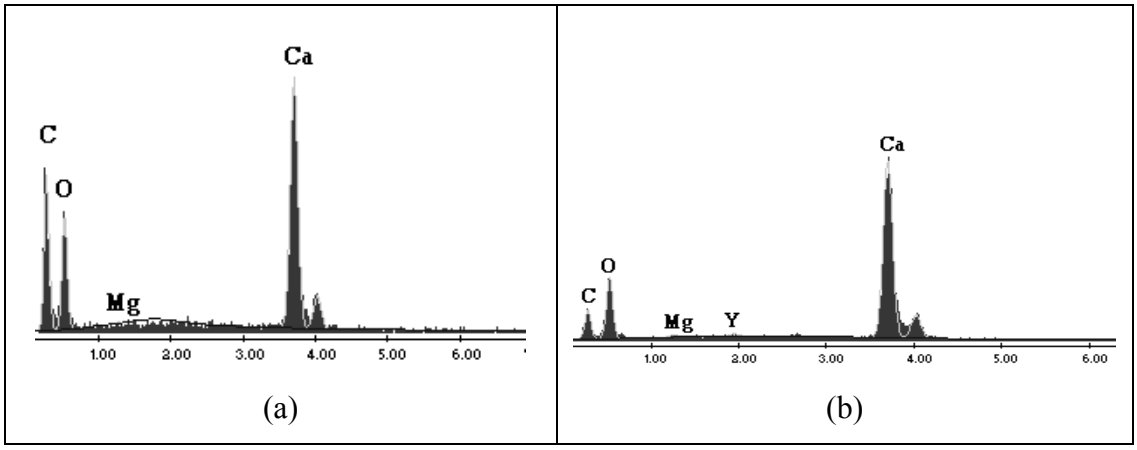

Figure 4.3. EDS spectra of (a) calcite and (b) aragonite.

Table 4.1. Elemental content of calcite and aragonite obtained by EDS analysis.

MINERAL	C		O		Mg		Ca	
	Atom %	Mass %	Atom %	Mass %	Atom %	Mass %	Atom %	Mass %
CALCITE	37.01	23.50	42.64	35.32	0.15	0.19	20.20	40.99
ARAGONITE	24.93	14.31	50.21	38.29	0.43	0.49	24.26	46.28

In particle size analysis, the particles greater than 38.0 µm were exposed to dry sieving. The percent mass fraction values of these particles are 50.2% and 42.8% for calcite and aragonite, respectively. The particle size distribution of calcite and aragonite for particles below 38.0 µm is shown in Figure 4.4. The mean, median, mode, and standard deviation of the obtained distribution are given in Table 4.2. Based on the data obtained, it was determined that 74.4% mass fraction of calcite and 71.2% mass fraction of aragonite had a particle size less than 10.0 µm.

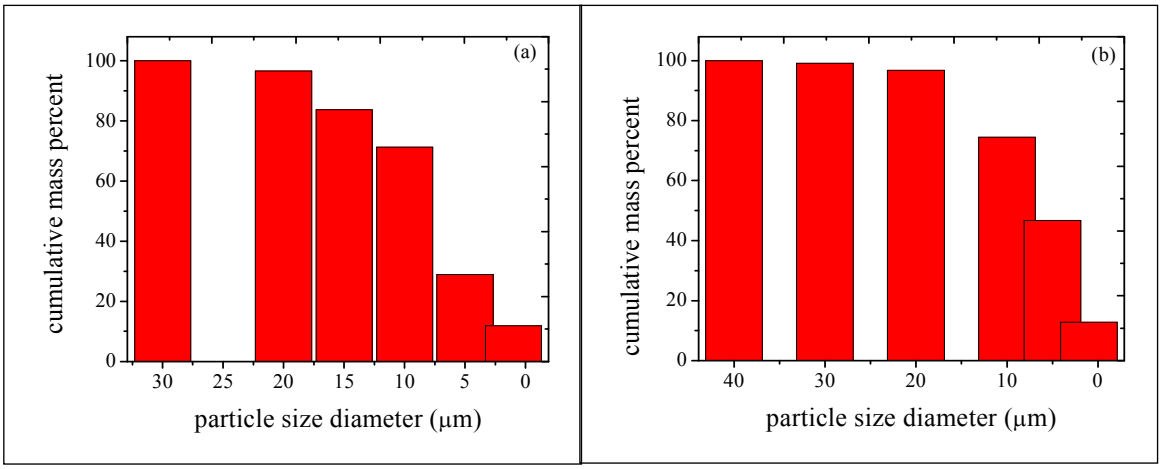

Figure 4.4. Particle size distribution (for particles less than 38 µm) for: (a) calcite and (b) aragonite.

Table 4.2. Mean, median, mode, and standard deviation for particle size analysis of calcite and aragonite minerals.

MINERAL	PARTICLE DIAMETER (µm)			
	Mean	Median	Mode	Standard Deviation
CALCITE	7.633	5.867	6.310	7.928
ARAGONITE	7.350	4.473	8.414	9.145

The Zeta potential of calcite and aragonite was measured at various pH values in order to determine the Zero Point of Charge (ZPC) of each mineral. Based on the values given in literature, calcium carbonate is reported to have ZPC values varying from 8.2 to 11.0 (Kosmulski 2001, Moulin and Roques 2003). This variation is thought to be caused by the pressure of carbon dioxide gas (PCO_2) which enables partial transformation of CO_3^{2-} to HCO_3^- released by dissolution of solid until gas-liquid equilibrium is satisfied in the system (Moulin and Roques 2003). The zeta potential variation of calcite and aragonite with respect to pH is shown in Figure 4.5. According to the obtained data, ZPC of calcite and aragonite are achieved at the pH values of 10.59 and 10.55, respectively. Below these values, the surface is positively charged and above them it is negatively charged.

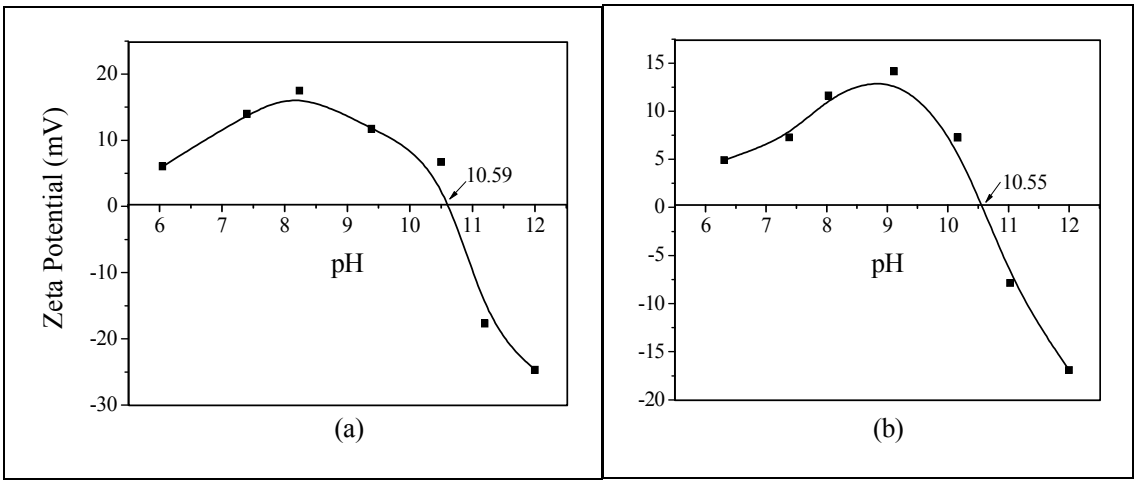

Figure 4.5. Variation of zeta potential with respect to pH for (a) calcite and (b) aragonite.

The surface area and pore size of calcite and aragonite were also determined using BET-N_2 analysis. The results are given in Table 4.3. The surface area of aragonite appears to be almost twice that of calcite.

Table 4.3. Results of surface area and pore size values of calcite and aragonite

MINERAL	BET Surface Area (m^2/g)	Langmuir Surface Area (m^2/g)	Pore Size (Å)
CALCITE	34.5	134.2	33.6
ARAGONITE	57.5	223.6	33.6

4.2. Kinetic and Equilibrium Description of Metal Adsorption on Calcite and Aragonite

4.2.1. Kinetics

In order to determine the rate of sorption, solutions containing 100 mg/L and 500 mg/L Ba^{2+}, Mn^{2+}, and Cd^{2+} ions were stirred with calcite and aragonite minerals at room temperature and ambient pressure for different time intervals. The results obtained from these studies are given in Figure 4.6 and 4.7. The sorption of Cd^{2+} ions approaches equilibrium in 30 minutes in both concentrations and this observation is valid for both calcite and aragonite mineral. Nevertheless, longer time periods are required for Ba^{2+} and Mn^{2+} ions to reach equilibrium. The sorption process of Mn^{2+} ions attains equilibrium within 6 or 7 hours on both of calcite and aragonite minerals. In the case of Ba^{2+} at initial concentration of 100 mg/L, equilibrium is reached within 1 hour while as the concentration is increased to 500 mg/L, several hours are required to approach equilibrium.

In order to determine the kinetic rate constants, three models that are widely used in sorption studies were applied. The models include first order rate equation, Lagergren's model (Lagergren 1898), second order rate equation (Ho and Mckay 1998), and Elovich equation (Han et al. 2006). The equations of these model are, respectively, given as:

$$q_t = q_e(1 - \exp(-k_1 t)) \tag{4.1}$$

$$q_t = \frac{k_2 q_e^2 t}{1 + k_2 q_e t} \tag{4.2}$$

$$q_t = \frac{\ln(\alpha\beta)}{\beta} + (\frac{1}{\beta})\ln t \tag{4.3}$$

In the equations, q_t refers to the ion concentration on calcite or aragonite minerals at a certain time, whereas, q_e represents the ion concentration at equilibrium. In addition, the constants k_1 (min^{-1}) and k_2 ($g.mg^{-1}.min^{-1}$) in the equations represent the first order and second order rate constants, respectively. In Elovich equation, α (mg sorbate/mg sorbent.min) and β (g sorbent/mg sorbate) are parameters related to initial sorption rate and surface covering capacity, respectively.

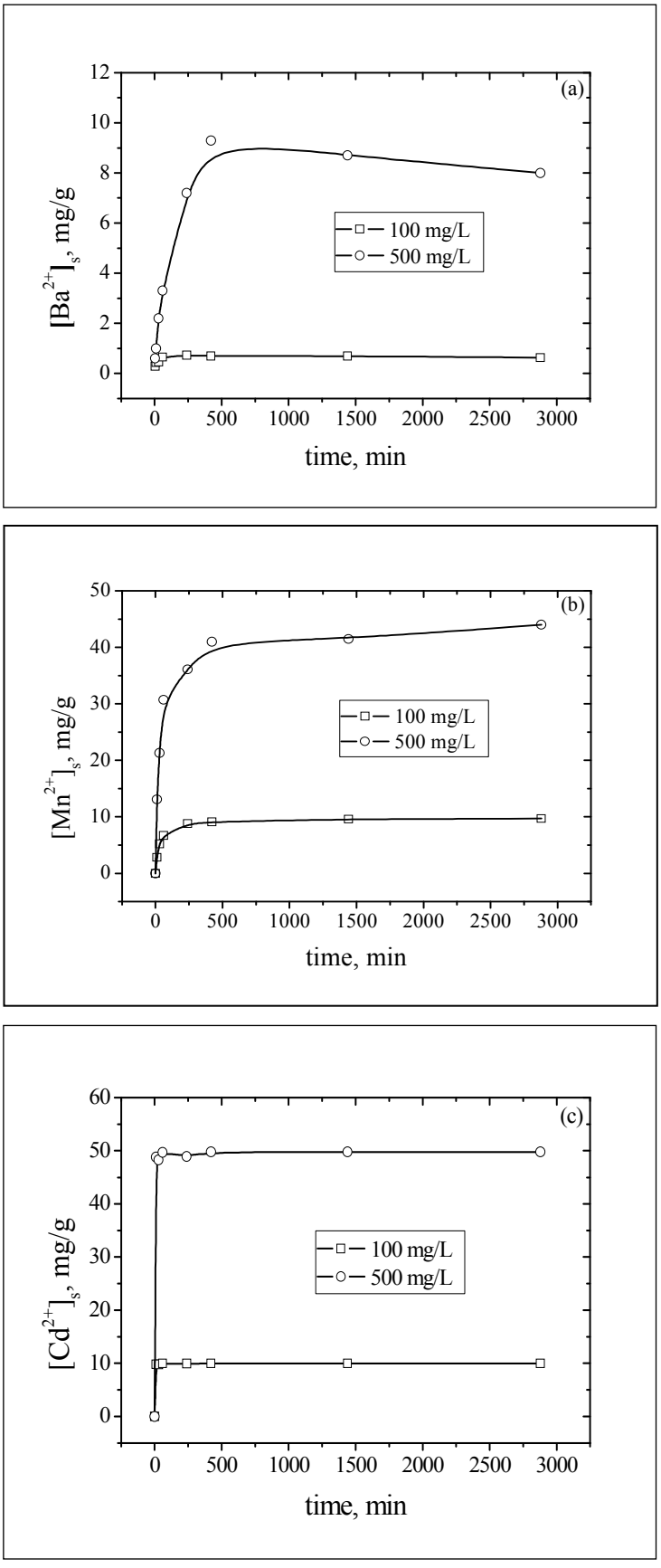

Figure 4.6. The variation of uptake of the ions (a) Ba^{2+}, (b) Mn^{2+}, and (c) Cd^{2+} by calcite mineral with respect to mixing time.

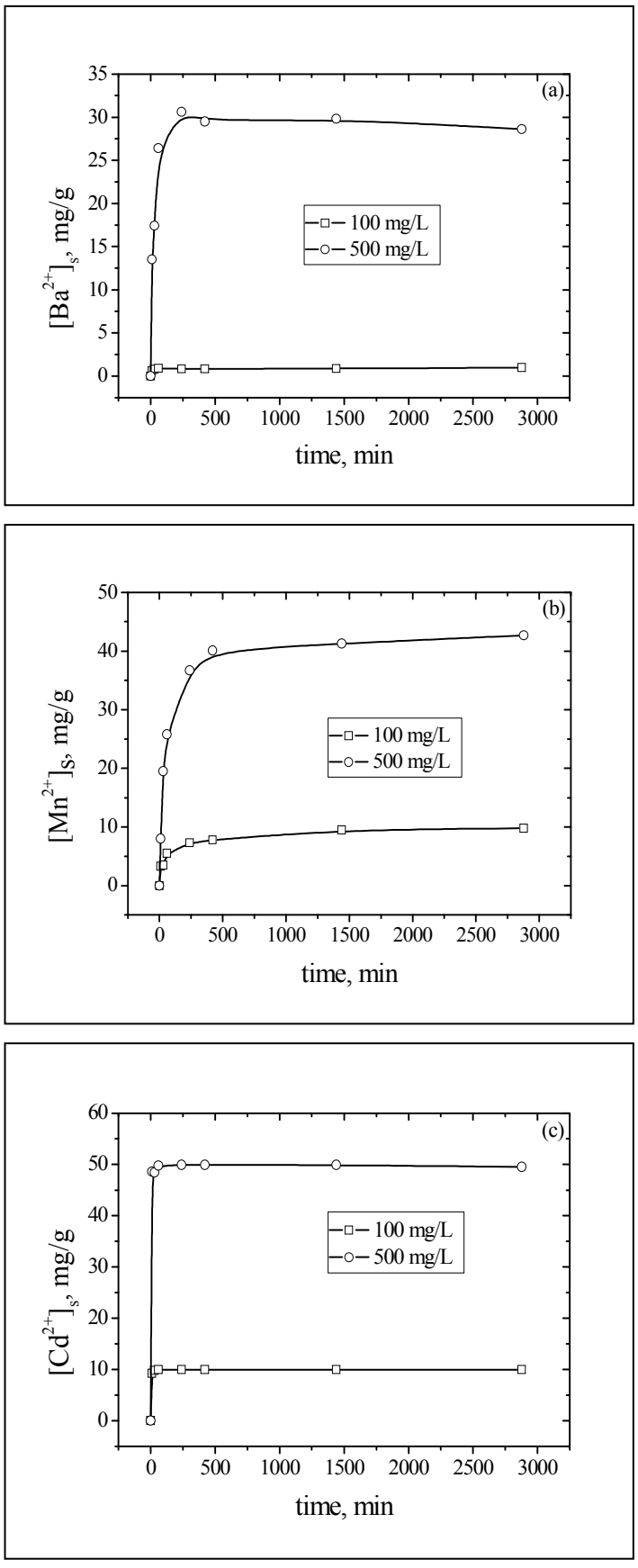

Figure 4.7. The variation of uptake of the ions (a) Ba^{2+}, (b) Mn^{2+}, and (c) Cd^{2+} by aragonite mineral with respect to mixing time.

Among these models, the best correlation with the experimental data was obtained by second order rate equation. This shows that the sorption of ions is very fast. The linear fits, k_2, and q_e are shown in Figure 4.8, and the model constants are given in Table 4.4, respectively. According to the values of the rate constant, k_2, the sorption rate is the fastest in the case of Cd^{2+}. The values of q_e indicate that both minerals demonstrated the highest affinity towards Cd^{2+} ions, the removal of which appears to be almost instantaneous as shown in the figure.

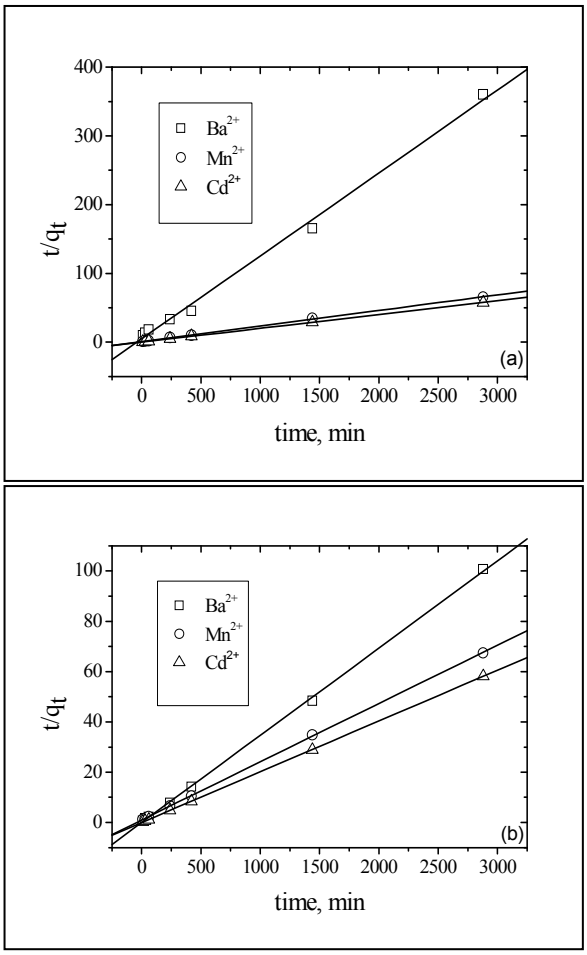

Figure 4.8. The linear fits obtained by use of second order rate equation: (a) adsorption of the ions on calcite, (b) adsorption of the ions on aragonite.

Table 4.4. k_2 and q_e values obtained by use of second order rate equation

Ion	Calcite			Aragonite		
	k_2 ($g.mg^{-1}.min^{-1}$)	q_e (mg/g)	R	k_2 ($g.mg^{-1}.min^{-1}$)	q_e (mg/g)	R
Ba^{2+}	3.1×10^{-3}	8.3	0.9979	4.4×10^{-3}	29.1	0.9998
Mn^{2+}	5.8×10^{-4}	44.3	0.9997	3.2×10^{-4}	44.5	0.9999
Cd^{2+}	1.8×10^{-2}	49.7	1.0000	6.1×10^{-3}	49.9	0.9999

4.2.2. Percentage Adsorption

In order to determine the percentage sorption of Ba^{2+}, Mn^{2+}, and Cd^{2+} at equilibrium condition, the sorption experiments are performed at initial concentrations of 10, 50, 100, and 500 mg/L under 25°C temperature and ambient pressure. The following equation was used in the calculations of percent sorption,

$$\text{Sorption}\% = \frac{[C]_0 - [C]_l}{[C]_0} \times 100\% \tag{4.4}$$

Here, C_0 is the initial and C_l is the equilibrium ion concentration. The values calculated from experimental data are given in Tables 4.5, 4.6, and 4.7. The tables provide also the equilibrium concentration of the ions in solution, $[C_l]$ (mg/L), and on the solid, $[C_s]$ (mg/g). These concentrations are interrelated to the initial concentration through the equation

$$[C]_S = \left([C]_0 - [C]_l\right) \times \frac{V}{M} \tag{4.5}$$

Here, V is the solution volume, M is the mass of the adsorbent.

Table 4.5. The equilibrium results corresponding to the uptake of Ba^{2+} ions by calcite and aragonite at various initial concentrations.

Mineral	$[C]_o$ (mg/L)	$[C]_l$ (mg/L)	$[C]_s$ (mg/g)	Sorption %
Calcite	10	3.7	0.63	63
	50	24	2.5	52
	100	67	3.3	33
	500	420	8.0	16
Aragonite	10	0.3	0.97	97
	50	8	4.2	84
	100	26	7.4	74
	500	241	28.6	52

Table 4.6. The equilibrium results corresponding to the uptake of Mn^{2+} ions by calcite and aragonite at various initial concentrations.

Mineral	$[C]_o$ (mg/L)	$[C]_l$ (mg/L)	$[C]_s$ (mg/g)	Sorption %
Calcite	10	0.4	0.96	96.4
	50	11.7	3.83	76.6
	100	29	7.10	71.0
	500	136	36.38	72.8
Aragonite	10	0.04	0.996	99.6
	50	3.1	4.69	93.8
	100	8.3	9.17	91.7
	500	28	47.2	94.4

Table 4.7. The equilibrium results corresponding to the uptake of Cd^{2+} ions by calcite and aragonite at various initial concentrations.

Mineral	$[C]_o$ (mg/L)	$[C]_l$ (mg/L)	$[C]_s$ (mg/g)	Sorption %
Calcite	10	~ 0	~1.0	> 99.9
	50	~ 0	~5.0	> 99.9
	100	0.2	9.98	> 99.9
	500	~ 0	~50.0	> 99.9
Aragonite	10	~ 0	~1.0	> 99.9
	50	~ 0	~5.0	> 99.9
	100	~ 0	~10.0	> 99.9
	500	0.2	49.98	99.7

The equilibrium values show that, almost all Cd^{2+} ions are sorbed by both calcite and aragonite minerals between 10mg/L and 500 mg/L concentration range. Mn^{2+} ions are also adsorbed in a great proportion by these two minerals. Both minerals demonstrated their smallest affinity towards Ba^{2+} ions. In the literature, there exist some resources asserting that Cd^{2+} ions are adsorbed by calcite more than Mn^{2+} ions (Curti 1999, Wang and Xu 2001). This is explained by the fact that the ionic radius of Cd^{2+} ions (0.95Å) is closer to that of Ca^{2+} ions (1.00Å) than is that of Mn^{2+} ions (0.83Å) the thing that makes Cd^{2+} ions suits more to the structural environment in calcium carbonate. This is valid, according to our results, for both minerals. Another important observation is that Ba^{2+} ions are much more adsorbed by aragonite minerals compared to calcite. No

experimental information is available in literature in regard to this. However, some theoretical models exist that are based on a thermodynamic basis predicting the preference of aragonite mineral towards Ba^{2+} uptake (Wang and Xu 2001). It is known that, the ionic radii of the second group ions such as Ba^{2+} and Sr^{2+} are greater than that of Ca^{2+} ion. Thus, it might be expected that they prefer the 9-foldcoordinated aragonite environment instead of the 6-foldcoordinated calcite cells. However, experimental evidence using structural technique collecting information on molecular level, such as EXAFS, is required to validate this conclusion.

On a thermodynamic basis, in recent years some approaches are applied in order to calculate the partition coefficients of adsorbed ions by $CaCO_3$ during solid solution ($Me_xCa_{(1-x)}CO_3$) formation process (Wang and Xu 2001, Sverjinsky and Molling 1992). In order to determine the partition coefficients, D_{Me}, of rhombohedral structures as calcite, Equation 4.6 can be used (Böttcher et al. 1997).

$$\log D_{Me,ideal} = (\Delta G^{o}_{f,\,CaCO3(s)} - \Delta G^{o}_{f,\,MeCO3(s)} - \Delta G^{o}_{f,\,Ca2+(aq)} + \Delta G^{o}_{f,Me2+\,(aq)}) / ((\ln (10))RT) \qquad (4.6)$$

In the equation, ΔG^{o}_{f} term represents the standard Gibbs free energies of adsorbed ions and rhombohedral carbonate structures, T is the Kelvin temperature and R is the ideal gas constant. Moreover, another equation was proposed by Y. Wang which included some properties of adsorbed ions.

$$-2.303\,RT \log K_d = a^*_{MHX}(\Delta G_{n,MH}{}^{Z+0} - \Delta G_{n,M}{}^{0}) + \beta^*_{MHX}(r_M{}^{Z+} - r_{n,MH}{}^{Z+}) - (\Delta G_{f,M}{}^{Z+0} - \Delta G^{0}_{f,MH}{}^{Z+}) \qquad (4.7)$$

In the equation, K_d, a^*, β^*, and r represents partition coefficient, model constants, and ionic radia, respectively. Based on this model, K_d values calculated for the adsorption of Ba^{2+}, Mn^{2+}, and Cd^{2+} ions by calcite and aragonite are given in Table 3.5. The obtained data generally obey to the order $Cd^{2+} > Mn^{2+} > Ba^{2+}$, in line with the results obtained by our experiments. However, the model prediction suggesting that Mn^{2+} ion is adsorbed by both calcite and aragonite approximately at same proportion does not correlate with the obtained experimental data.

Table 4.8. The partition coefficients calculated by the thermodynamic model of Wang's and Xu's (2001).

Metal Ion	Log K_d	
	Calcite	Aragonite
Ba^{2+}	-1.90	-0.86
Mn^{2+}	0.92	0.90
Cd^{2+}	2.52	3.09

4.3. Kinetics of Precipitate Formation of Metal Carbonates upon Interaction with Calcite and Aragonite

4.3.1. Rate of Precipitate Formation

The rate of metal-carbonate precipitate formation was investigated by using the initial concentrations 1000, 5000, and 10000 mg/L. In order to follow the kinetics of precipitate formation, the contact periods were changed from 30 minutes up to 3 weeks. The XRD diagrams of the samples obtained from the interaction of Ba^{2+}, Mn^{2+}, and Cd^{2+} ions at various concentrations with calcite and aragonite minerals at different time periods are shown in Figures 4.9-4.14. The most intense *hkl* reflections of metal carbonates are marked in these diagrams. The ICDD card numbers used in the identification of mineral carbonates are given in Table 4.9.

Table 4.9. ICDD card numbers of mineral carbonates relative to their crystal structure.

Mineral	ICDD Number
$CaCO_3$ (calcite)	81-2027
$CaCO_3$ (aragonite)	03-0405
$BaCO_3$ (witherite)	71-2394
$MnCO_3$ (rhodochrosite)	44-1472
$CdCO_3$ (otavite)	42-1342

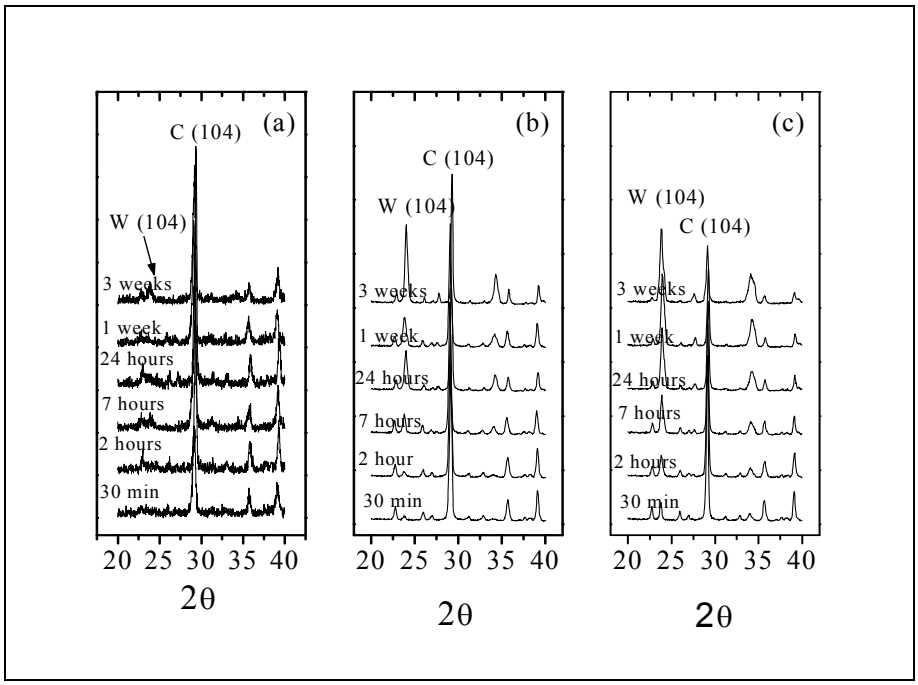

Figure 4.9. The change in *104* XRD signal of $BaCO_3$ (witherite) precipitate formed by the interaction of Ba^{2+} ions with calcite; (a) 1000 mg/L Ba^{2+}, (b) 5000 mg/L Ba^{2+}, (c) 10000 mg/L Ba^{2+} W: witherite, C: calcite.

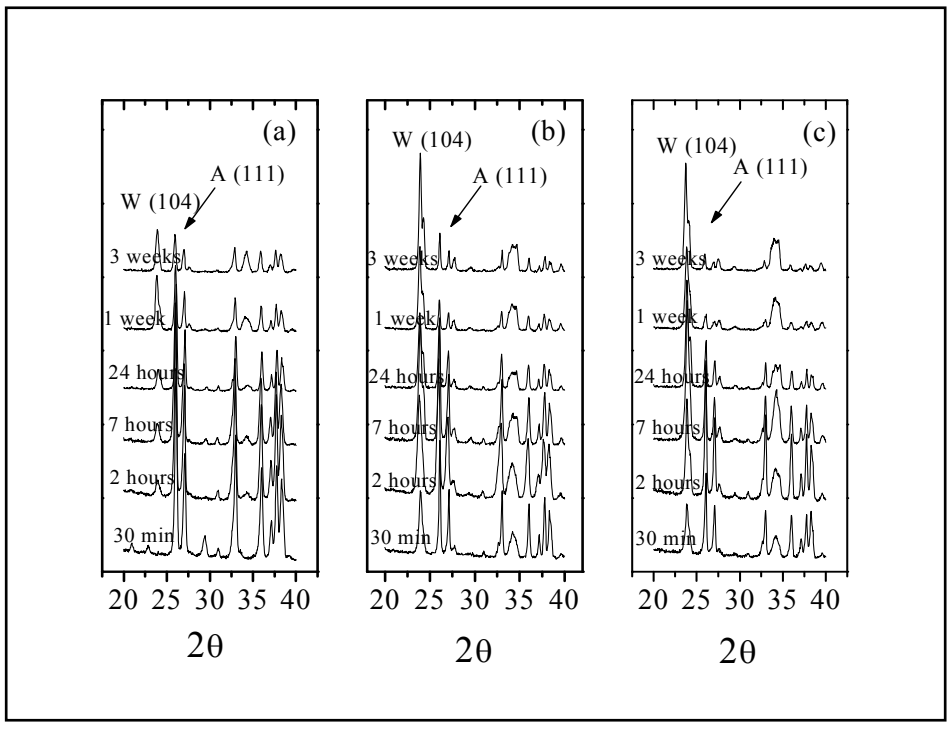

Figure 4.10. The change in *104* XRD signal of $BaCO_3$ (witherite) precipitate formed by the interaction of Ba^{2+} ions with aragonite; (a) 1000 mg/L Ba^{2+}, (b) 5000 mg/L Ba^{2+}, (c) 10000 mg/L Ba^{2+} W: witherite, A: aragonite

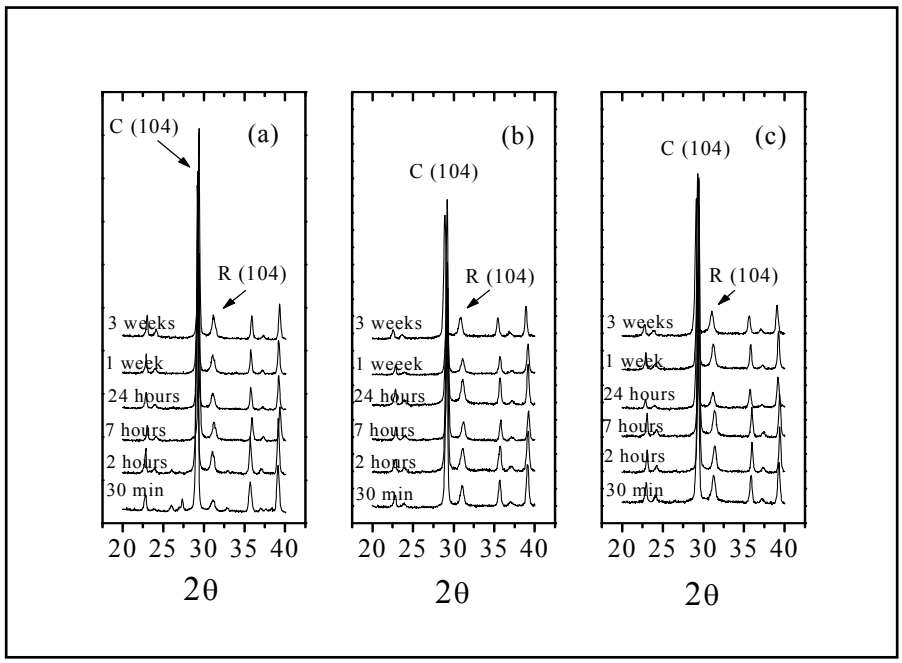

Figure 4.11. The change in *104* XRD signal of $MnCO_3$ (rhodochrosite) precipitate formed by the interaction of Mn^{2+} ions with calcite; (a) 1000 mg/L Mn^{2+}, (b) 5000 mg/L Mn^{2+}, (c) 10000 mg/L Mn^{2+} R: rhodochrosite, C: calcite

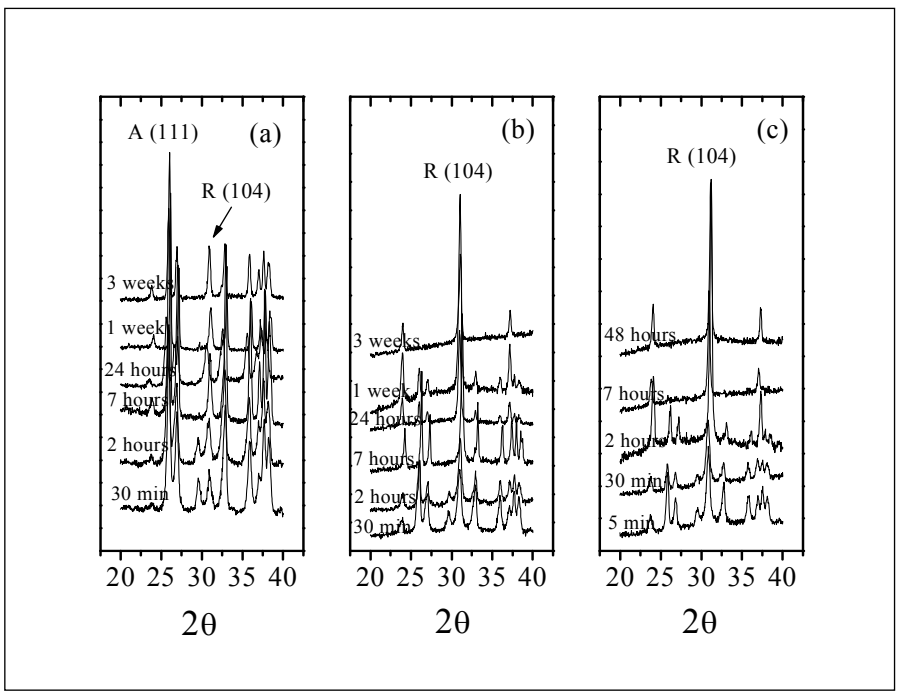

Figure 4.12. The change in *104* XRD signal of $MnCO_3$ (rhodochrosite) precipitate formed by the interaction of Mn^{2+} ions with aragonite; (a) 1000 mg/L Mn^{2+}, (b) 5000 mg/L Mn^{2+}, (c) 10000 mg/L Mn^{2+} R: rhodochrosite, A: aragonite

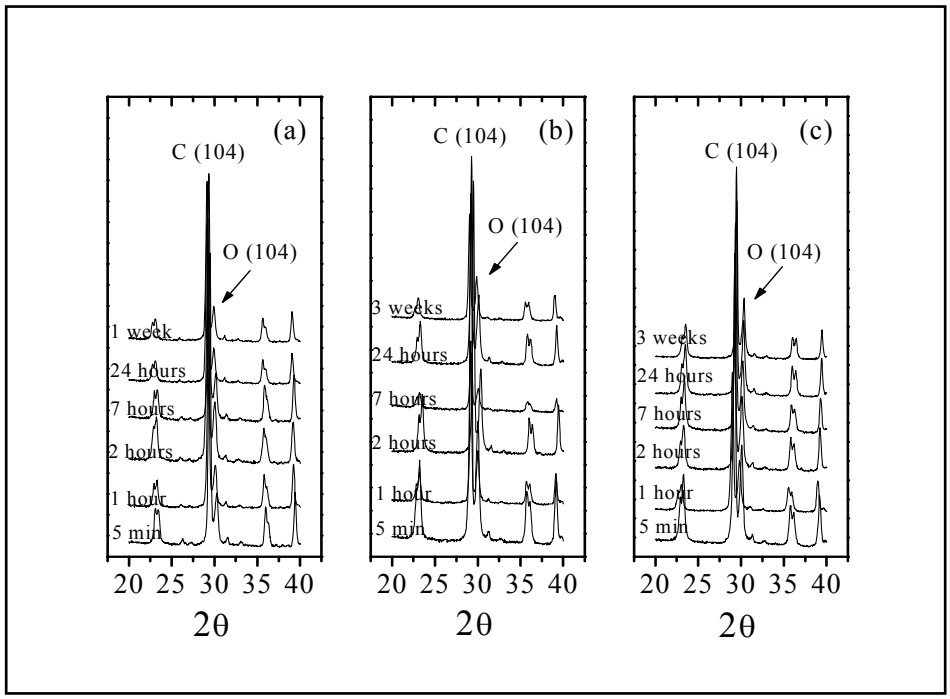

Figure 4.13. The change in *104* XRD signal of $CdCO_3$ (otavite) precipitate formed by the interaction of Cd^{2+} ions with calcite; (a) 1000 mg/L Cd^{2+}, (b) 5000 mg/L Cd^{2+}, (c) 10000 mg/L Cd^{2+} O: otavite, C: calcite.

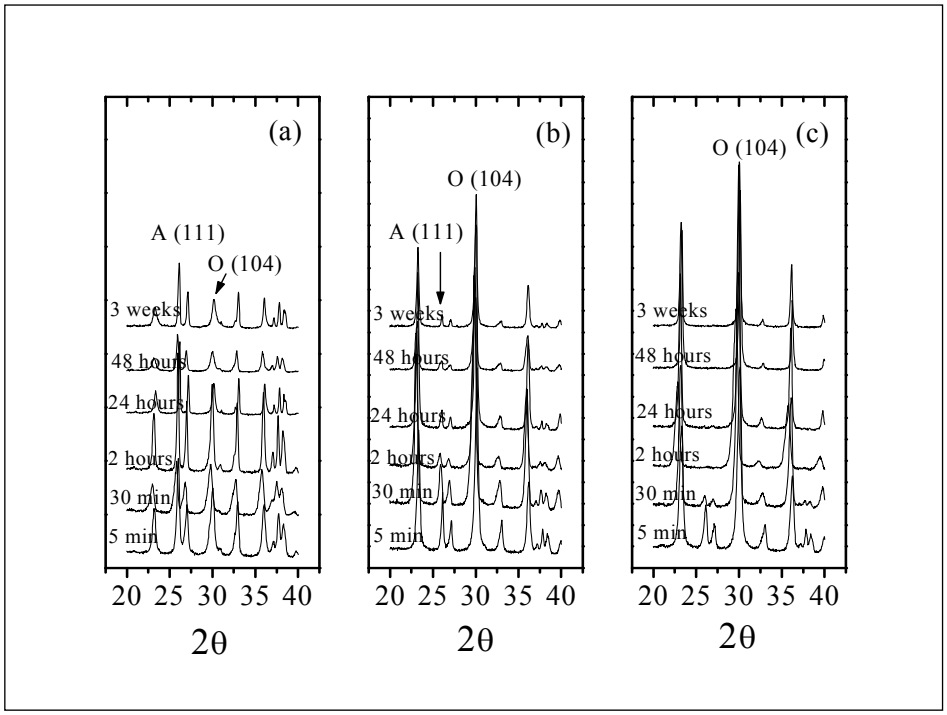

Figure 4.14. The change in *104* XRD signal of $CdCO_3$ (otavite) precipitate formed by the interaction of Cd^{2+} ions with aragonite; (a) 1000 mg/L Cd^{2+}, (b) 5000 mg/L Cd^{2+}, (c) 10000 mg/L Cd^{2+} O: otavite, A: aragonite.

As it is observed from diagrams, Ba^{2+}, Mn^{2+}, and Cd^{2+} ions form $BaCO_3$ (witherite), $MnCO_3$ (rhodochrosite), and $CdCO_3$ (otavite) minerals, respectively. The metal-carbonate peak signals increase in various proportions for different elements as the initial concentration is raised. The interaction of each of the ions with aragonite is seen to cause more metal-carbonate formation compared to the interaction with calcite. Also, the carbonate amounts formed upon the interaction of the ions with aragonite are more sensitive to the stirring time period in comparison to calcite.

As it is known, the precipitate formation of metal-carbonates in carbonate solutions is dependent on both carbonate and metal ion concentrations. Beyond saturation conditions, the reactions leading to $BaCO_3$, $MnCO_3$, or $CdCO_3$ formations in the solutions and the corresponding K_{sp} values (Skoog et al. 1997) are given below:

$$Ba^{2+} + CO_3^{2-} \Leftrightarrow BaCO_3(s) \qquad K_{sp}= 5.0 \times 10^{-9} \qquad (4.8)$$

$$Mn^{2+} + CO_3^{2-} \Leftrightarrow MnCO_3(s) \qquad K_{sp}= 5.0 \times 10^{-10} \qquad (4.9)$$

$$Cd^{2+} + CO_3^{2-} \Leftrightarrow CdCO_3(s) \qquad K_{sp}= 1.8 \times 10^{-14} \qquad (4.10)$$

It is expected that the existence of calcium carbonate in contact with the solutions will bring about surface precipitation. Based on the surface precipitation model (Zhu 2002), the reactions are given by the equations:

$$>CaCO_3^{o} + Me^{2+} + HCO_3^{-} \Leftrightarrow CaCO_3(s) + >MeCO_3^{o} + H^{+} \qquad (4.11)$$

$$>MeCO_3^{o} + Me^{2+} + HCO_3^{-} \Leftrightarrow MeCO_3(s) + >MeCO_3^{o} + H^{+} \qquad (4.12)$$

In the reactions, the symbol '>' indicates that carbonates are bound to the solid surface. According to the reactions, while some portion of metal carbonates are formed within the solution (bulk precipitation), another portion emerges by the interactions of metal ions with the carbonate ions on the solid surface (surface precipitation). In the bicarbonate-rich media, surface precipitation appears as a preliminary step for the bulk precipitation of metal carbonates. Within the pH values of the performed experiments, Tables 3.1-3.5, and the speciation of $CaCO_3$, the concentration of bicarbonate (HCO_3^-) ions is expected to be greater than that of CO_3^{2-} ions, and thus will play an important role in precipitate formation of the three metal carbonates.

4.3.2. XRD Quantitative Calculations

In order to determine the amounts of carbonates formed as a result of the interaction of ions with calcite and aragonite minerals, quantitative XRD was applied. For this purpose, empirical equations were developed for the quantification of binary carbonate mixtures. In these equations, it is possible to calculate the carbonate amount as a mass fraction by use of intensities of signals or peak areas obtained from XRD diagrams of the binary mixtures of $BaCO_3$, $MnCO_3$, or $CdCO_3$ minerals with calcite or aragonite.

Theoretically, the intensities of the x-rays reflected from any component is directly proportional with the amount of substances in that component and inversely proportional with the mass absorption coefficient of the mixture (Ouhadi and Yong 2003). In the first step of the quantitative XRD studies, XRD diagrams were recorded for synthetic $MeCO_3$-calcite and $MeCO_3$-aragonite mixtures formed from pure phases of calcite, aragonite, and $MeCO_3$ ($MeCO_3$ = $BaCO_3$, $MnCO_3$, or $CdCO_3$) minerals. These mixtures were prepared by mixing metal carbonates with pure calcite or aragonite containing 0.10, 0.20, 0.30, 0.40, 0.50, 0.60, 0.70, 0.80, and 0.90 metal carbonate as mass fraction in a mixture. All these processes were repeated three times for each carbonate mixtures. The peak areas of *hkl* lines of metal carbonates, *104* reflections of calcite, witherite, rhodochrosite, and otavite *111* reflection of aragonite obtained from XRD diagrams were obtained by use of Origin 5.0 program. Using the peak areas, the ratios of $MeCO_3$/calcite and $MeCO_3$/aragonite were calculated and the calibration curves were developed by drawing these ratios versus mass fractions. Finally, the curves were fitted to mathematical equations using Microsoft Excel. It was observed that the standard error fit of curves do not exceed 5%. The experimental data and corresponding fits are provided in Figure 4.15 and 4.16 for metal carbonate precipitation on calcite and aragonite, respectively.

In carrying out the quantification analysis, it is assumed that the mass absorption coefficients of these synthetic binary mixtures are the same as those of the samples formed as a result of precipitation of $MeCO_3$ on calcite or aragonite surfaces. In addition to this, the peak areas of the most intense reflections of metal carbonates were used instead of using peak areas of all XRD reflection lines.

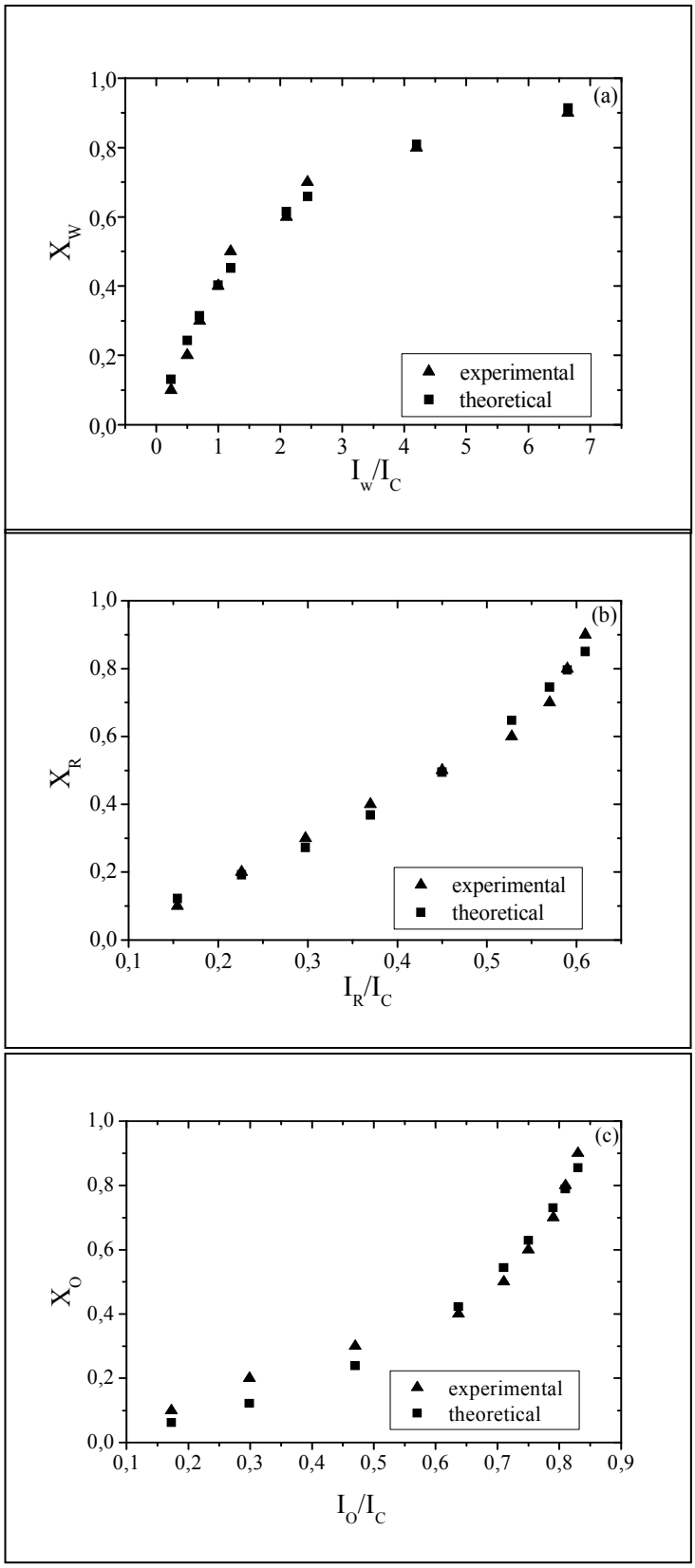

Figure 4.15. Variation of the mass fractions of $MeCO_3$ in their mixtures with calcite as a function of the intensity ratio of the $MeCO_3$/calcite; $MeCO_3$= (a) $BaCO_3$, (b) $MnCO_3$, (c) $CdCO_3$.

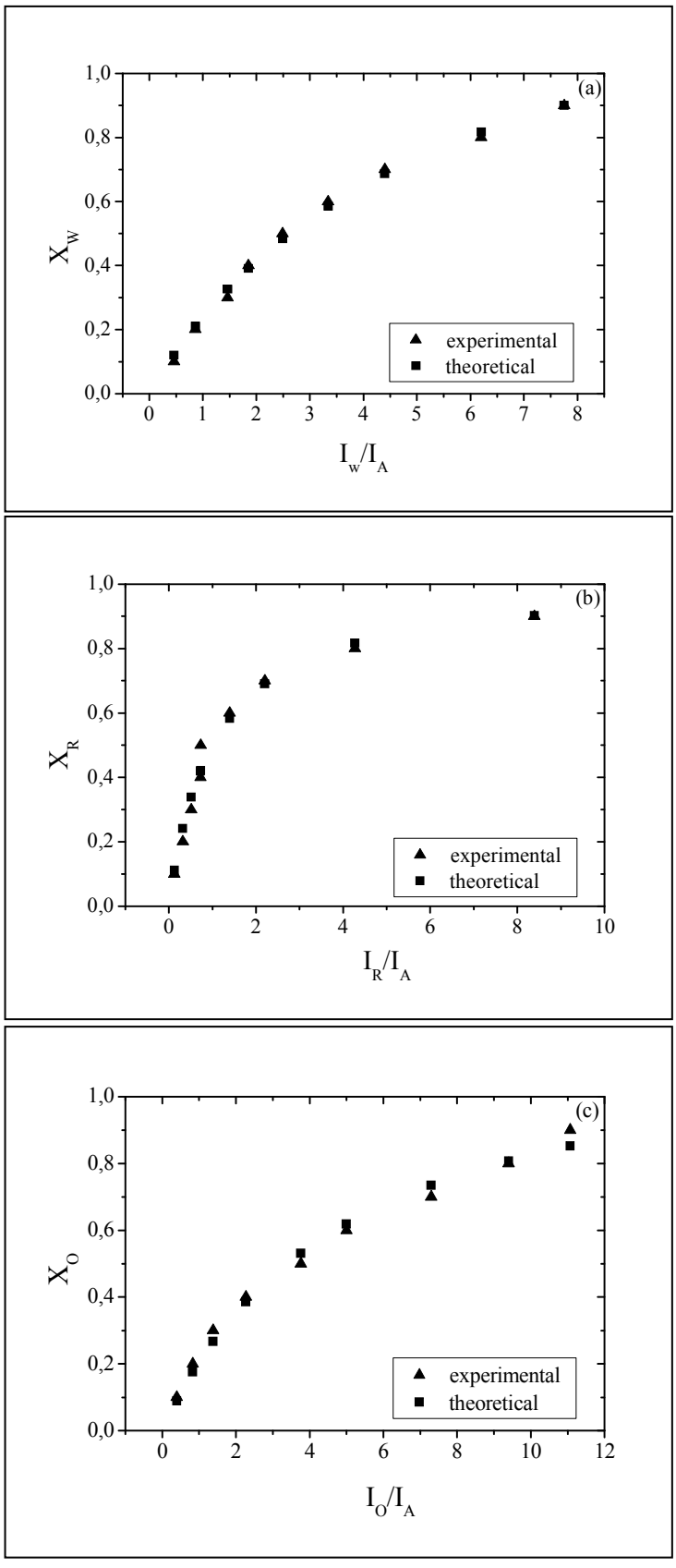

Figure 4.16. Variation of the mass fractions of $MeCO_3$ in their mixtures with aragonite as a function of the intensity ratio of the $MeCO_3$/aragonite; $MeCO_3$= (a) $BaCO_3$, (b) $MnCO_3$, (c) $CdCO_3$.

The equations obtained from calibration curves are given in Table 4.10. The range of peak area ratios used in the development of the equations ($I_{MeCO3}/I_{calcite}$ or $I_{MeCO3}/I_{Aragonite}$) is also included in Table 4.10 together with the standard error fits. In the equations, X_W, X_R, and X_O represent the mass fractions of $BaCO_3$ (witherite), $MnCO_3$ (rhodochrosite), and $CdCO_3$ (otavite), respectively. I_W, I_R, I_O, and I_C represent the peak areas of *104* reflections of $BaCO_3$, $MnCO_3$, $CdCO_3$, and calcite; while, I_A indicates peak area of *111* reflection of aragonite.

Table 4.10. The equations of binary metal carbonates developed for quantitative XRD analysis.

Carbonate Mixture	**Equation**	**Range of Peak Ratios Used (I_{MeCO3}/I_{CaCO3})**	**Standard Error Fit of Curves**
$BaCO_3$-calcite	$X_W = \frac{0.61(I_W / I_C)}{1 + 0.52(I_W / I_C)}$	0.0 - 6.64	3.3 %
$MnCO_3$-calcite	$X_R = \frac{0.69(I_R / I_C)}{1 - 0.83(I_R / I_C)}$	0.0 - 0.61	3.6 %
$CdCO_3$-calcite	$X_O = \frac{0.31(I_O / I_C)}{1 - 0.85(I_O / I_C)}$	0.0 - 0.83	5.0 %
$BaCO_3$-aragonite	$X_W = \frac{0.28(I_W / I_A)}{1 + 0.19(I_W / I_A)}$	0.0 - 7.75	1.8 %
$MnCO_3$-aragonite	$X_R = \frac{0.99(I_R / I_A)}{1 + 0.97(I_R / I_A)}$	0.0 - 8.39	2.9 %
$CdCO_3$-aragonite	$X_O = \frac{0.25(I_O / I_A)}{1 + 0.20(I_O / I_A)}$	0.0 - 11.07	2.4 %

The variation of the mass fraction of $MeCO_3$ (calculated using the above equations) with different times and initial concentrations are shown in Figures 4.17, 4.18, and 4.19. Since XRD signals originate from the upper part of the surface (several microns), the calculated mass fractions are expected to be different from the fractions within the bulk.

As can be seen from the figures, the amount of $MeCO_3$ precipitates formed on aragonite mineral are larger than those formed on calcite mineral at all concentrations.

The general trend indicates that, the precipitate formation kinetics increases at the initial stages; then decreases, and finally approaches equilibrium. Depending on the concentration and the type of the metal, days or weeks might be required for precipitate formation kinetics to approach equilibrium.

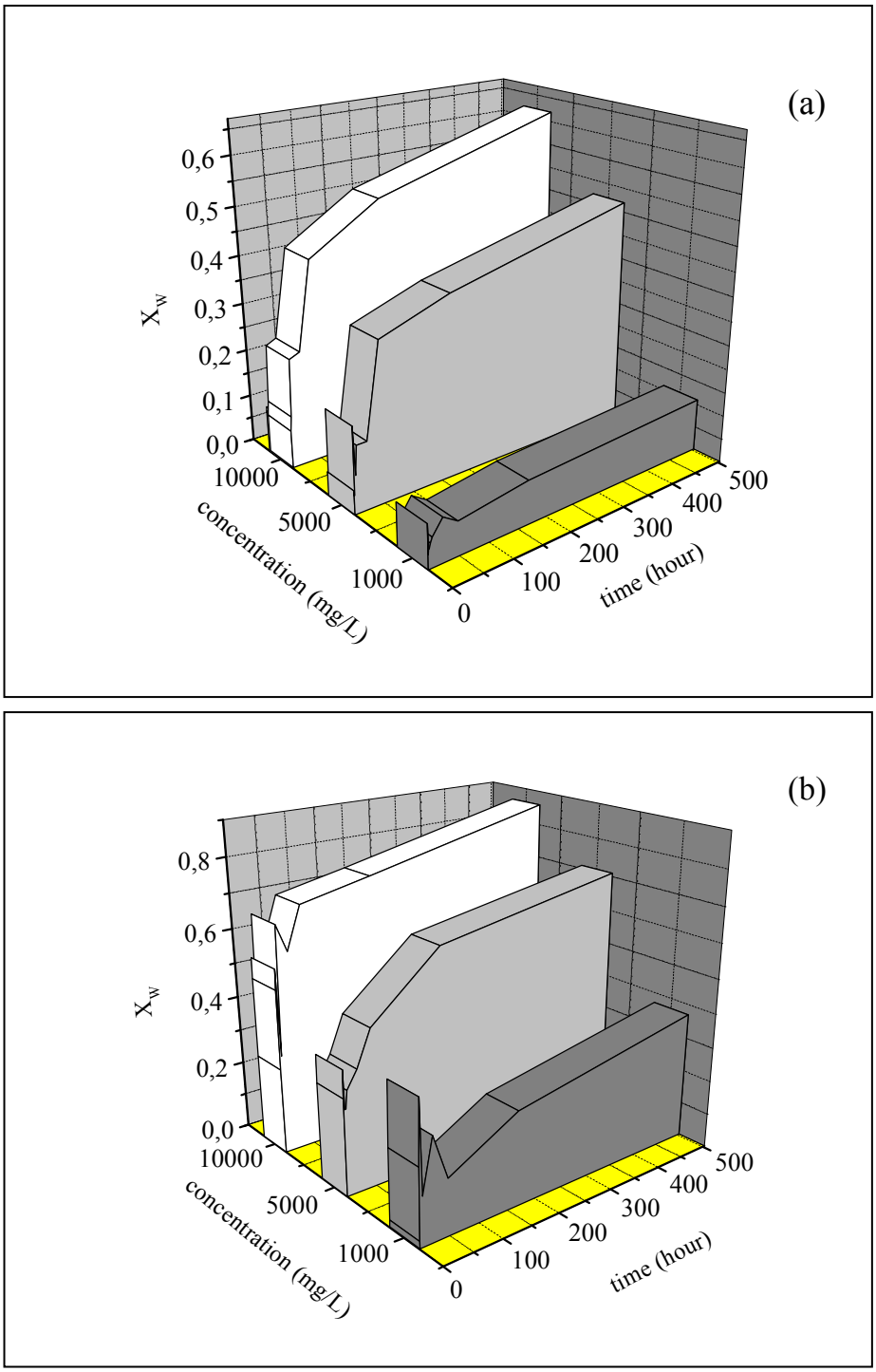

Figure 4.17. The change of mass fractions of precipitated $BaCO_3$ as a function of time and initial concentration; (a) on calcite surface, (b) on aragonite surface.

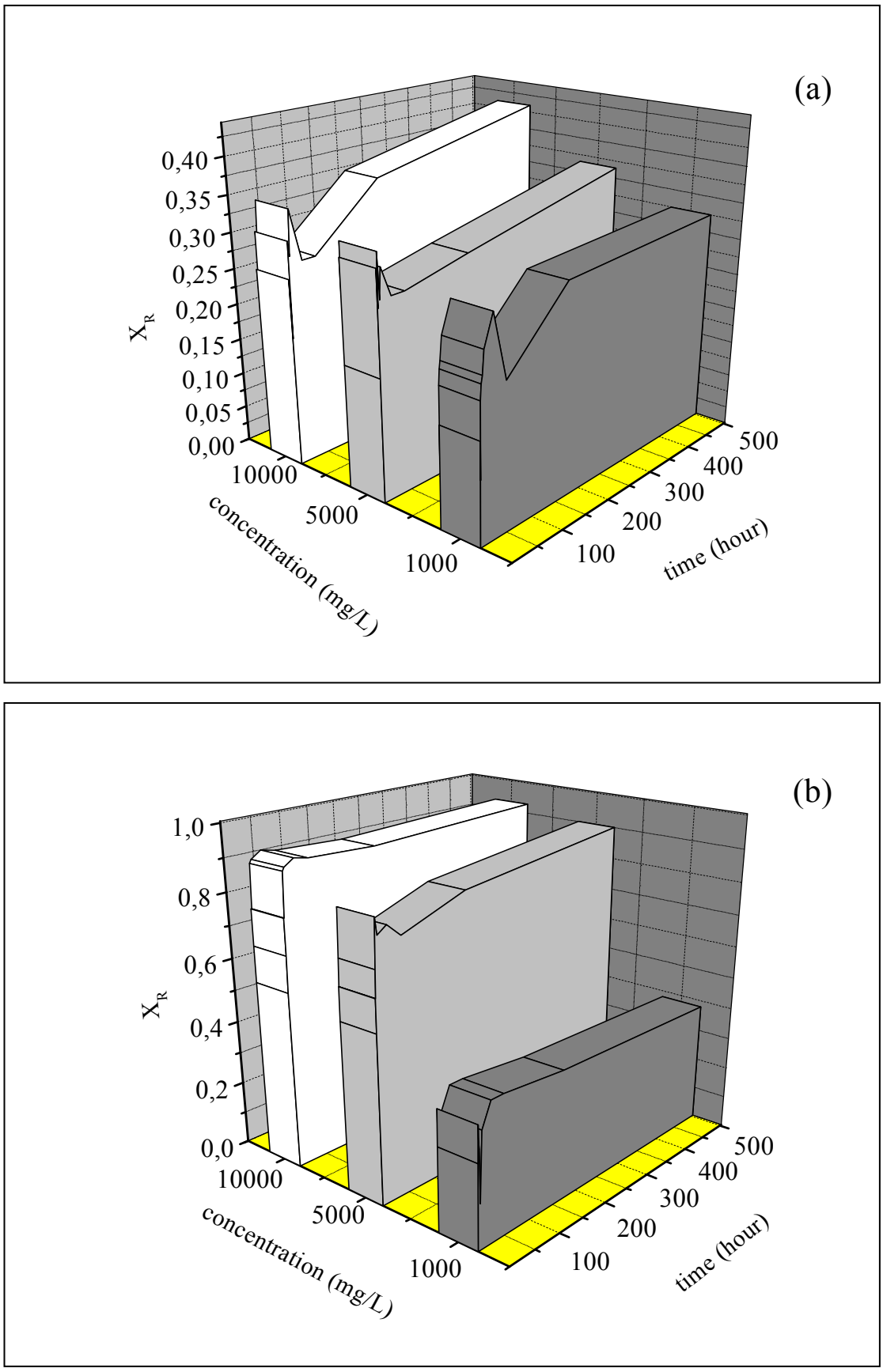

Figure 4.18. The change of mass fractions of precipitated $MnCO_3$ as a function of time and initial concentration; (a) on calcite surface, (b) on aragonite surface.

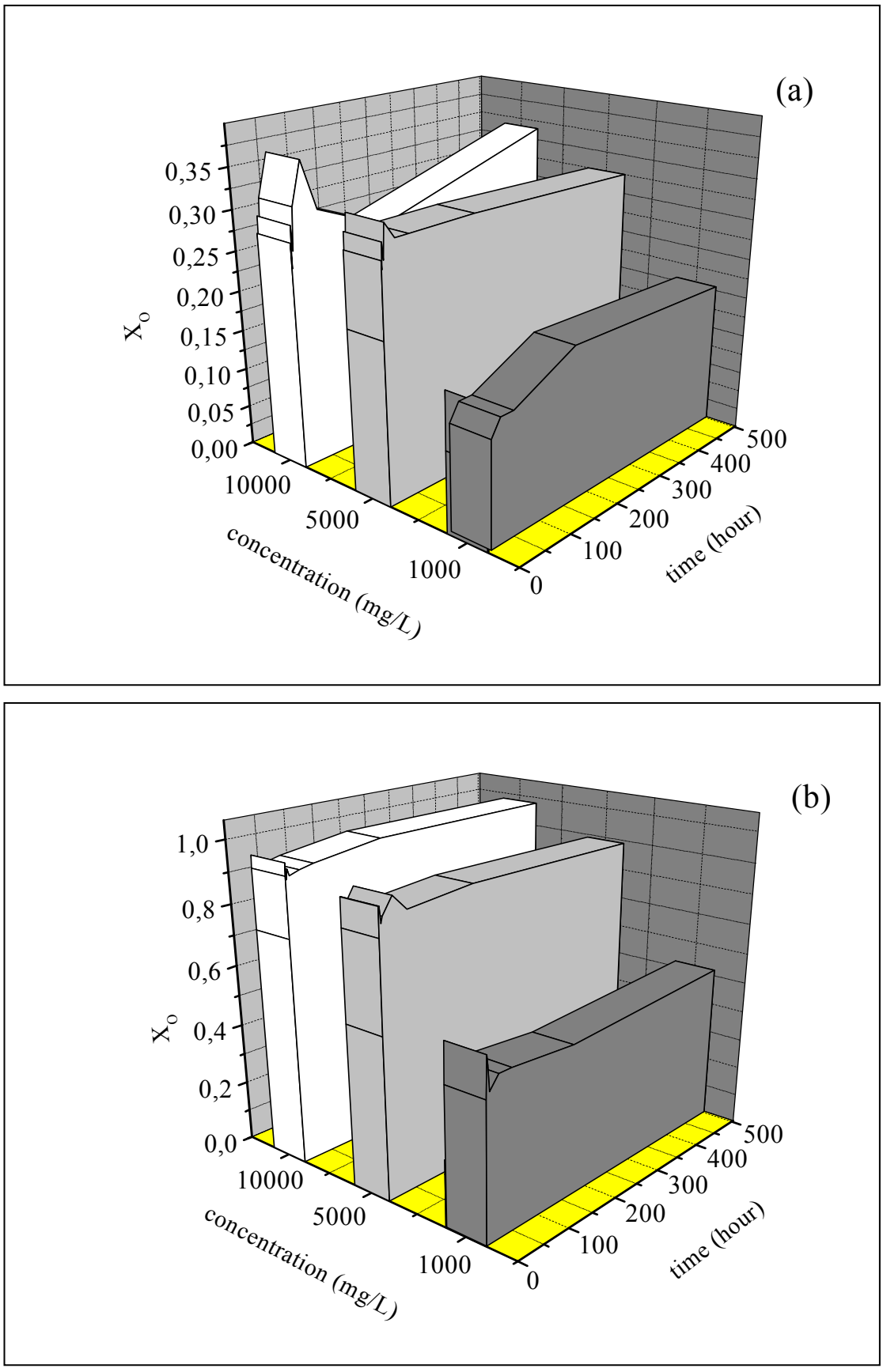

Figure 4.19. The change of mass fractions of precipitated $CdCO_3$ as a function of time and initial concentration; (a) on calcite surface, (b) on aragonite surface.

As the figures show, among these three carbonates, $BaCO_3$ is demonstrating the slowest kinetics. It is seen that, the increase of initial ion concentration affects precipitated $BaCO_3$ amount more than other metal carbonates. This is particularly observed when the concentration is increased from 5000 mg/L to 10000 mg/L. The mass fraction of $BaCO_3$ on aragonite surface at 10000 mg/L initial ion concentration is about 0.8 whereas that on calcite surface is approximately 0.6. While a limited amount of Ba^{2+} ions are adsorbed by calcite mineral as was previously mentioned, larger amount of Ba^{2+} are fixed during the precipitation process. This shows that in addition to tightly fixing the ion in the solid matrix, the precipitation mechanism involves an enhanced uptake of that ion. On the other hand, $MnCO_3$ and $CdCO_3$ show similar behaviors with respect to precipitate kinetics and precipitated amounts. The mass fractions of $MnCO_3$ and $CdCO_3$ formed on calcite surface at 10000 mg/L ion concentration are approximately 0.30 and 0.35 whereas this fraction is 0.9 on aragonite surface which means that aragonite surface is almost covered by $MnCO_3$ and $CdCO_3$.

4.3.3. EDS Mapping

EDS mapping was used to reveal the distribution of Ba, Mn, and Cd on the surface of calcite and aragonite, following the precipitation of the carbonates of these elements. The distribution of Ba^{2+} in the carbonate surface in comparison to that of Ca^{2+} was recorded over areas of approximate dimensions of 100μm×100μm. The elemental maps were recorded for carbonates contacted with Ba^{2+}, Mn^{2+}, and Cd^{2+} at the initial concentration of 10000 mg/L for a period of 3 weeks. The EDS maps are shown in Figure 4.20. In the $BaCO_3$-calcite sample, the Ca-rich cores appear to include large spheroidal grains that are surrounded by more finely distributed Ba-containing phase (presumably $BaCO_3$). In $BaCO_3$-aragonite case, more intense Ba maps were obtained. Compared with $BaCO_3$-calcite samples, the exterior rims of the carbonate grains are less distinguishable and appear more uniformly distributed. However, closer inspection reveals the presence of Ba- and Ca-rich regions corresponding to the two distinct carbonate phases.

Similar results were obtained for the distributions of Mn and Cd on calcite and aragonite surfaces. Typical maps of Mn, Cd in comparison to Ca distributions are demonstrated in Figure 4.21 and 4.22, respectively.

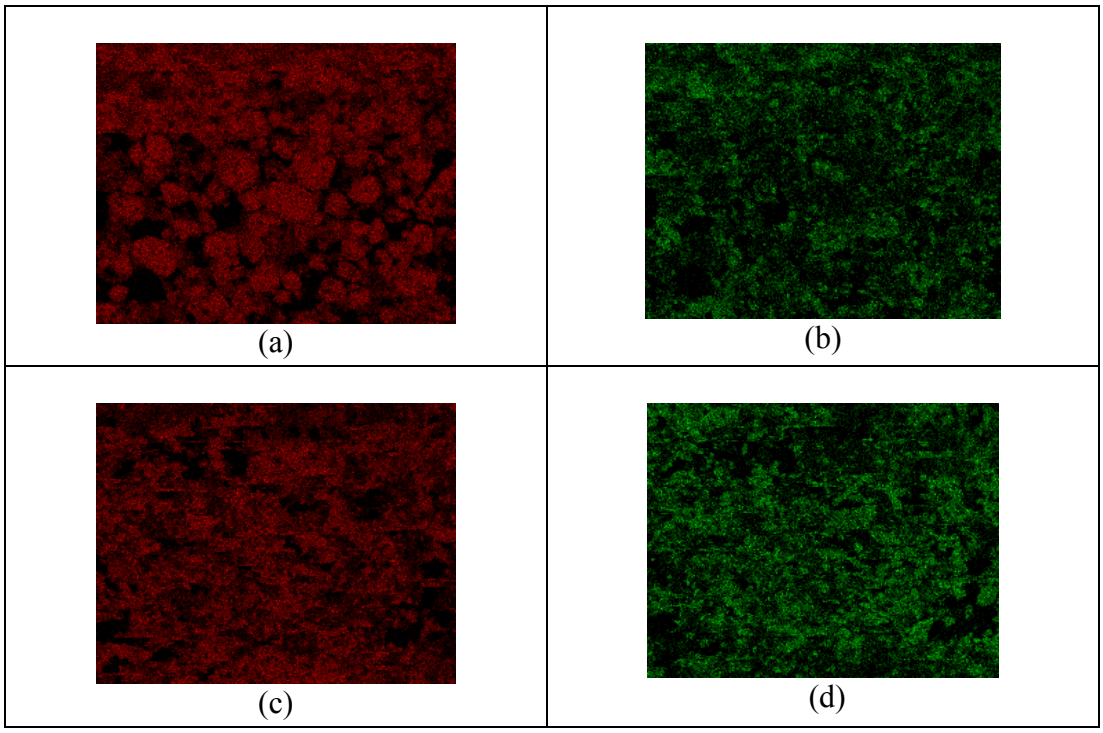

Figure 4.20. X-ray maps showing the distributions of (a) Ca on $BaCO_3$-calcite surface, (b) Ba on $BaCO_3$-calcite surface, (c) Ca on $BaCO_3$-aragonite surface, (d) Ba on $BaCO_3$-aragonite surface.

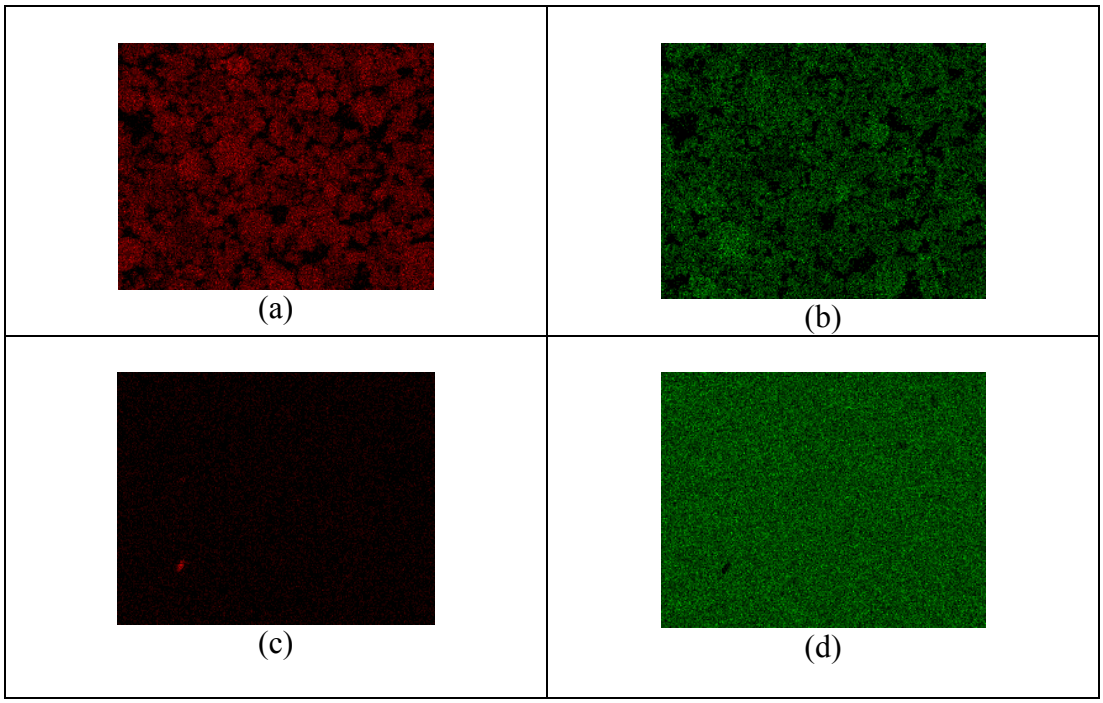

Figure 4.21. X-ray maps showing the distributions of (a) Ca on $MnCO_3$-calcite surface, (b) Mn on $MnCO_3$-calcite surface, (c) Ca on $MnCO_3$-aragonite surface, (d) Mn on $MnCO_3$-aragonite surface.

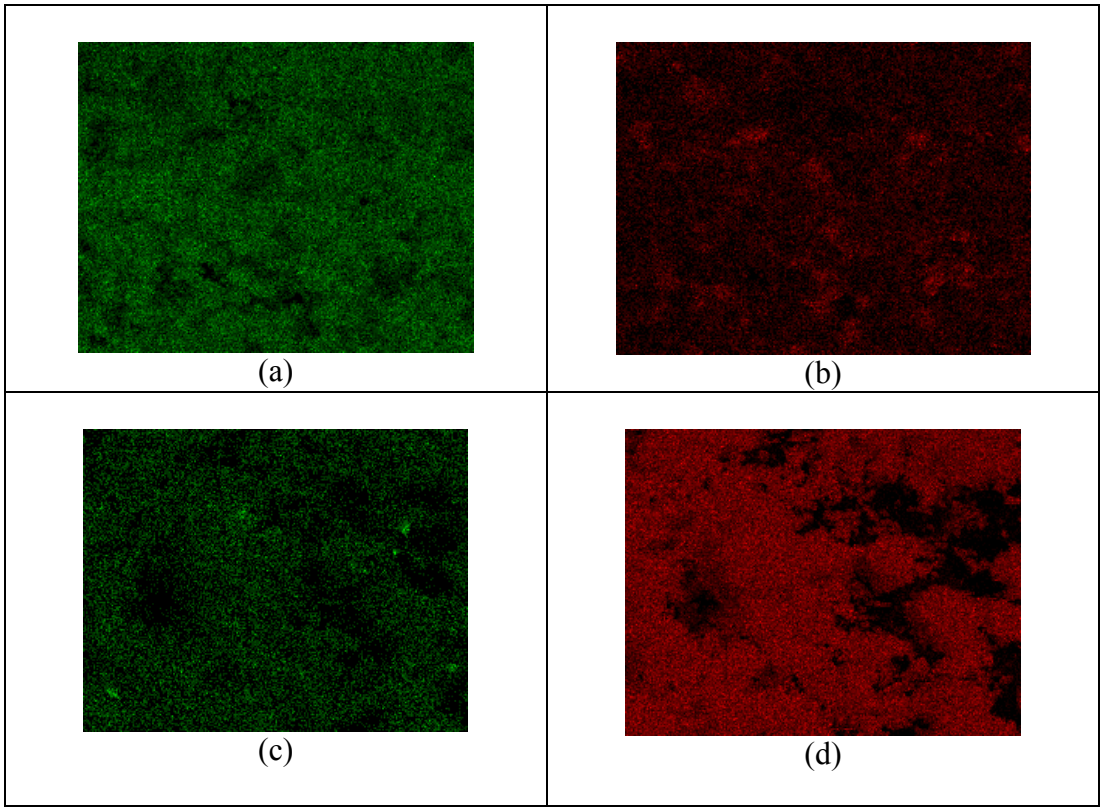

Figure 4.22. X-ray maps showing the distributions of (a) Ca on $CdCO_3$-calcite surface, (b) Cd on $CdCO_3$-calcite surface, (c) Ca on $CdCO_3$-aragonite surface, (d) Cd on $CdCO_3$-aragonite surface.

As it is observed from the figures, Mn and Cd signals cover almost completely aragonite in comparison to weak Ca signals, which is inline with the XRD quantitative results discussed in the previous section. On the other hand, Mn and Cd signals on $MeCO_3$-calcite surface are seen to be weaker than that of $MeCO_3$-aragonite surface, the thing accompanied with stronger Ca signals compared to aragonite case.

4.3.4. Effect of pH Change on Precipitate Formation

In order to determine the effect of pH on precipitate formation, the pH of the medium was adjusted to 10.0. The precipitates of the samples prepared in 1000, 5000, and 10000 mg/L initial concentration and 24 hours stirring time are investigated. XRD diagrams of $MeCO_3$-calcite and $MeCO_3$-aragonite ($MeCO_3$= $BaCO_3$, $MnCO_3$, or $CdCO_3$) are shown in Figure 4.23 and 4.24, respectively. Theoretically, it is expected that the increase of pH will cause an increase in the amount of carbonate ions, CO_3^{2-}, in

the medium and consequently enhance precipitation. The aim of the experiments was to reveal the comparative response of calcite and aragonite to the increase in pH of the medium. The amount of precipitated metal carbonates was increased by various proportions upon increasing the pH to 10.0. Generally, this increment is much more distinct in aragonite case than calcite case for the three ions; Ba^{2+}, Mn^{2+}, and Cd^{2+}. In the case of calcite, the decrease in calcite signals which points to the extent of dissolution and the consequent formation of $MeCO_3$ on calcite surface, is most pronounced in the case of contact with Cd^{2+} ions, and is the least upon contact with Ba^{2+} ions.

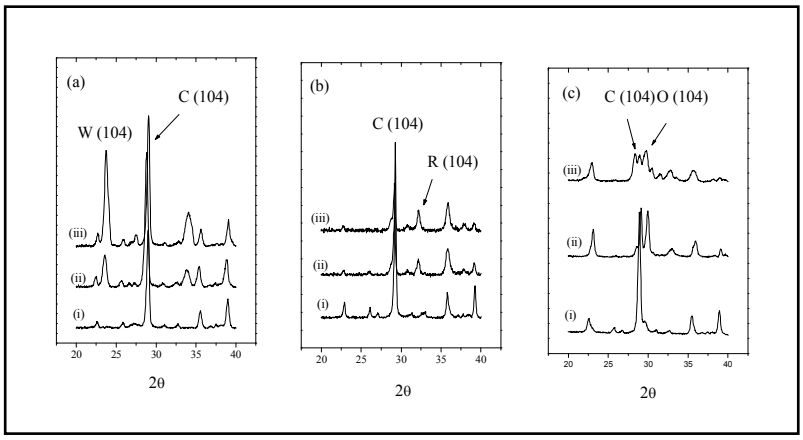

Figure 4.23. XRD diagrams of the precipitates formed on calcite surface after the pH of medium was adjusted to 10.0 (a) $BaCO_3$, (b) $MnCO_3$, and (c) $CdCO_3$. The initial ion concentrations are (i) 1000 mg/L, (ii) 5000 mg/L, and (iii) 10000 mg/L W: witherite, R: rhodochrosite, O: otavite, and C: calcite.

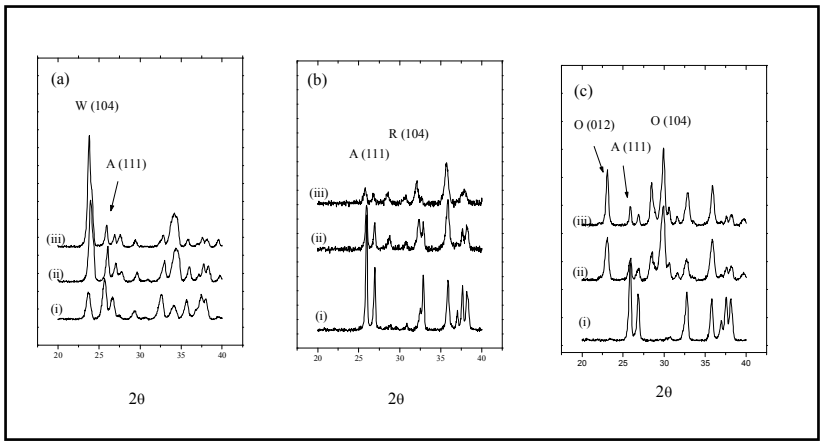

Figure 4.24. XRD diagrams of the precipitates formed on aragonite surface after the pH of medium was adjusted to 10.0 (a) $BaCO_3$, (b) $MnCO_3$, and (c) $CdCO_3$. The initial ion concentrations are (i) 1000 mg/L, (ii) 5000 mg/L, and (iii) 10000 mg/L. W: witherite, R: rhodochrosite, O: otavite, and A: aragonite.

4.3.5. Effect of Temperature Change on Precipitate Formation

In order to determine the effect of temperature on precipitate formation, the temperature of the medium is adjusted to 50°C in comparison to the earlier experiments performed at room temperature. The precipitates of the samples prepared at the initial concentration of 1000, 5000, and 10000 mg/L and stirring time 24 hours are investigated. The obtained XRD diagrams of $MeCO_3$-calcite and $MeCO_3$-aragonite are shown in Figure 4.25 and 4.26, respectively. The results indicated an apparent increase in the intensities of precipitated metal carbonates. Our earlier experiments on the effect of temperature on adsorption of these metal ions have also indicated an increase in the fixed amounts of ions as a result of temperature increase. Although the same seems to be valid at the stage of precipitation, according to our experiments, further elaboration of the topic is required.

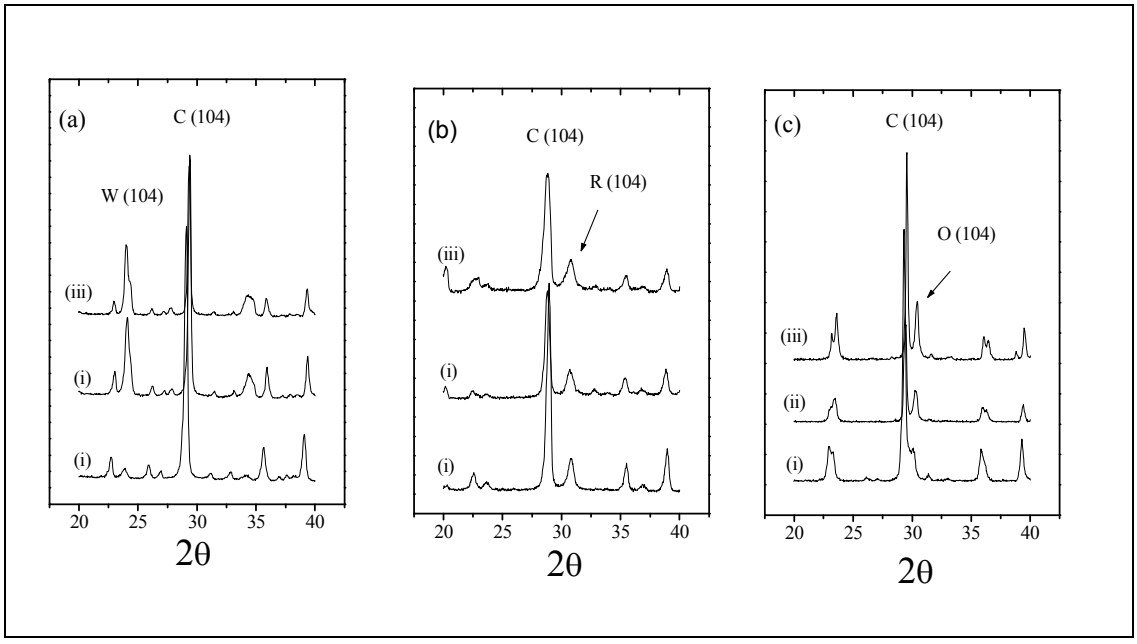

Figure 4.25. XRD diagrams of the precipitates formed on calcite surface after the temperature of medium was adjusted to 50°C (a) $BaCO_3$, (b) $MnCO_3$, and (c) $CdCO_3$. The initial ion concentrations are (i) 1000 mg/L, (ii) 5000 mg/L, and (iii) 10000 mg/L W: witherite, R: rhodochrosite, O: otavite, and C: calcite.

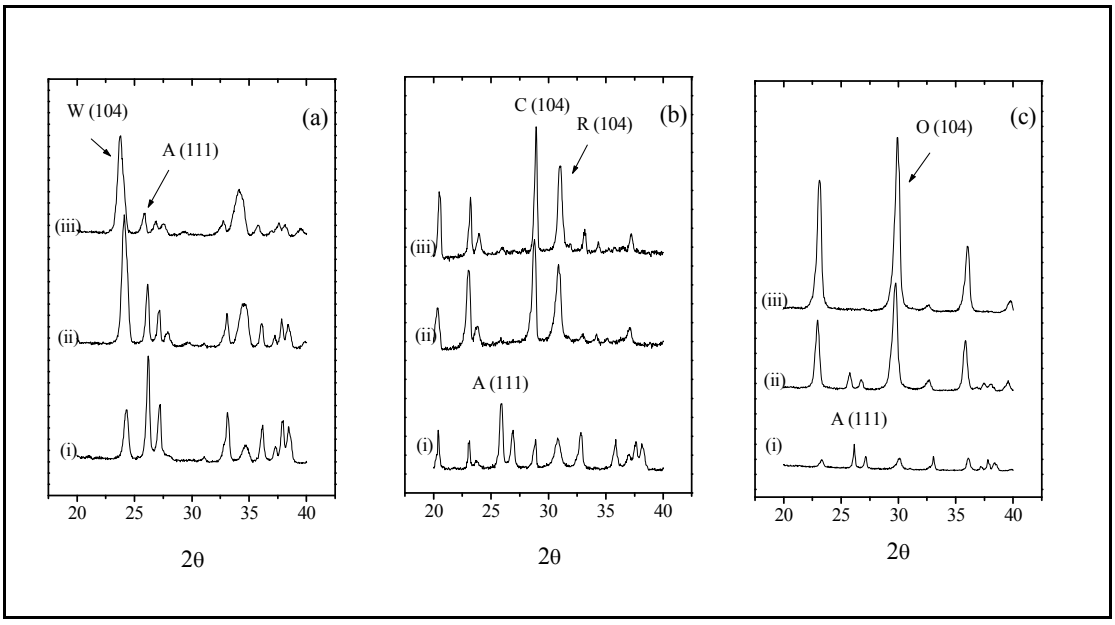

Figure 4.26. XRD diagrams of the precipitates formed on aragonite surface after the temperature of medium was adjusted to 50°C (a) $BaCO_3$, (b) $MnCO_3$, and (c) $CdCO_3$. The initial ion concentrations are (i) 1000 mg/L, (ii) 5000 mg/L, and (iii) 10000 mg/L W: witherite, R: rhodochrosite, O: otavite, and A: aragonite.

4.4. The Morphological Aspects and FTIR Spectra of Precipitated Metal Carbonates

4.4.1. SEM Images

Scanning Electron Microscope (SEM) was used to reveal the morphologies of the minerals. Typical SEM images of $BaCO_3$, $MnCO_3$, and $CdCO_3$ minerals formed on calcite and aragonite surfaces are given in Figure 4.27, 4.28 and 4.29, respectively.

As it is seen from Figure 4.27, $BaCO_3$ minerals precipitated on both minerals appeared to predominantly possess olivary-like morphology with an average particle size of 1-2 μm. Based on SEM images of $MnCO_3$, the crystal size of the mineral is about 200 nm, and it owns layered rhombohedral morphology (Figure 4.28). The morphology of $CdCO_3$ mineral is less distinct compared to other carbonates. In this carbonate structure, there are aggregates with 1-2 μm size in a conic shape and each aggregate consists of layers whose edge length is approximately 100 nm (Figure 4.29).

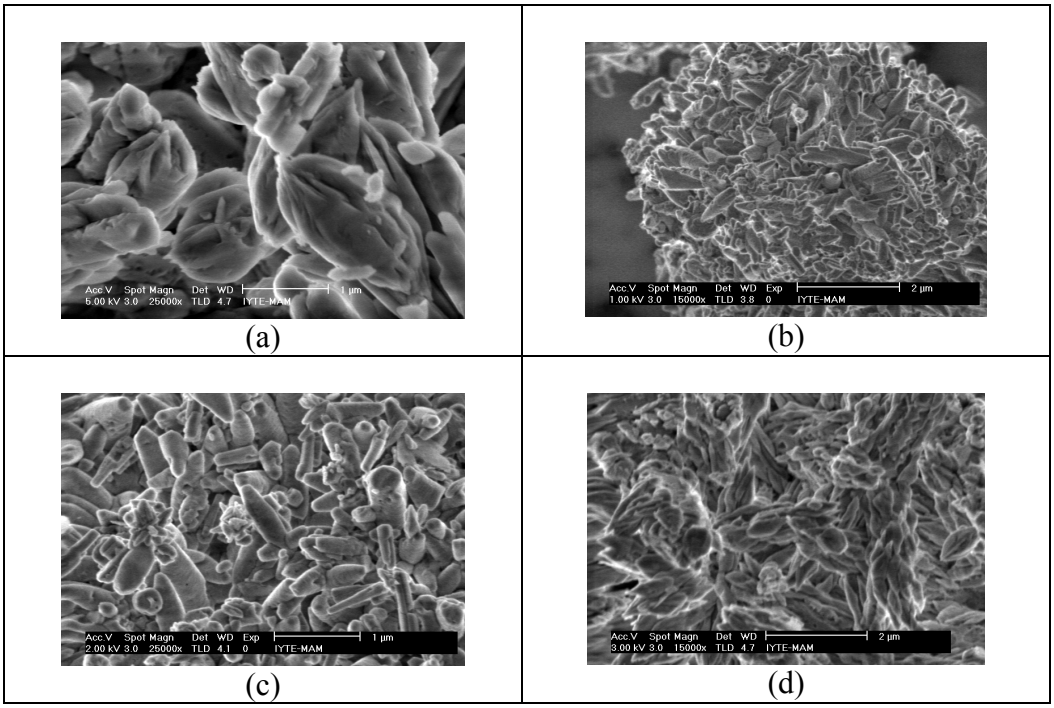

Figure 4.27. SEM images of $BaCO_3$ precipitated on (a, b) calcite surface, (c, d) aragonite surface.

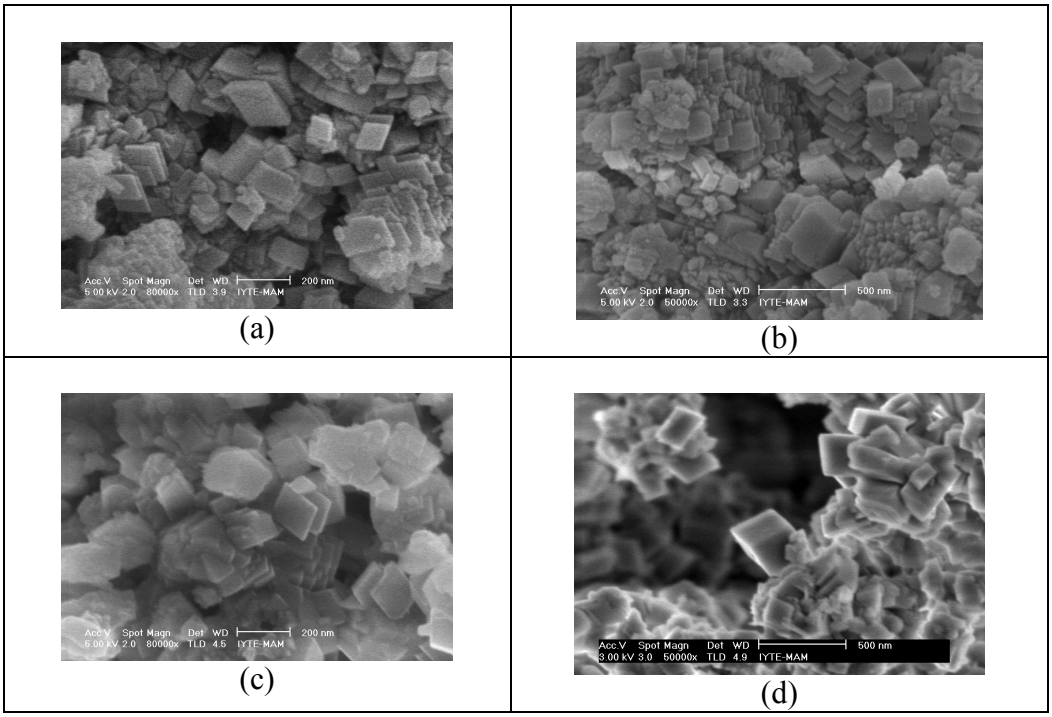

Figure 4.28. SEM images of $MnCO_3$ precipitated on (a, b) calcite surface, (c, d) aragonite surface.

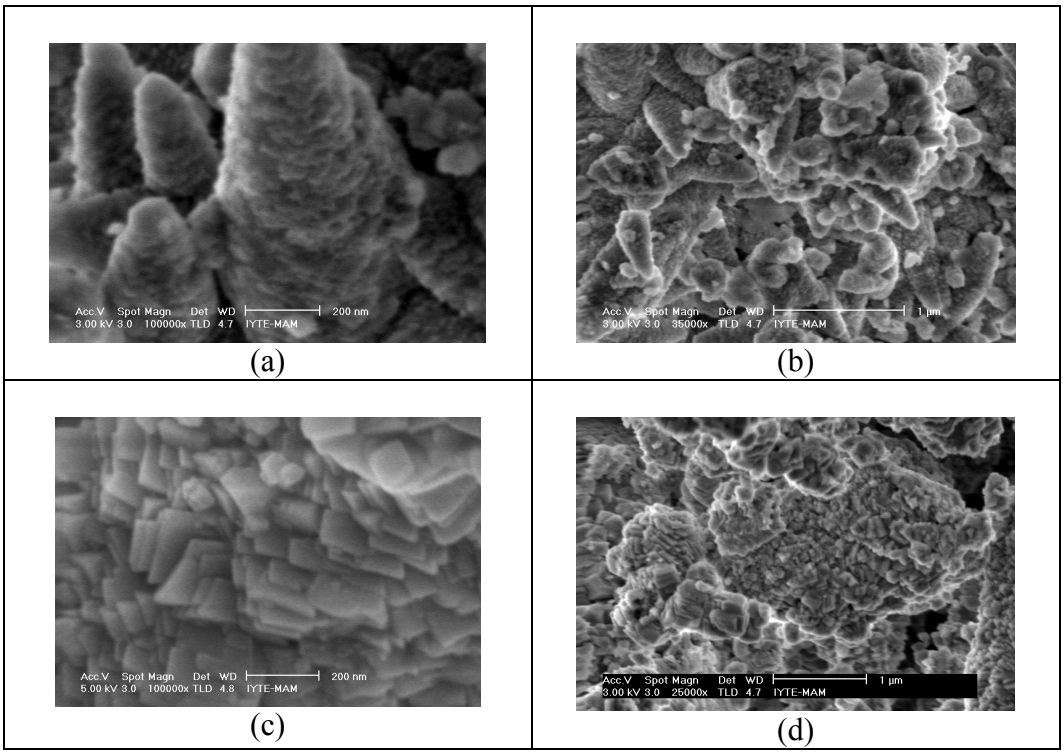

Figure 4.29. SEM images of $CdCO_3$ precipitated on (a, b) calcite surface, (c, d) aragonite surface.

4.4.2. Fourier Transform Infrared (FTIR)

FTIR was used to follow the possible changes in vibrational bands of calcite and aragonite as a result of their interactions with Ba^{2+}, Mn^{2+}, and Cd^{2+} ions, both for sorption and precipitation mechanisms. In principle, the vibrational spectra of carbonate minerals contains modes caused by symmetric stretching (ν1), out-of-plane bending (ν2), asymmetric stretching (ν3), in-plane-bending (ν4), in addition to the two combination modes (ν1+ν3) and (ν1+ν4). It is known that a gaseous carbonate ion possesses a trigonal planar shape with a point group of D_{3h} and the selection rules based on symmetry considerations predict that the ν1 mode is IR inactive. It can be theoretically shown that the D_{3h} symmetry of carbonate ion is lowered to D_3 in the case of calcite and C_s in the case of aragonite the thing that leaves the carbonate vibrational modes unchanged in the case of calcite but activates the ν1 mode and causes the ν3 and ν4 modes to split in the case of aragonite (Nakamoto 1986).

In the FTIR spectrum of calcite used in this study, the vibration bands ν2, ν3, and ν4 appear at 872, 1449, and 714 cm^{-1}. Even though ν1 vibration mode is not active

in pure calcite, a weak feature is observed at 1079 cm^{-1} which is stemming from minor impurities.

The FTIR spectra of calcite and aragonite before and after interaction of Ba^{2+}, Mn^{2+}, and Cd^{2+} ions are given in Figure 4.30, 4.31, and 4.32, respectively. The changes in the vibrational bands are consequences of the change in the molecular environment of carbonate groups. As it is understood from the figures, adsorptions of Mn^{2+} and Cd^{2+} ions by calcite and aragonite minerals, causes minor changes in vibration bands (Figure 4.31 (ii), and 4.32 (ii)). On the other hand, Ba^{2+} ion is seen to cause various discrepancies (Figure 4.30 (ii)). It is known that these discrepancies are proportional to the amount of ions but the results of the studies show that ionic radius is also effective. Due to the scarcity of the information available about this subject, it was not possible to compare the results with similar values in literature. The ionic radiuses of Mn^{2+}, Cd^{2+}, Ba^{2+}, and Ca^{2+} ions are 0.83, 0.95, 1.35, and 1.00 Å, respectively. The difference in size between Ba^{2+} and Ca^{2+} is much larger compared to the difference between Mn^{2+}or Cd^{2+} with Ca^{2+}. Thus, the incorporation of Ba^{2+} in the lattice of calcite and aragonite as a result of sorption can be expected to cause more impact than Mn^{2+} or Cd^{2+}, yielding to a change in intensities and energies of the vibration modes. At the stage of sorption, the most distinctive change in calcite bands is an increase in intensity of ν1 vibration which indicates a distortion in carbonate group symmetry. Another important alteration is a splitting of double bands of ν2 and ν4 vibrations of carbonate groups in both calcite and aragonite minerals. In general, the bands are observed to shift towards lower energy values (red-shifts), indicating weaker interaction of Ba^{2+} ion, with CO_3^{2-} ions in comparison to he interaction of Ca^{2+} ions with CO_3^{2-} ions in the carbonate matrix.

FTIR spectra of metal carbonates after precipitate formation on calcite and aragonite surfaces are shown in Figure 4.30 (iii), 4.31 (iii), and 4.32 (iii), respectively. As expected, the formations of metal carbonates cause more distinct variations than adsorption. These variations are mostly pronounced as a result of $BaCO_3$ formation. When $BaCO_3$ appeared as a distinct phase as a result of precipitation at concentrations beyond 1000 mg/L, a split in the ν1 band took place and the splits in ν2 and ν4 modes were greatly enhanced for both of calcite and aragonite cases. All the splits occurred at lower wavenumbers. The emerging features were assigned to $BaCO_3$ fractions in the carbonate mixtures. To confirm this assignment, FTIR spectra of a separate pure sample of $BaCO_3$ were recorded and compared. According to the results, the bands of ν1, ν2,

ν3, ν4 in pure $BaCO_3$ occurs at 1056, 854, 1432, and 690 cm^{-1}, respectively, which are very close to the newly emerging peaks after precipitation of $BaCO_3$ on calcite and aragonite.

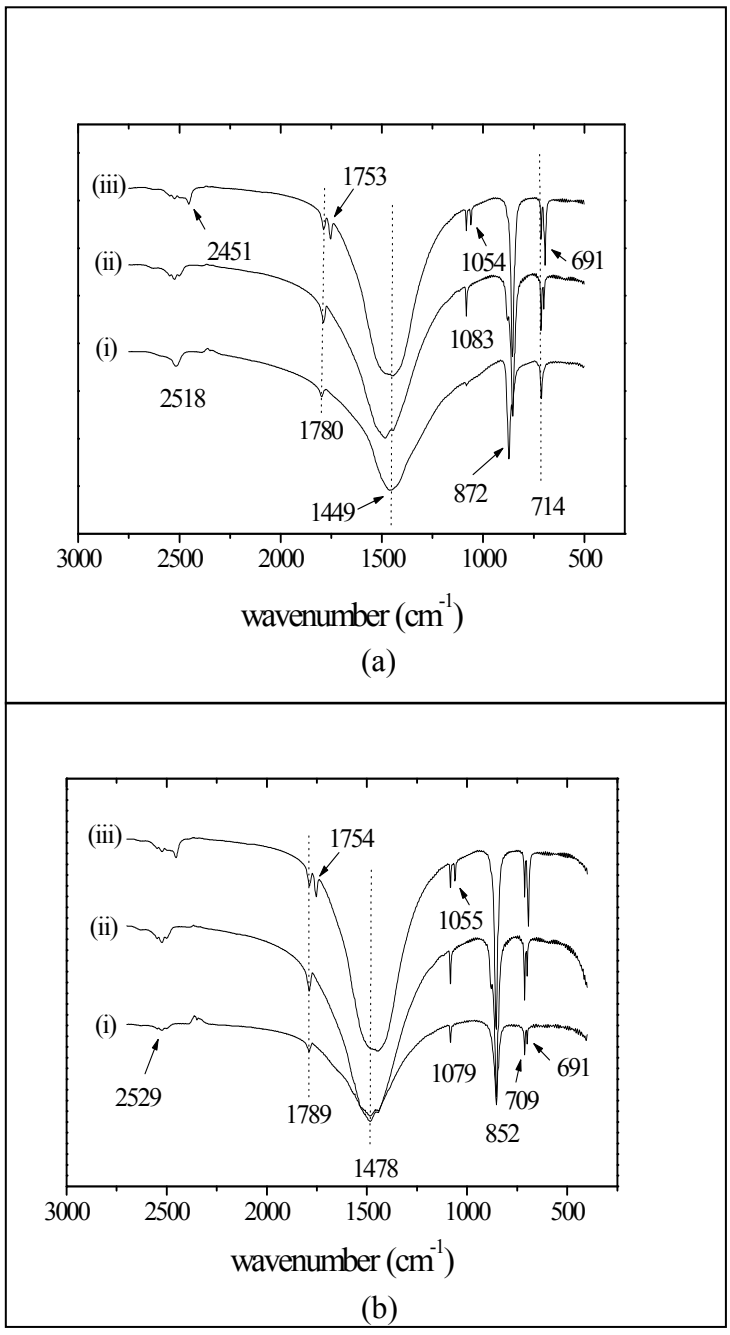

Figure 4.30. FTIR spectra of (a): (i) calcite, (ii) Ba^{2+}-calcite (500 mg/L Ba^{2+}), (iii) $BaCO_3$-calcite (10000 mg/L Ba^{2+}), (b): (i) aragonite, (ii) Ba^{2+}-aragonite (500 mg/L Ba^{2+}), (iii) $BaCO_3$-aragonite (10000 mg/L Ba^{2+}).

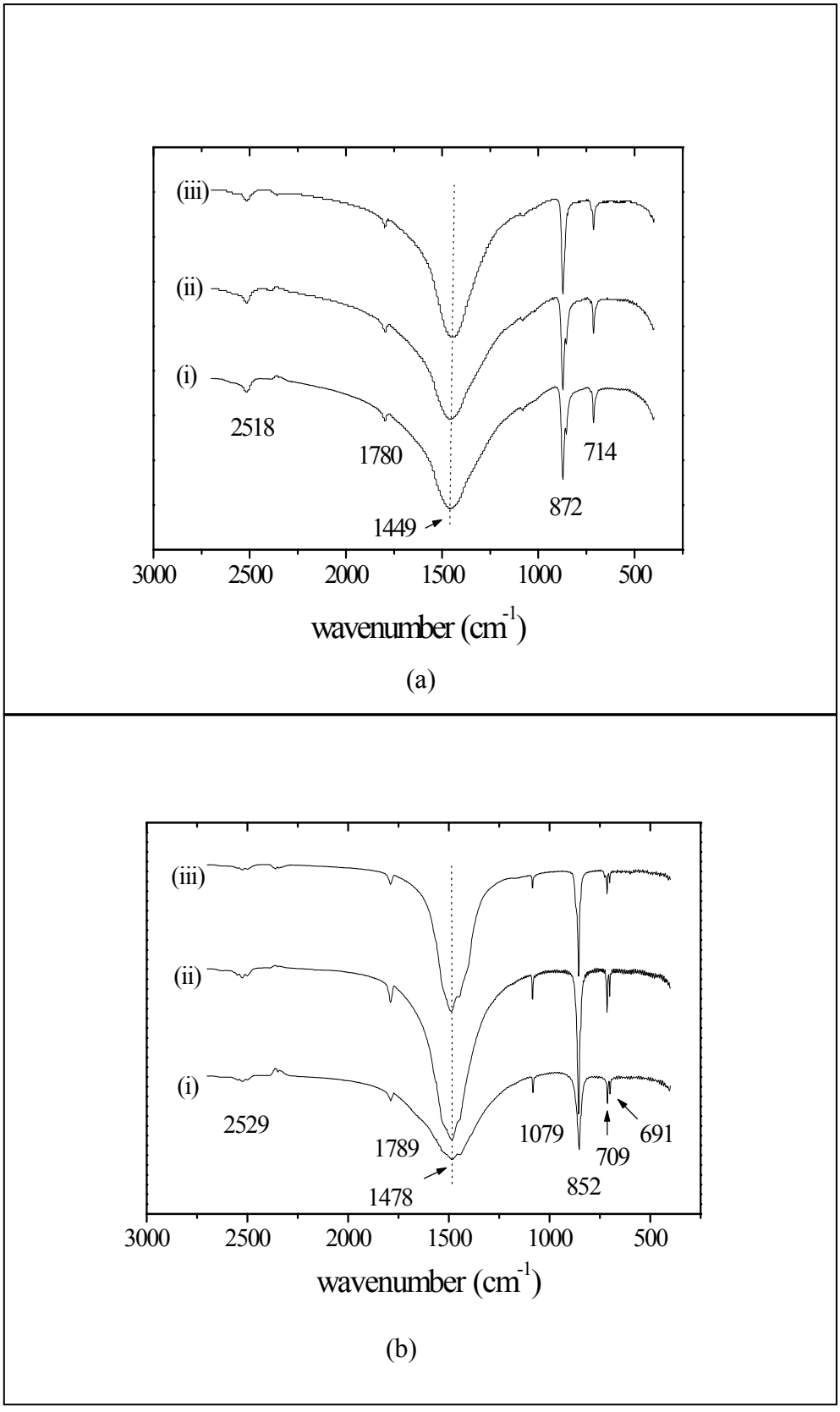

Figure 4.31. FTIR spectra of (a): (i) calcite, (ii) Mn^{2+}-calcite (500 mg/L Mn^{2+}), (iii) $MnCO_3$-calcite (10000 mg/L Mn^{2+}), (b): (i) aragonite, (ii) Mn^{2+}-aragonite (500 mg/L Mn^{2+}), (iii) $MnCO_3$-aragonite (10000 mg/L Mn^{2+}).

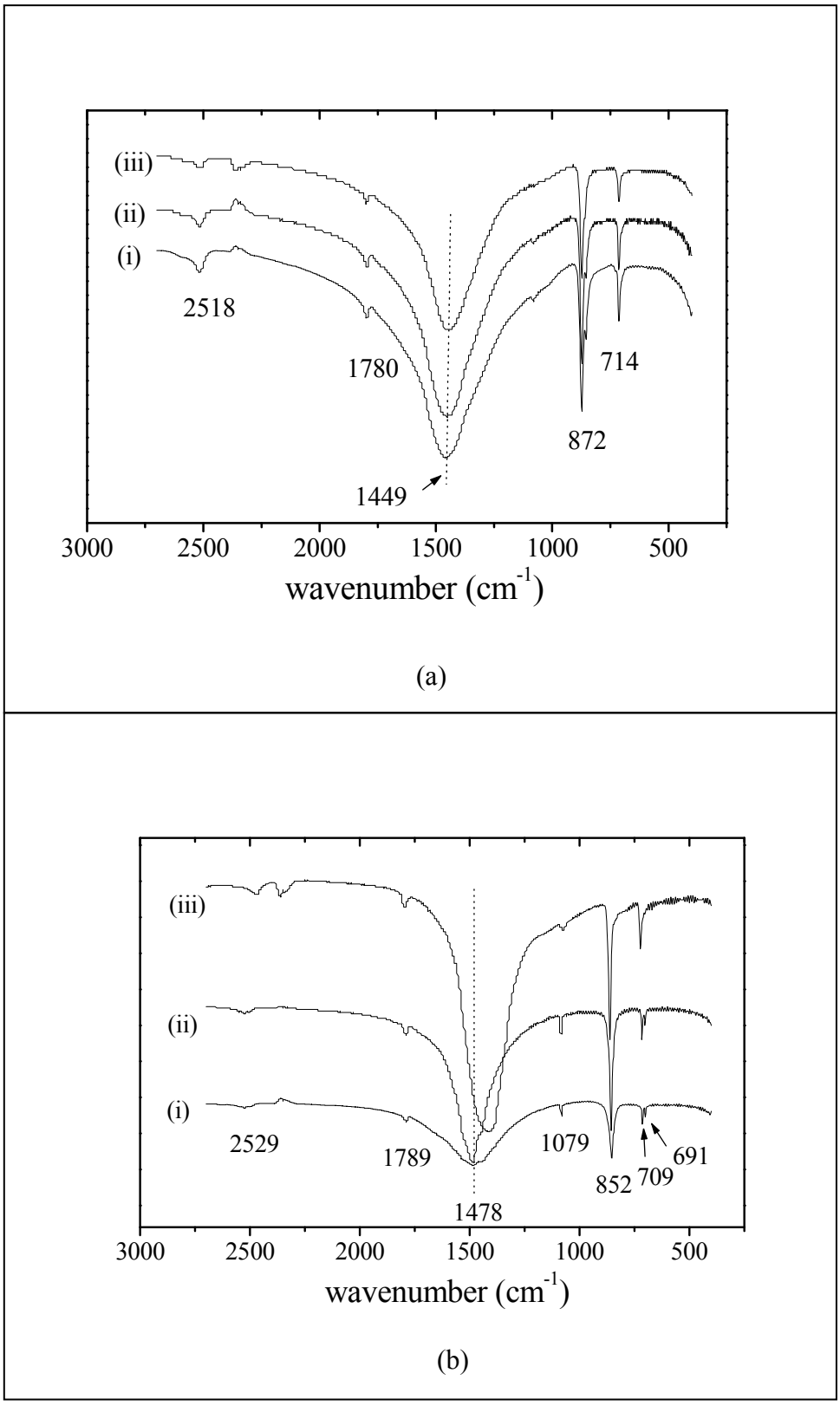

Figure 4.32. FTIR spectra of (a): (i) calcite, (ii) Cd^{2+}-calcite (500 mg/L Cd^{2+}), (iii) $CdCO_3$-calcite (10000 mg/L Cd^{2+}), (b): (i) aragonite, (ii) Cd^{2+}-aragonite (500 mg/L Cd^{2+}), (iii) $CdCO_3$-aragonite (10000 mg/L Cd^{2+}).

CHAPTER 5

CONCLUSION

In this study, the kinetic aspects of the uptake of Ba^{2+}, Mn^{2+}, and Cd^{2+} ions by calcite and aragonite minerals over a wide range of concentrations at the stages of adsorption and precipitate overgrowth was investigated. In addition to that, the morphological and structural characterization of metal ion carbonates formed on calcite and aragonite were also included in this study. Also, the effects of pH and temperature change on precipitate formation were studied.

Analysis of the kinetic results has shown that Cd^{2+} ions approach equilibrium more rapidly than Ba^{2+} and Mn^{2+} ions, the thing valid for both calcite and aragonite minerals. Additionally, the results demonstrate that the kinetics of these three ions on calcite and aragonite minerals is best described by the pseudo-second order rate equation. The affinity demonstrated by both minerals appears to be the highest towards Cd^{2+} ions and smallest towards Ba^{2+} ions. Moreover, the uptake of the three ions appeared to be enhanced as a result of temperature increase.

The studies on precipitate formation of metal carbonates upon interaction with calcite and aragonite showed that the more metal-carbonate formation occurred when the ions were interacted with aragonite as compared to calcite. XRD quantitative analysis was performed in order to determine the amounts of carbonates formed as a result of interaction of ions with calcite and aragonite minerals. According to the three-dimensional graphs of $MeCO_3$ mass fractions calculated using derived equations at different times and initial concentration, $BaCO_3$ is demonstrating the slowest kinetics among three carbonates and as initial ion concentration increases the amount of precipitated $BaCO_3$ is increased markedly. Comparatively, the increase in initial concentration led to less enhancement in precipitate formation of $MnCO_3$ and $CdCO_3$. At 10000 mg/L concentration, $MnCO_3$ and $CdCO_3$ appeared to cover almost completely the aragonite surface, the thing confirmed also by EDS analysis of elemental distribution. Furthermore, the increase of pH to 10.0, caused an increment of precipitate formation, the thing more distinctly seen in aragonite. The formation of $MeCO_3$ on calcite surface is most pronounced in the case of contact with Cd^{2+} ions and is the least

with Ba^{2+} ions. In addition, the results have shown that the increase of medium temperature to 50^{o}C caused an apparent increase in the intensities of precipitated metal carbonates.

According to SEM images, $BaCO_3$ minerals possess olivary-like morphology with an average particle size of 1-2 μm. $MnCO_3$ demonstrated layered rhombohedral morphology with particle size of about 200 nm. Comparatively, $CdCO_3$ morphology appeared to be less distinct than other carbonates, showing aggregates with a conic shape that are1-2 μm in size with each aggregate consisting of layers whose edge length is approximately 100 nm. Based on FTIR results, the ionic radius seems to be the most effective parameter in affecting the vibrational modes of calcite and aragonite. So, the incorporation of Ba^{2+} in the calcite or aragonite lattice appeared to cause more impact than Mn^{2+} or Cd^{2+} yielding.

Further studies can be performed to assess the effect of pH and temperature on precipitate formation kinetics of the metal carbonates.

REFERENCES

Bancroft, G., Brown, J.R., Fyfe, W.S., 1977. "Quantitative X-ray Photoelectron Spectroscopy (ESCA): Studies of Ba^{2+} Sorption on Calcite", *Chemical Geology*.Vol. 19, pp. 131-144.

Bilinski, H., Kozar, S., Plavšić, M., Kwokal $\hat{Z}$., Branica, M., 1991. "Trace Metal Adsorption on Inorganic Solid Phases under Estuarine Conditions", *Marine Chemistry*. Vol. 32, pp. 225-233.

Böttcher, M.E., Tesoriero, A.J., Pankow, J.F., 1997. "Comment Solid Solution Partitioning of Sr^{2+}, Ba^{2+}, and Cd^{2+} to Calcite", *Geochimica Cosmochimica Acta*. Vol. 61, pp. 661-662.

Capellen, P.V., Charlet, L., Stumm, W., Wersin, P., 1993. "A Surface Complexation Model of the Carbonate Mineral-Aqueous Solution Interface", *Geochimica et Chosmochimica Acta*.Vol. 57, pp. 3505-3518.

Chiarello, R.P., Sturchio, N.C., Grace, J.D., Geissbuhler, P., Sorensen, L.B., Cheng, L., Xu, S., 1997. "Otavite-calcite Solid Solution Formation at the Calcite-water Interface Studied in situ by Synchrotron X-ray Scattering", *Geochimica et Cosmochimica Acta*. Vol. 61, pp. 1467-1474.

Curti, E., 1999. "Coprecipitation of Radionuclides with Calcite: Estimation of Partition Coefficients based on a Review of Laboratory Investigations and Geochemical Data", *Applied Geochemistry*. Vol. 14, pp. 433-445.

Davis, J.A., Fuller C.C., Cook A.D., 1987. "A Model for Trace Metal Sorption Processes at the Calcite Surface: Adsorption of Cd^{2+} and Subsequent Solid Solution Formation", *Geochimica et Cosmochimica Acta*. Vol. 51, pp. 1477-1490.

Ewing, G.W., 1985. "Atomic Absorption", in *Instrumental Methods of Chemical Analysis*, (McGraw-Hill Book Co.-Singapore), pp.109-122.

Fuller, C.C., Davis, J.A., 1987. "Processes and Kinetics of Cd^{2+} Sorption by a Calcareous Aquifer Sand", *Geochimica et Cosmochimica Acta*. Vol. 51, pp. 1491-1502.

Garcia-Sánchez A. and Álvarez-Ayuso E., 2002. "Sorption of Zn, Cd and Cr on Calcite. Application to Purification of Industrial Wastewaters", *Minerals Engineering*. Vol.15/7, pp. 539-547.

Godelitsas, A., Astilleros, J.M., Hallam, K., Harissopoulos, S., Putnis, A., 2003. "Interaction of Calcium Carbonates with Lead in Aqueous Solutions", *Environmental Science and Technology*. Vol. 37, No. 15, pp. 3351-3360.

Gutjahr, A., Dabringhaus H., Lacmann R., 1996. "Studies of the Growth and Dissolution Kinetics of the $CaCO_3$ Polymorphs Calcite and Aragonite II. The Influence of Divalent Cation Additives on the Growth and Dissolution Rates", *Journal of Crystal Growth*. Vol. 158, pp. 310-315.

Han, R., Zou, W., Zhang, Z., Shi, J., Yang, J., 2006. "Removal of Copper (II) and Lead (II) from Aqueous Solution by Manganese Oxide Coated Sand: I. Characterization and Kinetic Study", *Journal of Hazardous Materials*. Vol.137, pp. 384-395.

Ho, Y.S., Mckay, G., 1998. "Sorption of Dye from Aqueous Solution by Peat", *Chemical Engineering Journal*. Vol. 70, pp. 115-120.

Jenniss, S.W., Katz, S.A., Lynch, R.W., 1997. "Atomic Absorption Spectrometry", in *Application of Atomic Spectrometry to Regulatory Compliance Monitoring*, (Wiley-VCH, Inc., New York), pp. 2-18.

Jensen, D.L., Boddum, J.K., Tjell, J.C., Christensen, T.H., 2002. "The Solubility of Rhodochrosite ($MnCO_3$) and Siderite ($FeCO_3$) in Anaerobic Aquatic Environments", *Applied Geochemistry*. Vol. 17, pp. 503-511.

Johnson, C.A. and Furrer G., 2002. "Influence of Biodegradation Processes on the Duration of $CaCO_3$ as a pH Buffer in Municipal Solid Waste Incinerator Bottom Ash", *Environmental Science Technology*. Vol. 36/2, pp. 215-220.

Kinsman, D.J., Holland, H.D., 1969. "The Co-precipitation of Cations with $CaCO_3$-IV. The Co-precipitation of Sr^{2+} with Aragonite between 16° and 96°C", *Geochimica et Cosmochimica Acta*. Vol. 33, pp. 1-17.

Kirby, C.S. and Rimstidt, J.D., 1994. "Interaction of Municipal Solid Waste Ash with Water", *Environmental Science Technology*. Vol. 28, pp. 443-451.

Kitano, M.O., 1986. "Coprecipitation of Alkali Metal Ions with Calcium Carbonate", *Geochimica et Cosmochimica Acta*. Vol. 50, pp. 49-58.

Kosmulski, M., 2001. *Chemical Properties of Material Surfaces*, (Marcel Dekker, Inc., New York), pp. 207.

Lagergren, S., 1898. "Zur Theorie der Sogenannten Adsorption Gelöster Stoffe", *K. Sven. Vetenskapsakad. Handl*. Vol. 24, pp. 1-39.

Langmuir, D., 1997. *Aqueous Environmental Chemistry*, (Prentice-Hall, Inc., New Jersey), pp. 193-230.

Lieser, K.H., 1995. "Radionuclides in the Geosphere: Sources, Mobility, Reactions in Natural Waters and Interactions with Solids", *Radiochimica Acta*. Vol. 70/71, pp. 355.

Lorens, R.B., 1981. "Sr, Cd, Mn and Co Distribution Coefficients in Calcite as a Function of Calcite Precipitation Rate", *Geochimica et Cosmochimica Acta*. Vol. 45, pp. 553-561.

Magaritzl, M., Brenner, B., Ronen, D., 1990. "Ba and Sr Distribution at the Water-table: Implications for Monitoring Ground-water at Nuclear Waste Repository Sites", *Applied Geochemistry*. Vol. 5, pp. 555-562.

Martin-Garin, A., Gaudet, J.P., Charlet, L., Vitart, X., 2002. "A Dynamic Study of the Sorption and the Transport Processes of Cadmium in Calcareous Sandy Soils", *Waste Management*. Vol. 22, pp. 201-207.

Meece, D.E. and Benninger, L.K., 1993. "The Coprecipitation of Pu and Other Radionuclides with $CaCO_3$", *Geochimica et Cosmochimica Acta*. Vol. 57, pp. 1447-1458.

Miyake, M., Komarneni, S., Roy, R., 1988. "Immobilization of Pb^{2+}, Cd^{2+}, Sr^{2+} and Ba^{2+} Ions using Calcite and Aragonite", *Cement and Concrete Research*. Vol. 18, pp. 485-490.

Moulin, P., Roques, H., 2003. "Zeta Potential Measurement of Calcium Carbonate", *Journal of Colloid and Interface Science*. Vol. 261, pp.115-126

Nakamoto, K., 1986. *Infrared and Raman Spectra of Inorganic and Coordination Compounds*, (John Wiley & Sons New York), pp. 86-87.

Ning, X., Hochella, Jr. M.F., Brown, Jr. G.E., Parks, G.A., 1996. "Co(II) Sorption at the Calcite-water Interface: I. X-ray Photoelectron Spectroscopic Study", *Geochimica et Cosmochimica Acta*. Vol. 60, pp. 2801-2815.

Ouhadi, V.R. and Yong, R.N., 2003. "Impact of Clay Microstructure and Mass Absorption Coefficient on the Quantitative Mineral Identification by XRD Analysis", *Applied Clay Science*. Vol. 23, pp. 141-148.

Pagenkopf, G.K., 1978. *Introduction to Natural Water Chemistry*, (Marcel Dekker, Inc., New York), pp. 1-16.

Pingitore, N.E., Eastman, M.P., Sandidge, M., Oden, K., Freiha, B., 1988. "The Coprecipitation of Manganese(II) with Calcite: An Experimental Study", *Marine Chemistry*. Vol. 25, pp. 107-120.

Pingitore, N.E. and Eastman, M.P., 1984. "The Experimental Partitioning of Ba^{2+} into Calcite", *Chemical Geology*. Vol. 45, pp. 113-120.

Piriou, B., Fedoroff, M., Jeanjean, J., Bercis, L., 1997. "Characterization of the Sorption of Europium(III) on Calcite by Site-Selective and Time-Resolved Luminescence Spectroscopy", *Journal of Colloid and Interface Science*. Vol. 194, pp. 440-447.

Prieto, M., Cubillas, P., Fernández-Gonzalez, Á., 2003. "Uptake of Dissolved Cd by Biogenic and Abiogenic Aragonite: A Comparison with Sorption onto Calcite", *Geochimica Cosmochimica Acta*. Vol. 67, pp. 3859-3869.

Robbins, J.A., Lindner, G., Pfeiffer, W., Kleiner, J., Stabel, H.H., Frenzel, P., 1992. "Epilimnetic Scavenging of Chernoobyl Radionuclides in Lake Constance", *Geochimica et Cosmochimica Acta*. Vol. 56, pp. 2339-2361.

Shahwan, T., Atesin, A.C., Erten, H.N., Zararsiz, A., 2002. "The Uptake of Ba^{2+} Ions by Natural Bentonite and $CaCO_3$: A Radiotracer, EDXRF and PXRD Study", *Journal of Radioanalytical Nuclear Chemistry*. Vol. 254/3, pp. 563.

Shahwan, T., Zünbül, B., Tunusoğlu, O., Eroğlu, A.E., 2005. "AAS, XRPD, SEM/EDS, and FTIR Characterization of Zn^{2+} Retention by Calcite, Calcite-kaolinite, and Calcite-clinoptilolite Minerals", *Journal of Colloid and Interface Science*. Vol. 286, pp. 471-478.

Shahwan, T., Zünbül, B., Eroğlu, A.E., Yılmaz S., 2005. "Effect of Magnesium Carbonate on the Uptake of Aqueous Zinc and Lead Ions by Natural Kaolinite and Clinoptilolite", *Applied Clay Science*. Vol. 30, pp. 209-218.

Shahwan, T., Zünbül, B., Akar, D., 2005. "Study of the Scavenging Behavior and Structural Changes Accompanying the Interaction of Aqueous Pb^{2+} and Sr^{2+} Ions with Calcite". *Geochimica Journal*. Vol. 39, pp. 317-326.

Skoog, M.D., West, D.M., Holler, F.J., 1997. *Fundamentals of Analytical Chemistry*, (Harcourt Brace & Company, Florida), pp. A-6.

Smith, B.C., 1996. *Fundamentals of Fourier Transform Infrared Spectroscopy*, (CRC Press LLC, Florida), pp.1-53.

Speck, P.J.H.R., de Graaf, J.W.M, Nieuwenhuis, J.D., Zijlstra, J.J.P., 1998. "Optimizing the Process of Sulphuric Acid Injection into Limestones", *Journal of Geochemical Exploration*. Vol. 62, pp. 331-335.

Sternbeck, J., 1997. "Kinetics of Rhodochrosite Crystal Growth at 25^{o}C: The Role of Surface Speciation", *Geochimica et Cosmochimica Acta*. Vol. 61, pp. 785-793.

Stipps, S.L.S., 1999. "Toward a Conceptual Model of the Calcite Surface: Hydration, Hydrolysis, and Surface Potential", *Geochimica et Cosmochimica Acta*. Vol. 63, pp. 3121-3131.

Strobel, A.S. and Heineman, R.W., 1989. *Chemical Instrumentation: A Systematic Approach,* (John Wiley & Sons, Inc., New York), pp. 785-787.

Stumm, W. and Morgan, J.J., 1996. *Aquatic Chemistry*, (John Wiley & Sons, Inc., New York), pp. 349- 608.

Stumm, W., 1992. *Chemistry of the Solid-Water Interface*, (John Wiley & Sons, Inc., New York), pp. 87-307.

Sverjinsky, D.A. and Molling, P.A., 1992. "A Linear Free Energy Relationship for Crystalline Solids and Aqueous Ions", *Nature*. Vol. 356, pp. 231-234.

Terakado, Y. and Masuda, A., 1989. "The Coprecipitation of Rare-earth Elements with Calcite and Aragonite", *Chemical Geology*. Vol. 69, pp. 103-110.

Tesoriero, A.J. and Pankow J.F., 1996. "Solid Solution Partitioning of Sr^{2+}, Ba^{2+}, and Cd^{2+} to Calcite", *Geochimica et Cosmochimica Acta*. Vol. 60, pp. 1053-1063.

Torstenfelt, B., Andersson, K., Allard, B., 1982. "Sorption of Strontium and Cesium on Rocks and Minerals", *Chemical Geology*. Vol. 36, pp. 123-137.

Wang, Y. and Xu, H., 2001. "Prediction of Trace Metal Partitioning Between Minerals and Aqueous Solutions: A Linear Free Energy Correlation Approach", *Geochimica et Cosmochimica Acta*. Vol. 65, pp. 1529-1543.

WEB_1, 2007. The Metropolitan Emergency Response and Logistical Information Network, 16/03/2006.
http://www.ndcrt.org/links/hazmat.html

WEB_2, 2007. The Mineral Calcite, 23/04/2007.
www.galleries.com/minerals/carbonat/calcite/calcite.htm

WEB_3, 2005. Calcite Structure, 14/12/2005.
www.uvgb.edu/DutchS/PETROLGY/Calcite%20Structure.htm

WEB_4, 2006. Crystal Structure Gallery, 09/03/2006
www.staff.aist.go.jp/nomura-k/english/itscgallary-e.htm

WEB_5, 2007. The Mineral Aragonite, 23/04/2007.
www.galleries.com/minerals/carbonat/calcite/aragonite.htm

WEB_6, 2007. Solid State Diffusion, 20/04/2007.
http://www.uio.no/studier/emner/matnat/kjemi/KJM5120/v05/undervisningsmateriale/KJM5120-Ch5-Diffusion.pdf

WEB_7, 2007. Atomic Absorption Spectroscopy, 22/02/2007.
www.cartage.org.lb/en/themes/sciences/chemistry/Analyticalchemistry/MethodsInstrumentation/Spectroscopy/Atomicabsorption/Atomicabsorption.htm

WEB_8, 2007. Basic Overview of ICP-AES, 14/02/2007.
http://www.odp.tamu.edu/publications/tnotes/tn29/technot2.htm

WEB_9, 2007. Material Analytical Services, 15/02/2007.
http://www.mastest.com.htm

WEB_10, 2007. Centre of Diffraction Studies, 11/02/2007. www.abdn.ac.uk/~che241/cdiff/index.htm

WEB_11, 2006. New Hampshire Materials Laboratory, Inc., 15/05/2006. http://nhml.com/resources_NHML_Scanning-Electron-Microscopes.php

WEB_12, 2007. Keck Interdisciplinary Surface Science Center, 12/04/2007 www.nuance.northwestern.edu/keckii/ftir1.asp

Weijden, R.D., Weijden, C.H., Comans, R.N.J., 1994. "Sorption and Sorption Reversibility of Cd on Calcite under Simulated Riverine, Estuarine and Marine Conditions", *Marine Chemistry*. Vol. 47, pp. 65-79.

Wersin, P., Charlet, L., Karthein, R., Stumm, W., 1989. "From Adsorption to Precipitation: Sorption of Mn^{2+} on $FeCO_3(s)$", *Geochimica Cosmochimica Acta*. Vol. 53, pp. 2787-2796.

Zachara, J.M., Kittrick, J.A., Harsh, J.B., 1988. "The Mechanism of Zn^{2+} Adsorption on Calcite", *Geochimica et Cosmochimica Acta*. Vol.52, pp. 2281-2291.

Zachara, J.M., Kittrick, J.A., Dake, L.S., Harsh, J.B., 1989. "Solubility and Surface Spectroscopy of Zinc Precipitates on Calcite", *Geochimica et Cosmochimica Acta*. Vol. 53, pp. 9-19.

Zachara, J.M., Cowan, C.E., Resch, C. T., 1991. "Sorption of Divalent Metals on Calcite", *Geochimica et Cosmochimica Acta*. Vol. 55, pp. 1549-1562.

Zhu, C., 2002. "Estimation of Surface Precipitation Constants for Sorption of Divalent Metals onto Hydrous Ferric Oxide and Calcite", *Chemical Geology*. Vol. 188, pp. 23-32.